Universidade de Aveiro Departamento de engenharia cerâmica e do vidro
Ano 2011

Jorge Louro Luís

Compósitos PU/ZnO para aplicações biomédicas
PU/ZnO composites for biomedical applications

Universidade de Aveiro Departamento de engenharia cerâmica e do vidro
Ano 2011

Jorge Louro Luís

Compósitos PU/ZnO para aplicações biomédicas
PU/ZnO composites for biomedical applications

Dissertação apresentada à Universidade de Aveiro para cumprimento dos requisitos necessários à obtenção do grau de Mestre em engenharia de materiais, realizada sob a orientação científica da Doutora Maria Elizabete Jorge Vieira Da Costa, Professora auxiliar e co-orientação da Doutora Maria Helena Figueira Vaz Fernandes, Professora associada do Departamento de engenharia cerâmica e do vidro da Universidade de Aveiro.

Dissertation presented to the University of Aveiro in fulfilment of the requirements for the awarding of Master degree in Materials engineering carried out under the supervision of Doctor Maria Elizabete Jorge Vieira Da Costa, Assistant Professor and co-orientation of Doctor Maria Helena Figueira Vaz Fernandes, Associated Professor of ceramics and glass engineering department of University of Aveiro.

Este trabalho é dedicado a todas as pessoas que me ajudaram e suportaram até ao fim, especialmente o meu pai, a minha mãe e a minha irmã.

I dedicate this work to the people that believed and supported me till the end, but mostly my father, my mother and my sister.

o júri

presidente

Prof. Doutor Joaquim Manuel Vieira
Professor Catedrático da Universidade de Aveiro

Prof. Doutor Rui Ramos Ferreira e Silva
Professor Associado da Universidade de Aveiro

Prof. Doutor Fernando Jorge Mendes Monteiro
Professor Catedrático da Faculdade de Engenharia da Universidade do Porto

Prof. Doutora Maria Elizabete Jorge Vieira da Costa
Professora Auxiliar da Universidade de Aveiro

Prof. Doutora Maria Helena Figueira Vaz Fernandes
Professora Associada da Universidade de Aveiro

agradecimentos

Gostaria de agradecer às minhas orientadoras, Prof. Doutora Maria Elizabete Jorge Vieira da Costa and Prof. Doutora Maria Helena Figueira Vaz Fernandes pelo esforço e tempo dedicado a este trabalho, ao Prof. Martinho Oliveira e ESAN (Escola Superior Aveiro Norte) pelas valiosas discussões e equipamento utilizado, às técnicas de caracterização de pó Eng. Célia Miranda, Ana Ribeiro e Maria Bastos pela disponibilidade e ajuda prestada, à Marta, Fiorentina e Bruno pelas sessões de SEM, às profs. Sandra Vieira and Odete Silva pela ajuda na viabilidade celular e um especial obrigado aos meus colegas de laboratório pela ajuda e apoio que me deram.

acknowledgments

I would like to thank my coordinators Prof. Doutora Maria Elizabete Jorge Vieira da Costa and Prof. Doutora Maria Helena Figueira Vaz Fernandes for all the effort and time they dedicated to this work, Prof. Martinho Oliveira and ESAN (Escola Superior Aveiro Norte) for the borrowed equipment and valuable discussions, the powder characterization technicians Eng. Célia Miranda, Ana Ribeiro e Maria Bastos for the availability help they provided, Marta, Fiorentina and Bruno for the valuable SEM sessions, profs. Sandra Vieira and Odete Silva for the cell viability assays and my laboratory colleagues for all the help and support they provided.

palavras-chave

Compósito, óxido de zinco, poliuretano, nanoparticulas, aplicações biomédicas, células MC3T3

resumo

O presente trabalho visa o estudo da preparação e caracterização de dispositivos biomédicos com capacidade de suscitar diferentes respostas biológicas. Os compósitos de poliuretano e óxido de zinco (PU/ZnO) mostram-se promissores, pois qualquer dos materiais, em separado, tem revelado propriedades biomédicas interessantes. No entanto, as propriedades da mistura de ambos ainda não estão totalmente esclarecidas. Às próprias nanopartículas ou nanoestruturas de ZnO são apontados desempenhos ambíguos, que tornam imprevisíveis as respectivas respostas biológicas.

Este trabalho tem, assim, como principal objectivo, estudar o efeito da concentração, forma e tamanho de partícula de ZnO nas propriedades de compósitos PU/ZnO, designadamente na sua bioactividade in vitro e resposta celular. Com esse objectivo sintetizaram-se partículas de ZnO nanoestruturadas, por precipitação química, que foram caracterizadas comparativamente com nanopartículas de ZnO comerciais. Avaliaram-se as fases presentes, cristalinidade, forma e tamanho de partícula, área superficial específica e porosidade. Posteriormente formularam-se compósitos de matriz polimérica (poliuretano), carregados com as partículas de ZnO (2% e 50% em peso) e submeteram-se os compósitos a ensaios de bioactividade in vitro e de viabilidade celular (linha MC3T3). Os ensaios de bioactividade revelaram que os compósitos com 50% ZnO, nomeadamente os compósitos com nanoesferas de ZnO, são potencialmente mais bioactivos que o poliuretano ou os compósitos com 2% ZnO. Por seu lado, os estudos de viabilidade celular revelaram que os compósitos com 2% ZnO e o polímero são os que apresentam maior viabilidade celular. Verificou-se que no caso das partículas comerciais ou nanoestruturadas o efeito de 50% de carga é similar ao efeito das próprias partículas, induzindo citotoxicidades muito semelhantes. Os compósitos que continham nanoesferas de ZnO (50% em peso) evidenciaram citotoxicidade superior aos outros. Estes comportamentos são discutidos com base na quantidade de catiões Zn^{2+} libertados para o meio.

Em conclusão, os resultados obtidos mostram que é possível controlar a bioactividade e citotoxicidade dos compósitos PU/ZnO através da manipulação da concentração ou morfologia de partícula de ZnO e, por esta via, desenhar compósitos com potencialidades para aplicações ortopédicas (compósitos com 2% em peso) e compósitos para aplicações em que se pretende travar a proliferação celular, como no tratamento do cancro (compósitos com 50% em peso).

keywords

Composite, zinc oxide, polyurethane, nanoparticles, biomedical aplications, MC3T3 cells

abstract

The present work is focused on the preparation and characterization of biomedical devices able to elicit different biological responses. Polyurethane/zinc oxide composites (PU/ZnO) appear as very promising materials as they may combine the interesting biomedical properties of ZnO and PU. However the properties of the composites, particularly in what the biological response is concerned, are far from being completely known. They are even unpredictable when ZnO nanoparticles or nanostructures are involved as ambiguous behaviours have been pointed out to nanometric sized ZnO particles.

The main objective of the present work is to study the effects of the shape, size and concentration of ZnO particle on the properties of PU/ZnO composites, particularly on its bioactivity and cellular response.

For this purpose ZnO nanoparticles/nanostructures were synthesized by a chemical precipitation method and subsequently characterized in terms of crystal phase composition, crystallinity, shape and particle size, specific surface area and porosity. These properties were further compared to those of commercial ZnO nanoparticles counterparts. PU/ZnO composites were then formulated by loading a PU matrix with ZnO particles (2 and 50$\%_{wt}$) and then submitted to *in vitro* bioactivity tests in SBF and to cell viability assays using a MC3T3 cell line. The bioactivity assays revealed that 50$\%_{wt}$ ZnO loaded composites, namely those loaded with ZnO nanospheres, are potentially more bioactive than both PU and 2$\%_{wt}$ PU/ZnO composites. Regarding cell viability, 2$\%_{wt}$ PU/ZnO formulations were found to be the composites ensuring the higher cell viability. It was also shown that the toxicity effects of the 50$\%_{wt}$ PU/ZnO composites prepared either with commercial or precipitated nanostructured ZnO particles were very similar to the toxicity effects of the corresponding isolated ZnO particles. As for the composites prepared with ZnO nanospheres (50$\%_{wt}$ Pu/ZnO), their toxicity was higher than the remaining composites. These behaviours were discussed based on Zn^{2+} release to SBF media.

As a conclusion, the obtained results show that it is possible to control PU/ZnO composites bioactivity and cytotoxicity by manipulating the concentration and/or ZnO particle morphology, thereby enabling the design of composites with potential usefulness for orthopaedic applications (2 $\%_{wt}$ PU/ZnO) or for biomedical purposes intended to retard cellular proliferation like cancer treatment (50 $\%_{wt}$ PU/ZnO).

List of abbreviations

1,2-D*	-	1,2-Dichloroethane
3T3	-	Fibroblast cell line
A549	-	Glandular cancerous cell line
ATR-FTIR	-	Attenuated total reflectance Fourier transform infrared spectroscopy
B	-	Brushite
BD	-	1,4-buthanediol
BDO	-	1,4-buthanediol
BET	-	Braunauer, Emmet and Teller
BJH	-	Barret, Joyner, Halenda
C**	-	Chloroform
C2	-	2% composite with commercial ZnO nanosized powder
C50	-	50% composite with commercial ZnO nanosized powder
CDDS	-	Controlled drug delivery systems
Cit	-	Citric acid
CNS	-	Central nervous system
CP	-	Calcium phosphate
cZnO	-	Commercial ZnO nanosized powder
DSC	-	Differential scan calorimetry
ED	-	Ethylenediamine
EDS	-	Energy dispersive spectroscopy
ESD	-	Equivalent sphere diameter
FDA	-	Food and drug agency
HA	-	Hydroxyapatite
HBP	-	Human blood plasma
HeLa	-	Immortalized cervical cancer cell line
HL60	-	Leukaemia cell line
HMDI	-	Hydrogenated diphenylmethane-diisocyanate
ICP	-	Inductively coupled plasma spectroscopy
IUPAC	-	International Union of Pure and Applied Chemistry
M	-	Monetite
MC3T3-E1	-	Osteoblast cell line
MDI	-	Diphenylmethane-diisocyanate
mZnO	-	Precipitated ZnO nanostructured powder
NPs	-	Nanoparticles
NT	-	Nanotechnology

P2 - 2% composite with precipitated ZnO nanostructured powder
P50 - 50% composite with precipitated ZnO nanostructured powder
PA - Polyethylene adipate
PBMC - Mononuclear blood cell line
PDT - Photo dynamic therapy
PHECD - Poly(1,6-hexyl 1,2 ethyl carbonate)diol
PNS - Peripheral nerve tissues
PTMEG - Polytetramethylene ether glycol
PTMG - Polytetramethylene ether glycol
PTMO - Polytetramethylene ether glycol
PU - Polyurethane
pZnO - Precipitated ZnO nanostructured powder
R - Gas constant
R2 - 2% composite with precipitated ZnO nanosized powder
R50 - 50% composite with precipitated ZnO nanosized powder
RKO - Colon cancer cell line
ROS - Reactive oxygen species
rZnO - Precipitated nanosized ZnO powder
SBF - Simulated body fluid
SEM - Scan electron microscopy
T cells - Type of white blood cell line
TDI - Toluene diisocyanate
U87 - Glial cancer cell line
UV - Ultra violet light
XRD - X-ray diffraction
ZP - Zinc phosphate

List of symbols

$\cdot OH$ - Hydroxyl radical
$\cdot OH_2$ - Hydroperoxyl radical
$\cdot O^{2-}$ - Superoxide radical anion
a_m - Adsorbate molecule area
C - Carbon
D - Crystallite size
d_{AV} - Average pore size
d_{hkl} - Distance between two crystallographic parallel planes
D_p - Pore diameter
e' - Conduction band promoted electron
$e'/h^{\cdot}$ - Electronic pair electron hole
H - Hydrogen
$h^{\cdot}$ - Valence band electron hole
H^+ - Hydrogen ion
H_2O - Water molecule
H_2O_2 - Hydrogen peroxide
HCO_3^- - Hydrogen carbonate
HO^{2-} - Hydrogen peroxide anion
K - Form factor
m - mass
N - Nitrogen
n - Amount of adsorbed gas
Na - Sodium
N_A - Avogadro constant
n_m - Monolayer capacity
$n\lambda$ - Constructive phase
O - Oxygen
θ - Diffraction angle
O^{2-} - Oxygen ion
$p/p°$ - Partial pressure
r_K - Kelvin radius
r_p - Amount of desorbed gas
S - Pore cumulative SSA
SO_4^{2+} - Sulphate ion
SSA - Specific surface area per mass unit
T - Temperature
t - Monolayer thickness

T_g - Glass transition temperature
V_p - Pore volume
VSSA - Specific surface area per volume unit
Y - Constant
Zn - Zinc
Zn^{2+} - Zinc ion
$ZnCl_2$ - Zinc chloride
ZnO - zinc oxide
β - Width at half height
ϑ^1 - Condensed gas molar volume
λ - Wavelength
ρ - Volumic mass
σ^{1g} - Condensed gas surface energy

List of figures

List of tables

Table of contents

Chapter I

1. Introduction

Zinc oxide (ZnO) is a wide band gap piezoelectric semiconductor with large exciton binding energy used in numerous electronic applications. Moreover, under specific light wavelengths ZnO may undergo free-radical reactions and exhibit cytotoxicity and antibacterial/fungi properties which suggest its medical usefulness. Furthermore, being a broad spectrum UV reflector, ZnO is also a primary choice as sunscreen additive for cosmetic products. ZnO is also a Food and Drug Agency (FDA) approved compound. However, as observed for nanosized materials in general, the biological effects of nanosized or nanostructured ZnO particles are still poorly understood. There is a large controversy on the effects these particles on both human health and environment, as many contradicting aspects being reported. Nanosized particles are generally addressed to be potentially harmful to human health if not properly controlled and thus the interest of confinement in a polymer matrix is very appealing. This strategy may be useful when aiming at a local targeted action [1-35].

Polyurethanes (PUs) are materials of extreme relevance due to their chemical properties, mechanic and possible biodegradability. These characteristics allied to the facile processing methods allows their regular use in the medical area as ventricular devices, diaphragms, heart valves, bioactive vascular grafts, catheters and other devices. PUs, namely tecoflex SG80A PU, is also an FDA approved material and even with its own intrinsic limitations presents itself as potential confining matrix as a way to control the exposure level of these particles [36-47].

PU/ZnO composites are reported for nerve guide channels, catheters or osteoconductive strategies. The addition of ZnO nanoparticles/nanostructures to PU will inevitably change the polymer properties, but as such changes have been inconsistently reported, the biological response to the composite itself also becomes unpredictable [5, 10].

The purpose of the present work is to study the potential of polyurethane/zinc oxide (PU/ZnO) nanocomposites for biomedical applications. The manipulation of some specific properties of ZnO particles such as shape, size and porosity, are carried out and their impact on polyurethane/ZnO composites properties are evaluated, while accessing the resulting composites *in vitro* behaviour.

1.1. Nanocomposites

Composite materials combining a polymer matrix and nanometric sized particles (nanoparticles) are envisaged as promising materials for the near future, referred here as nanocomposites, as they offer the superior properties of nanoparticles while benefiting from the polymer processing technology [1].

It can be roughly stated that polymer/nanoparticles nanocomposites can be prepared through four routes, [1]:

- Solution method: consists on the dissolution of the polymer followed by the dispersion of the nanoparticles in the polymer solution and then by the evaporation of the solvent.
- Melt mixing: the polymer is melted and mixed with the filler and then homogenised.
- In-situ polymerization: the nanoparticles are dispersed in the pre-polymer solution and polymerization is subsequently promoted.
- Template synthesis: using polymer templates the nanoparticles are precipitated within the polymer pores from a precursor solution (particle size is strongly dependent on the polymer pore size distribution).

Nanometric sized particles (nanoparticles) are known since several decades but their effects and properties as polymer nanofillers are not yet clearly known. Furthermore as nanoparticles themselves still pose some challenging issues, they will be specifically addressed in the next section.

A. Nanoparticles

In the XXI century nanoparticles production revealed itself as a key technology that would allow a technological and industrial development as the automobile, computers and communication technologies did in the last century [2].

Prompted by the exceptional properties exhibited by nanoparticles, the research efforts of the scientific community to develop nanoparticles (NPs) and nanotechnologies (NT) have increased in the latest years. The global market also sticks to this tendency as the investment has kept increasing throughout the years with an increase in the nanomaterials business value (figure 1 and table 1) [2, 3].

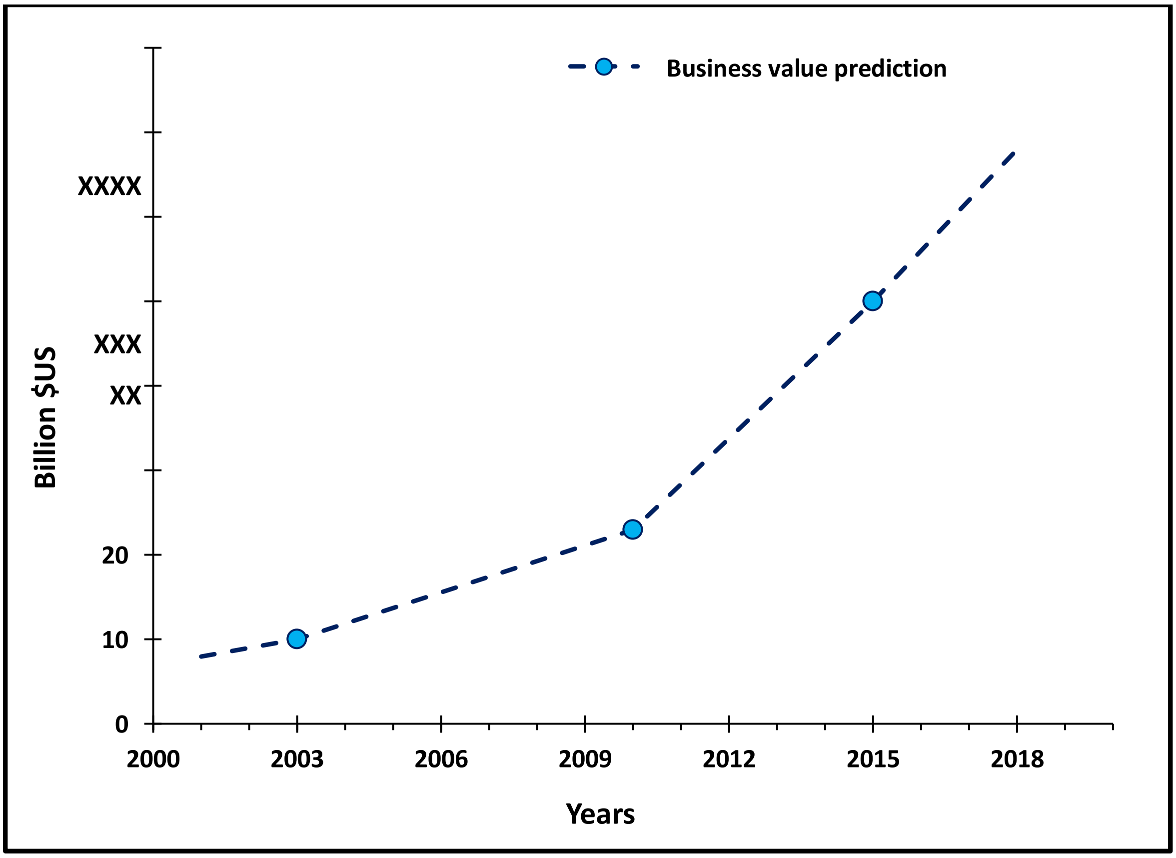

Figure 1. Nanomaterials world market business value prediction, X denotes the digit, i.e. XX double digit, etc. [2].

Table 1. Worldwide nanomaterials interest by region, adapted from [2].

Year	Region	Market	Value
2003	World	Nanoproducts – business value	xx billions US$
2003	World	R&D - public investment	3 billion US$
2005	World	Nanotecnology - investment	5 to 7 billion US$
2006	U.S.A.	Nanotecnology - spent	1,2 billion US$
2008	U.S.A.	Nanomaterials - market	1,4 billion US$
2008	World	Nanoproducts - global market	700 billion US$
2008	World	Nanoproducts - global market	700 billions €
2010	World	Nanoproducts - business value	xxx billions US$
2010	World	Nanoproducts - global market	148 billion US$
2011	World	Nanomaterials - global demand	4,1 billion US$
2015	World	Nanoproducts - business value	xxxx billions US$

x - digit

Part of the interest raised by the nanoparticles relies on the fact that as the particle size diminishes its specific surface area ‘SSA’ increases, providing larger contact areas, enhanced reactivity and a higher number of surface atoms or defects per unit area. The physical and chemical properties of the materials can change drastically as the particle size goes down to the nanometric scale and thus become significantly different from those of the bulk material. Various examples include insulator materials that become conductive, insoluble becoming more soluble and cytotoxicity changes as well. Some newly discovered particles worthy of mention have generated a particular interest in the chemical and semiconductors industries, namely some metallic oxides as aluminium, cerium, iron, zinc, titanium, silicon oxides, nanoclays, some metals like silver and gold, some polymers including dendrimers, fluorenes and polystyrene, and others as carbon black and nanotubes [2].

The health area is raising a great interest for nanoparticles as observed in the drug delivery field as their high surface area and adsorptive properties allow the fixation and transport of relevant biological compounds or drugs to specific sites, improving the performance of controlled drug delivery systems [3, 4].

Tissue engineering is also an area with great expectations regarding nanoparticles because their nanometric size allows the mimetization of nanosized proteins and their high SSA and topographical nanoroughness allows the adsorption of specific proteins, a critical stage in cell adhesion and proliferation as cells do not adhere directly to the material but to the initially adsorbed proteins [5]. Other applications in biology or medicine include Fluorescent biological labels, detection of pathogens or proteins, probing of DNA structure, tumour control, separation and purification of biological molecules or cells, contrast fluid and phagokinetic studies [6]

Depending on their origin nanoparticles can either natural (volcanic/lunar dust, mineral) or anthropogenic. The anthropogenic nanoparticles can be unintentionally released, like in fossil fuels combustions, or can be engineered and designed to suit a certain purpose (engineered nanoparticles) [1].

Nanometric sized particles are normally classified in the following categories (figure 2): nanoparticles, nanosheets, and nanorods [1]:

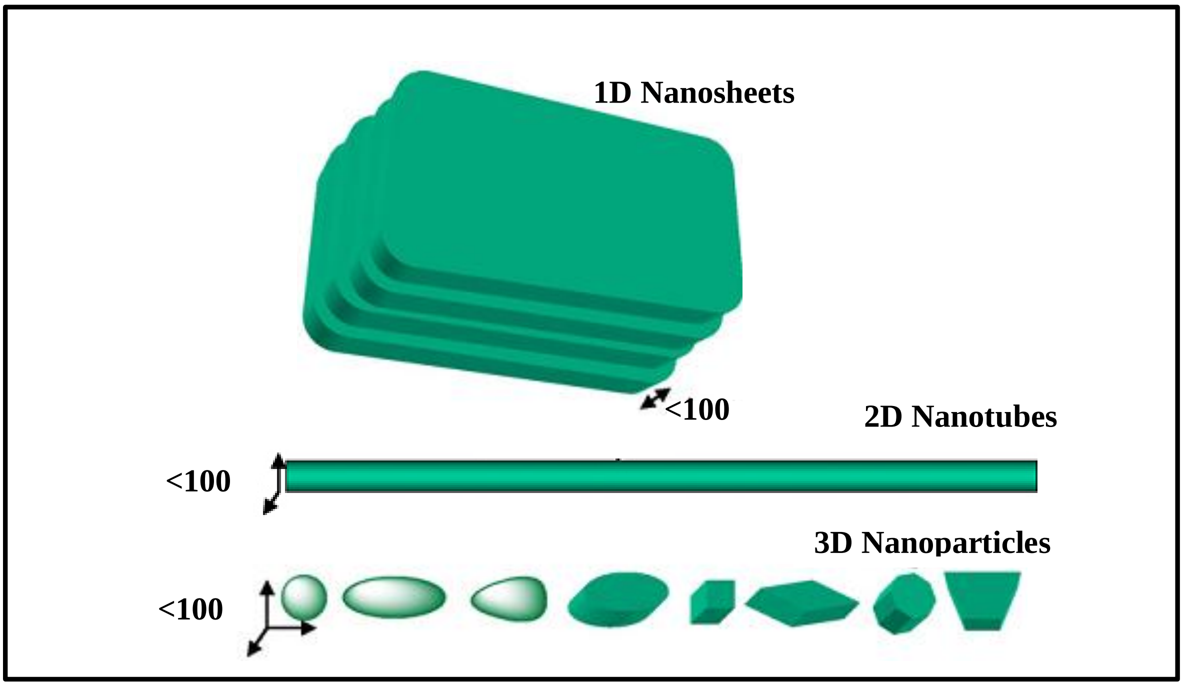

Figure 2. Shape of nanomaterials: nanoparticles, nanotubes and nanosheets, adapted from [1].

Nanoparticles are those particles in which all the three dimensions are under 100 nm, nanotubes are those that have a high length/diameter ratio (fibers, tubes, rods) and two dimensions under 100 nm and nanosheets have only one dimension under 100 nm [1]. By extending the concept of aspect ratio, nanosized materials can also be conveniently addressed and classified according with their dimensionality: one-dimensional - 1D (sheets, thin films), two-dimensional - 2D (tubes, rods and wires – may be attached on a substrate) or three-dimensional 3D (particles) if one, two or three dimensions are in the nanometre size, respectively. 2D particles have the largest aspect ratio as opposed to 3D like particles [7].

There is some controversy regarding this classification (table 2), since the imposed 100 nm as the upper limit is somewhat arbitrary. This limit is commonly considered to be the one at which the properties of the particles differ from the properties of the corresponding bulk materials, but there is no scientific solid evidence to support this statement and the change of properties may occur above this limit [3, 8].

Table 2. Nanomaterial classification and definitions, adapted from [8].

Organization	Definition
European Medicines Agency (EMEA) (2006)	"From the atomic level at around 0.2 nm (2 Å) up to around 100 nm."
The (US-)National Nanotechnology Initiative Strategic Plan December (2007).	"Nanotechnology is the understanding and control of matter at dimensions between approximately 1 and 100 nm, where unique phenomena enable novel applications. ... Dimensions between approximately 1 and 100 nm are known as the nano-scale. Unusual physical, chemical, and biological properties can emerge in materials at the nano-scale. These properties may differ in important ways from the properties of bulk materials and single atoms or molecules."
EU Novel food Regulation (2009).	"'Engineered nanomaterial' means any intentionally produced material that has one or more dimensions of the order of 100 nm or less or is composed of discrete functional parts, either internally or at the surface, many of which have one or more dimensions of the order of 100 nm or less, including structures, agglomerates or aggregates, which may have a size above the order of 100 nm but retain properties that are characteristic to the nano-scale."
European Food Safety Authority (EFSA) (2009).	"Nano-scale refers to a dimension of the order of 100 nm and below [...] but there are size-related effects that can appear at larger size."
EC Scientific Committee on Emerging and Newly Identified Health Risks (SCENIHR) (2007). **SCENIHR (2009).**	"Engineered nanomaterial (ENM) is any material that is deliberately created such that it is composed of discrete functional and structural parts, either internally or at the surface, many of which will have one or more dimensions of the order or 100 nm or less (2007)." "It was also proposed the use of a limit of specific surface area (above $60m^2/g$) to regard a particulate substance 'nanomaterial' (2009)."

Kreyling, et al [8] point out that in broad size distributions the current nanoparticle definitions are difficult to apply, as they generally take in account only the average particle size. Most of the definitions also do not take into account nanostructure agglomerations, partially nanostructured materials and high surface area sub-micrometre particles [8].

As some materials may contain or accidently release a small amount of nanoparticles, it is important to correctly classify what can be considered or included in the nanoparticle definition, not only from the legal side but mainly to classify the risk associated with handling the materials and adequate the processes and exposure levels for minimizing the associated risk [2, 8].

Several attempts to correctly define a nanoparticle have been made throughout the years, taking into account agglomerates and suspensions, as well as limiting certain properties (at least a specific area ‘SSA’ of 60 m^2/g) [8]. There are particles that are sized under 100 nm that have a specific surface area under 60 m^2/g which are obviously nanoparticles. Therefore Kreyling, et al [8] propose limiting the minimum specific surface area per unit of volume ‘$VSSA$’ to 60 m^2/cm^3 as a way to complement the nanoparticle definitions. Doing so, these authors consider that it is possible to easily classify nanosized materials, nanostructured materials, as well as nanodispersions. The VSSA can be calculated by relating the ‘SSA’ [m^2/g], determined by BET procedure, and the material density ‘ρ’ [g/cm^3] by equation 1 [8]:

$$\boldsymbol{VSSA = SSA \cdot \rho} \qquad \text{(equation 1)}$$

An uncontrolled nanoparticles release may have a great impact on the environment and on the society itself. As most of nanoparticle toxicity studies are focused on the effects and impact of accidently discharged and inhaled nanoparticles originated by combustion processes, the effect of engineered nanoparticles remains obscure. As combustion generated nanoparticles are often considered as accounting for several health problems [3], the extrapolation that engineered nanoparticles have the same adverse effects cannot be ruled out without further toxicity studies. Considering the possibility of nanoparticle hazardous impacts it seems mandatory to characterize several nanoparticle parameters such as [2, 3]:

- Chemical composition and purity.
- Crystal structure and crystallinity.
- Particles size distribution and morphology.
- Specific surface area.
- State of aggregation.
- Surface condition (zeta potential, hydrophobicity/hydrophilicity, etc.).
- Solubility.
- Synthesis method and post-synthesis changes.

The three pathways for obtaining nanoparticles imply a solid to solid or a liquid to solid or a gas to solid conversion. Examples as high energy milling, sol-gel process and vapour phase deposition are popular approaches (table 3) for nanoparticle production. However for bioaplications a strict control of particle size and topography is required and most of these techniques do not respond as desired to these needs. In many solution routes the use of surfactants, capping agents and templates has been useful for controlling the size and the shape of the nanoparticle [6].

Table 3. Nanoparticles production methods, adapted from [6].

Processing method	**% of use**
Physical vapor deposition	10
Colloidal chemistry	25
Mechanical alloying	10
High energy milling	22
Chemical vapor deposition	> 20
Sol-gel	35
Mechanical grinding	20
Solvothermal	> 6
Supercriticl fluid precipitation	9
Biological/biomimetic	9
Flame pyrolysis	6
Laser ablation	12
Ultrasound	< 3
Electrodeposition	> 9
Electro-explosion	< 3
plasma synthesis	3
Microwave	< 3
Other precipitations	< 3

However the available options for producing nanoparticles with controlled particle shape and size are limited to a few (table 4), often needing additional steps like calcination or milling that are prohibitively expensive and ruinous for the sake of morphology control. Therefore the development of simpler and effective synthesis processes, ideally at low temperature is required to further supply the demand. From this point of view chemical solution precipitation methods appear very attractive and worthy of research investment. [9].

Table 4. Comparison the effectiveness of nanoparticles processing techniques, adapted from [9].

Parameter	Solid state reactions	Precipitation	Sol-gel	Polymerizable complex	Solvothermal
Cost	L to M	M	H	H	M
Development	C	D/C	R&D	R&D	R&D/D
Control:					
- Composition	P	G	VG	VG	G/VG
- Morphology	P	M	M	M	G
Powder reactivity	P	G	G	G	G
Purity	< 99.5	> 99.5	> 99.9	> 99.9	> 99.9
By steps:					
- Calcination	multiple	maybe	yes	yes	maybe
- Milling	multiple	maybe	yes	yes	no

L: low; M: moderate; H: high

C: commercial; D: demonstration; R&D: research and development

P: poor; G: good; VG: very good

B. Nanocomposites bioapplications

There are several applications benefiting from the combination of polymers and nanoparticles properties as found in many different areas as tissue engineering, specifically in nerve guide channels and bone implants, or in other fields as antimicrobial materials. The next section will review few representative examples of such applications.

B1. Nerve guide channels

In the late 80's tissue engineering research grew exponentially, namely nerve regeneration therapy [10]. Current grafting techniques can be summarized as [11]:

- Autografts: the graft is collected from the patient's body bearing full biocompatibility and no immune response. Being, considered as a gold standard its drawbacks are related to its limited availability.

- Allografts: this type of graft is provided by a donor other than the patient and although it has the same capabilities as an autograft, the immune response may be superior, the availability is also low and there is an associated risk of disease transmission.

- Xenografts: for this type of graft the implantation source is other species, and it carries itself an increased immune response probability and higher disease transmission risk.

As each of these approaches poses some risks, particularly the used materials in allograft or xenograft and the lack of reliable sources, the development of mimetic materials seems to be a promising approach. In the last decade nerve tissue regeneration strategies have been revised because clinical trials did not confirm the growth factors effects observed in *in vitro* studies. Some difficulties emerged also from other issues such as the cellular complexity of the nervous system which requires different approaches for different cell types, or the difficulties of transposing laboratory modelling to the operation site [10].

Early attempts of nerve defects repair often resulted in failure. However as micro-surgery concept was consolidated, the trials success rate improved allowing the individual alignment of the nerves and minimizing the tension generated from stretching and suturing the two nerve ends directly. For the successful achievement nerve guide channels play an important role. Guide channels are tubes within which the two ends of a damaged nerve are allowed to grow and attach and thus recover faster. There may exist a lot of materials that can be possibly used as guide channels. However some key properties are required such as [5, 10]:

- To be easily processed for allowing the achievement of the desired diameter and wall thickness.
- To be of simple implantation through microsurgery.
- To be sterilizable.
- To be biocompatible and biodegradable.

Permanent inert materials, as opposed to biocompatible and biodegradable materials, can also be used in nerve repair strategies, but not only they carry higher risk of infection, they also elicit connective tissue responses, can compress nerves or become dislodged [10].

The peripheral nerve tissues ‘PNS’ may spontaneously recover or are easier to be aided in recovery (figure 3A). Contrarily central nervous system ‘CNS’ tissues generally need the aid of guide channels to regenerate, as there are several factors such as inhibitory cues or absence of stimulatory cues that prevent spontaneous tissue recovery (figure 3B) [5].

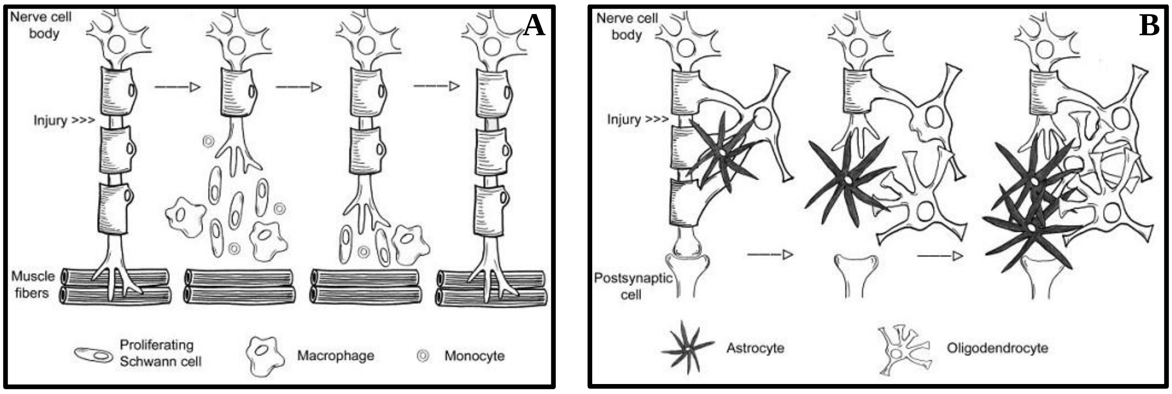

Figure 3. Illustration of the nerve regeneration process: A) spontaneous peripheral nerve system (PNS) recovery. B) Central nervous system (CNS) auto-inhibition, adapted from [12].

Synthetic materials are a promising choice to replace the autologous material and its associated risks, as it is possible to incorporate several strategies as cell transplants, topographic and electrical stimulation. These strategies alone have been proved to work well but their combined efficiency is not known yet in nerve guide channels, thus requiring further studies to develop and evaluate the next generation of nerve guide channels [5].

B2. Bone implants

In our current society bone fractures and several bone diseases, like cancer, osteoporosis, and osteoarthritis are becoming more and more common, due to the increased human life expectancy and to the modern life style. The limited life time of the common implants results from several issues like implant loosening, inflammation, infection and debris release, which makes urgent the development of novel materials able of a better bone bonding with larger life time and bone regeneration abilities [13].

These objectives have pushed orthopaedic medicine to study bone tissue regeneration and growth, as osseous defects greatly influence human quality of live and longevity. Biologically bone tissue is a very dynamic and extremely complex system, with a great regenerative capacity. Bone tissue is composed of a myriad of interleaved components which give rise to a complex structure. Healthy bone is roughly composed by 70% of a nanohydroxyapatite mineral phase and by 30% of collagen organic phase. Other elements present in smaller quantities include citrate, carbonate, sodium, magnesium, zinc, potassium and a wide variety of noncollagenic proteins [14].

The needs underlying the regeneration of severe bone defects resulting from traumas, tumours or anomalies require the application of implants or grafting techniques (autografting, allografting, xenografting). To date the limitations to these techniques come from the unavailability of the biological material, the immunologic adverse responses or from the inadequacy of the synthetic materials [14].

There is a need to develop new grafting materials able of mimicking the biological components ability to [14, 11] induce osteoblasts adhesion and proliferation as well as vascularisation [15].

It was observed that electric current promotes osteogenesis, and thus it has been hypothesised that the internal forces induced by an external electric field generate electric signals that transport information to bone cells allowing the regulation of their biological functions [15]. Collagen fibers are aligned polar proteins, and thus when deformed they generate an electrical current and vice-versa (piezoelectricity). It has been proposed that piezoelectricity may have a fundamental role in bone growth, remodelling and regeneration. Piezoelectric materials with mimetization capabilities are attractive an approach in skeletal regeneration [16].

B3. Inert bioimplants

Sometimes an approach different from that intended to the promotion of cell adhesion and proliferation may be required. In many devices, like catheters, heart valves or sensors, among the various failure reasons are the interactions at the body/material interface like the adhesion and proliferation cells which are not desired at the body/material interface. Catheters are particularly prone to bacterial film formation and subsequent infection especially in a long term usage. This film is formed soon after implantation, a process called *surface conditioning*, and its composition is manly conditioned by the chemical nature and the design of the implant. The main problem is that even non-pathogenic entities may cause infections which require the removal of the implant with its associated risks. Therefore the development of new materials able of reducing the bacterial film formation and the interaction with body fluids is needed in order to improve implant life and body acceptance [17].

1.2. Zinc oxide

Zinc oxide (ZnO) is a binary semiconductor that in normal pressure and temperature condition crystallises preferably in Wurtzite hexagonal structure (figure 4) and appears in nature as zincite mineral. The hexagonal ZnO belongs to the space group $P6_3mc$ or C_{6v}^{4}, point group 6 mm or C_{6v} and its typical lattice are [18, 19]:

$$a = b \neq c$$
$$a = 3{,}2495\ \text{Å}$$
$$c = 5{,}2069\ \text{Å}$$

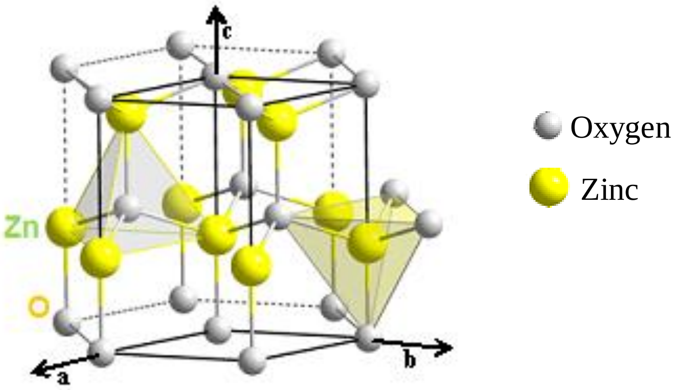

Figure 4. ZnO wurtzite hexagonal structure, adapted from [URL1].

Each ion present is tetrahedrically coordinated, meaning that an ion is surrounded by four ions of opposite signal, and the distribution occurs in ab plane intercalated sheets of cations ‘Zn^{2+}’ and sheets of anions ‘O^{2-}’ along the c axis [18, 19].

The terminal surfaces of this crystalline structure in the c axis are the (0001) of Zn^{2+} cations and the $(000\overline{1})$ of O^{2-} anions. The strong polarity of these terminations gives rise to like piezoelectricity or spontaneous polarization. The chemical bond classification lies between pure covalent and pure ion as in this material exists sp3 bonding as well as a strong ion character in the Zn-O bonding [18, 19].

The interest in ZnO for optoelectronics application lies in properties such as a wide band gap (~3,37 eV) or large exciton binding energy (~60 meV). As the work wavelength of ZnO lies between ultraviolet (UV) and blue radiation, ZnO research was electronic oriented and it was based almost solely bulk properties (i.e. crystal growth, doping, band structure, lasers or sensors) [18, 19].

A. ROS formation

Reactive oxygen species (ROS) can spontaneously form in the nanoparticles surface, more particularly in the crystalline defect present in them. Generally they appear by reaction in the materials surface of adsorbed oxygen species and electron/hole pairs. The more electron/hole pairs exists in the material surface the more ROS are formed. This can be enhanced by rising the number of interstitial zinc that leading to electron/hole pairs ‘$e'/h^{\cdot}$’ [20].

Typically these electronic species can be achieved by irradiating the material with electromagnetic radiation, namely UV, promoting valence electrons to the conduction band leaving behind the corresponding holes. With nanoparticles it is expected that with the increased of surface area the site defects (i.e. interstitial Zn) also increase leading to more available electronic defects even in the absence of radiation [20].

Even if the mechanisms of ROS formation are not fully understood several mechanisms have been proposed. One of those will be used to illustrate what possibly happens in aqueous solutions (Figure 5) (electronic species e' and $h^{\cdot}$ are written in Kröger-vink notation and radical species are noted with a dot ‘·’ on the left to avoid misinterpretations) [20].

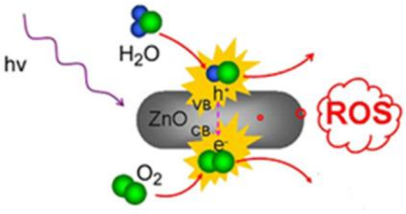

$$\boldsymbol{H_2O + h^{\cdot} \rightarrow H^+ + \cdot OH + O_2 + e^{'} \rightarrow \cdot O_2^-} \tag{1}$$

$$\boldsymbol{\cdot O_2^- + H^+ \rightarrow \cdot HO_2 + e' \rightarrow HO_2^-} \tag{2}$$

$$\boldsymbol{HO_2^- + H^+ + e' \rightarrow H_2O_2} \tag{3}$$

Figure 5. ZnO ROS production mechanism, electronic species $\boldsymbol{e'}$ and $\boldsymbol{h^{\cdot}}$ are written in Kröger-vink notation and radical species are noted with a dot ‘·’ on the left to avoid misinterpretations, adapted from [20, 21].

Through UV radiation one electron/hole pair is formed in the material surface. The electronic hole '$h^{\cdot}$' reacts with one water molecule to form the ion pair 'H^+/OH^-' while the free electron 'e'' reacts with one oxygen molecule to form the superoxide radical anion '$\cdot O_2{}^-$' (1). The '$\cdot O_2{}^-$' radical may react with the 'H^+' ion forming the hydroperoxyl radical '$\cdot HO_2$' that may further react with another free electron originating the hydrogen peroxide anion '$HO_2{}^-$' (2). The reaction can end if a peroxide molecule 'H_2O_2' is formed by the reaction of the 'H^+' ions and '$HO_2{}^-$' (3) [20].

B. Bio zinc oxide

It is expected that with particle size reduction below the nanometre range, namely sub micrometre and nanometre, that the materials properties are greatly enhanced and improving and potentiate their applicability in the biomaterials area. In this area the cytotoxic effects of ZnO nanoparticles are not fully known and therefor it is a major topic in biomaterials research and investigation [1-4].

Nanoparticles properties can be adverse to biological systems, but several studies shows the possibilities of their usefulness to potentiate and valorise those same properties in biological applications to improve the humankind quality of life. ZnO appears to have a great potential to be a key item in biomedical applications, namely in controlled drug delivery, cellular regeneration or biomarker, and therefor ZnO nanoparticles cytotoxicity must be fully evaluated so its effect can be known [4].

It is accepted that ZnO cytotoxicity (figure 6) is related to two fundamental factors [4]:

- Surface effects: ROS release form the particles surface that reacts with cellular walls and breaks them by means of lipid peroxidation, exposing the cellular nucleus. ROS can then penetrate the cell and react with nucleic acid and proteins (i.e. enzyme deactivation). Even cells with great anti-oxidant potential can be broken and enter oxidative stress if the natural antioxidants are fully depleted.

- Mechanical effect: Stress originated from the interface particle/cell and it is related with the size and form of the particles.

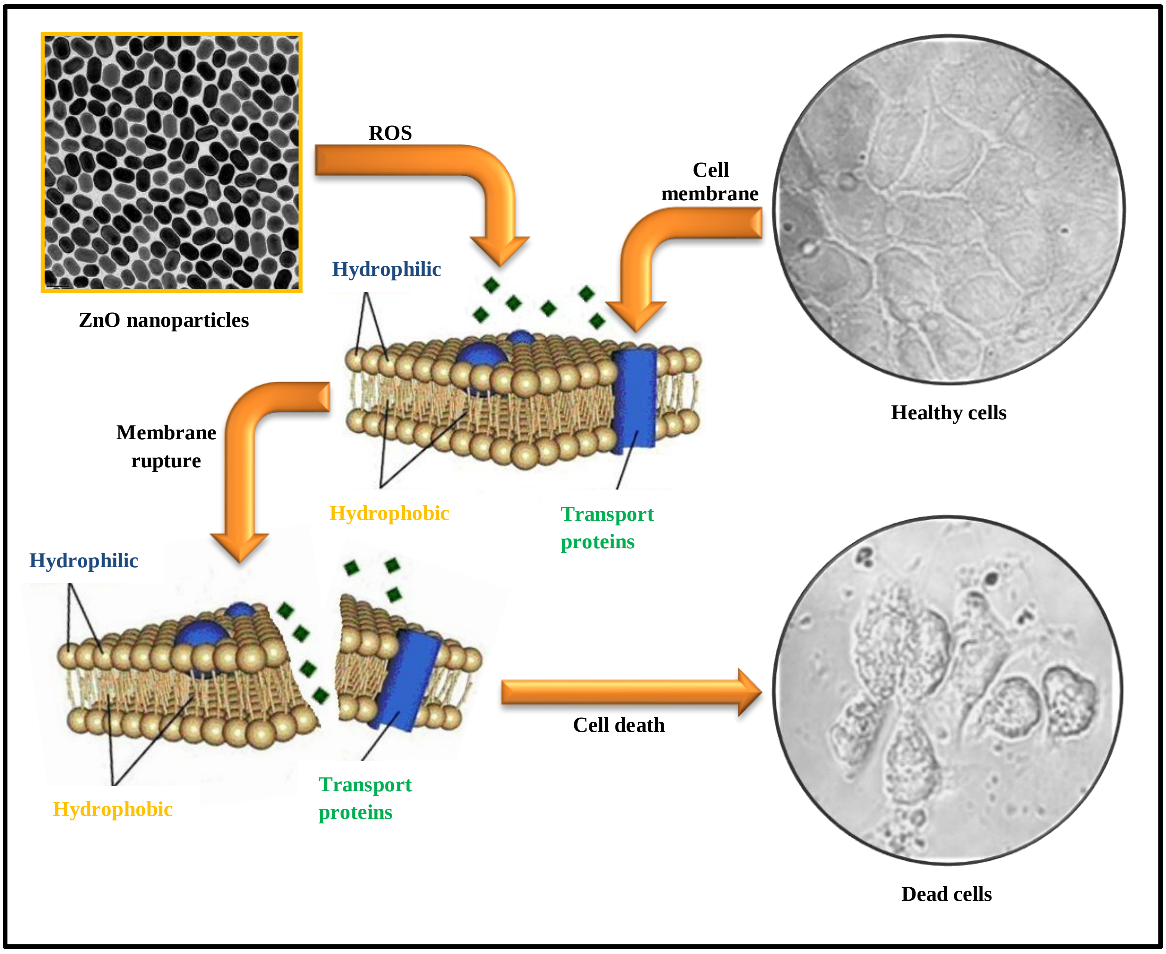

Figure 6. The effect of ZnO cytotoxic mechanism in cells [22].

B1. Controlled drug delivery systems

Nanoparticles have the advantage of being in the same size order of biomolecules or biological structural units, and by so they can dynamically interact with the cellular surface or interior or penetrate barriers that micrometre particles can't. This was possible by the advances, in recent years, of the comprehension of the human body to the molecular and nanometric levels but the treatment methods that could benefit from this knowledge didn't follow this lead [23].

Currently none or few alternatives exist to chemo/radiotherapy in cancer disease treatment. Both treatments are often accompanied by several adverse effects, such as medullar tissue suppression, neurotoxicity and poor selectivity, as its administration can hardly be called local. Nanotechnology and nanomedicine open new doors in focussed treatment which could obviate these troubles as nanoparticles can act as an active principle, drug carrier or both [23].

B1.1. Selective cytotoxicity

When Cory Hanley, et al [23] investigated the effect of ZnO exposition in cultures activated T cells lines it was observed that to a concentration of 10 mM of ZnO activated T cells were less viable than the non-activated counterparts. Further, in complementary tests of co-cultures of cancerous cells and healthy cell lines viability of the cancerous ones were several times less than the healthy ones. It is also verified that the cytotoxicity of ZnO nanoparticles is dose dependant, as with increased dose cytotoxicity of the system increases to both types of cells, but there is an evident selectivity of toxic effects to the unhealthy cell lines. Other tests indicate that ZnO nanoparticles induce cell apoptosis by means of ROS, which leads to say that the toxicity is in fact related to the proliferation rate of the exposed cells (cancerous replicate extremely fast) [23]. Other authors observed the same pattern and behaviour in other systems, namely Mariappan Premanathan, et al [24] in cultures of leukaemia cells (HL60) and mononuclear blood cells (PBMC), stating that ZnO nanoparticles exert a strong cytotoxic effect on the leukaemia line, inducing apoptosis through lipid peroxidation [24].

B1.2. Synergy action

Photo dynamic therapy (PDT) is currently being studied as a mean to obviate cancer’s normal treatment methods. If the cells are resistant to chemicals and drugs normal treatment methods can be inhibited. The action of a specific wave length radiation on a photosensitiser located in specific target sites will promote the release of ROS with capability do destroy and avoid the proliferation of malignant cells. [4].

As zinc oxide is a known photosensitiser, Dadong Guo, et al [4] studied the synergetic effect of ZnO NPs loaded with daunorrubicin drug in PDT of leukaemia multiresistant cancer cell lines. The cytotoxic effect of ZnO NPs was observed on both cell types (leukaemia and multiresistant counterparts), and the action on both cell lines was the same at higher concentrations. The effect is enhanced by the radiation as the ROS released from ZnO NPs break the cellular wall resulting in cytoplasm efflux, more drug and ROS cell penetration which results in cell death [4]. The same phenomenon was observed by Jingyuan Li, et al [25] and Haijun Zhang [21] in other types of cell lines.

B1.3. Role of particle size

Particle size may influence the material cytotoxicity, especially in nanometre scale. Dadong Guo, et al [4] observed practically no difference in the toxicity of 20, 60 and 100 nm particles at the same concentrations in leukaemia normal and multiresistant cell line [4].

However at concentrations above 25 µg/ml cell viability greatly decreased on both types of cultures, but being more pronounced in multiresistant leukaemia cell line [4].

On the other hand Shantikumar Nair, et al [26] observed that cytotoxicity had a strong dependency on the particle size in cultures on cancerous osteoblasts. In their investigations at low concentrations smaller size particles were more cytotoxic but at higher concentration levels the behaviour of those same particles was the same. Particles under 350 nm were more effective at lower concentration than micrometric particles, as the toxic behaviour can be seen at 100 µM and it reaches the maximum at 500 µM [26].

B1.4. Role of particle morphology

As the size of particle may influence toxicity of NPs, particle morphology can also influence NPs toxicity. Rizwan Wahab, et al [27] investigated the influence of the concentration of several types of nanostructures (NS) in U87 and HeLa cell lines. The NS investigated were microflowers of nanorods (MFR), microflowers of nanosheets (MFS) and nanoparticles aggregated microspheres (NAM) that were compared to loose nanoparticles [27].

These authors, as the others mentioned above, observed that NP and NS cytotoxicity in both cultures rise in a dose dependent way. These authors also observed that NAM and MFS were more toxic than nanoparticles alone and MFR. According to these authors nanoparticles morphology can be related to cytotoxicity, but further studies are still needed in determining the specific effect and mechanisms behind this influence [27].

B1.5. Role of zinc ions

Zinc oxide has low solubility in aqueous medium, but some authors point out the possibility that the 'Zn^{2+}' ions originated from the nanoparticles dissolution may influence and actively participate on the cytotoxicity of ZnO nanoparticles [28].

W. Song, et al [28] show that when Ana-1 cell lines are exposed to NPs concentration below ZnO solubility the cells are more exposed to 'Zn^{2+}' ions and therefor they associate the toxicity to this ion. When the cell lines are exposed to NPs concentration above ZnO solubility the cation concentration is so low that their contribution practically irrelevant, in favour of the effects associated with particle specified above [28].

On the other hand P. J. Moos, et al [29] didn't found any correlation between 'Zn^{2+}' cation release on the ZnO cytotoxicity in RKO colon cancerous cell lines and affirm that to those cells cytotoxicity is due to particle cell contact.

In agreement with P. J. Moos, et al [29], M. Ahamed, et al [30] also didn't attributed ZnO NPs cytotoxicity to the cations released from nanorods in contact with A549 cell lines. It is however observed that the cytotoxic effect of higher concentration of this ion is lower that the oxidative stress imposed by the same amount of ZnO nanorods.

B2. Antibacterial/fungi properties

ZnO particles also have antibacterial/fungi properties, as O. Yamamoto [31] finds a string size a concentration dependency on antibacterial activity in *Escherichia coli (E. Coli)* and *Staphylococcus aureus (S. aureus)* bacteria cultures. The effect of particle size reduction from 800 to 100 nm was more pronounced in the *E. Coli* bacteria colony [31].

The proposed action mechanisms of antibacterial activity are attributed to [26]:

- ROS release from the particles surface
- Ion release from the particles surface
- Bacteria cell membrane rupture
- Internalization of the particles

As a photo-active material, ZnO antibacterial studies often rely on UV radiation of the material, which shows the importance the ROS released on the fotocatalitic activity of the material. On the other hand there are some reports that even without the UV radiation this material presents inhibitory properties relatedly to *E. Coli* bacteria [26, 32].

Taking into account another route, S. Nair, et al [26] discuss the effect of surfactant agents on the antibacterial properties of NPs, as diethyleneglycol surfactant for example can damage gram-positive *S. Aureus* bacteria's membranes undermining the evaluation of the effect of NPs themselves. It is quite relevant to determine if the surfactant has any effect on these properties as it may unintentionally come from the NPs production stage. There are studies that indicate that polyethyleneglycol acts as free radical trap site obstructing their action on bacteria's membranes leading to antibacterial activities in the interaction particle/membrane. On this account there is an increased effect on gram-negative *E. Coli* than in gram-positive *S. Aureus*, possibly attributed to the thicker membrane which resists more effectively to the mechanical action of ZnO NPs [26].

Conversely M. Premanathan, et al [24] observed a stronger effect on the gram-positive *S. aureus*, when they studied the antibacterial activity in *E. coli*, *Pseudomonas aeruginosa (P. Aeruginosa)* e *S. aureus* strains, possibly to the inexistence of surfactant agents which allows the action of other mechanisms besides the mechanical action [24].

B3. Bone tissue regeneration

In search of new biomimetic materials it was found that the ‘Zn^{2+}’ ion besides being osteoconductive stimulates also osteogenesis [33]. Zinc is also a trace element in bone structure, and is often associated with bone development, as it intervenes in the calcification mechanism, participates in numerous biological phenomena, and zinc deficiency promotes late bone growth [34]. ZnO nanoparticles appear as a biomimetic particle that could supply the bone surround with ‘Zn^{2+}’ ions and induce osteoconduction by its piezoelectric properties.

J. K. Park, et al [35] observed the growth and osseointegration of MC3T3-E1 osteoblasts cell line in ZnO nanoflowers deposited in silicon substrates. These authors observed a rapid proliferation of the osteoblasts throughout the ZnO nanostructures potentiated by the samples roughness. *In vivo* evidence shows that it possible to integrate this material in live bone matrix and that ZnO may have an active role in adhesion, proliferation and growth bone matrix [35].

B4. Nerve guide channels

Biomimetic materials capable of better interactions with the body are needed to improve current guide channel implants, and by so the approach of multi-stimuli is being investigated [12]. This way nanoZnO polymer composites can be engineered into scaffolds that mimic the natural neural support tissue with the possibility of electrical charge neuron regeneration aid. ZnO nanoparticles natural antibacterial properties may reduce infection risks associated with the implantation of the device. J. T. Seil and T. J. Webster (2008) have studied a polyurethane/ZnO nanocomposite for as nerve guide channel in CNS recovery. These composites not only possess two of the mentioned strategies they also have the characteristic of decreasing astroglial cell adhesion and proliferation, the cells that create the most prominent factor that alts the CNS regeneration, the glial scar [5].

1.3. Polyurethane

Polyurethanes (PUs) are a vast family of synthetic polymers of complex chemical structure when compared with simpler polymers, such as polyethylene or polypropylene. The complex structure is formed when three distinct monomers are combined through specific chemical reactions originating the polymer chains. The monomers, diisocyanate, macroglycol and chain extender, can react and organize in multiple ways, giving rise to an infinity of materials with distinct mechanic and physico-chemical properties. The versatility of these materials arises from the fact that it is possible to alter its chemistry depending on the needed application. The changes can be carried out by altering either the raw materials or the processing conditions [36].

PUs were first synthesized in 1937 by Otto Bayer and coworkers and till today have been typically applied as elastomers, foams, adhesives and paints. Besides the named applications, polyurethanes found niche market as a biomaterial as they possess unique mechanical properties, especially fatigue resistance. The biological response and bio-stability of these materials is conditioned by the surface properties, and those are greatly influenced by the chemistry and synthesis procedure, as both variables influence the composition and distribution of the carbonated chains through the material [36].

A. Polyurethane's chemical structure

The combinations of the diisocyanate, polyol and chain extender originate two different micro-domains that typically characterise a PU. One is a hard segment originated by the reaction of diisocyanate and chain extender and the other is a soft segment originated by the oligomer polyol. Typical polyurethanes can be represented by [37]:

$$\boldsymbol{P - (D(CD)_n - P)_n}$$

Were '$\boldsymbol{P}$' is the polyol, '$\boldsymbol{D}$' the diisocyanate and '$\boldsymbol{C}$' the chain extender. As these three elements can be differently combined, the PUs properties will depend of the hard/soft segment ratio and the monomers nature [37].

A1. Diisocyanate

The diisocyanate is a chemical compound of low molecular weight with two isocyanate terminal groups. The isocyanate terminations allow this monomer to chemical bond to a polyol or chain extender forming linear chains, or ramifications if more isocyanate groups are added, either aliphatic or aromatic. From the industrial or biomedical point of view diphenylmethane-diisocyanate (MDI) (4), hydrogenated diphenylmethane-diisocyanate (HMDI) (5) and toluene diisocyanate (TDI) (6) are the most important ones.

$$OCN-(C_6H_4)-CH_2-(C_6H_4)-NOC \tag{4}$$

$$OCN-(C_6H_{10})-CH_2-(C_6H_{10})-NOC \tag{5}$$

$$CH_3-(C_6H_3)-(NCO)_2 \qquad \textit{(NCO bonded to carbons 2,4 or 2,6)} \tag{6}$$

Polyurethane synthesis works by either reactions of urethanes links formation, as an isocyanate terminal group reacts with hydroxyl groups (polyol or chain extender (7), or by urea links formation if a diamine is used as chain extender (8) [36].

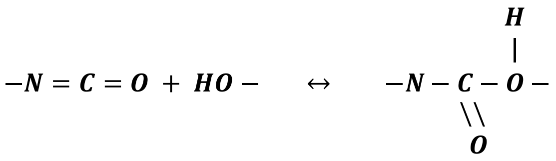

$$-N=C=O\ +\ HO- \quad \leftrightarrow \quad -N-\underset{\substack{\backslash\backslash\\ O}}{C}-\overset{\substack{H\\ |}}{O}- \tag{7}$$

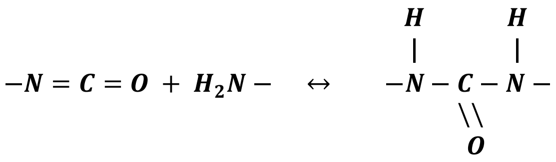

$$-N=C=O\ +\ H_2N- \quad \leftrightarrow \quad -\overset{\substack{H\\ |}}{N}-\underset{\substack{\backslash\backslash\\ O}}{C}-\overset{\substack{H\\ |}}{N}- \tag{8}$$

Isocyanate groups are so reactive that they easily react with hydrogen in acid medium and can originate either a foam or high urea content, and so reactions with water (9) should be avoided as they will lead to by-products formation, not always desired [36].

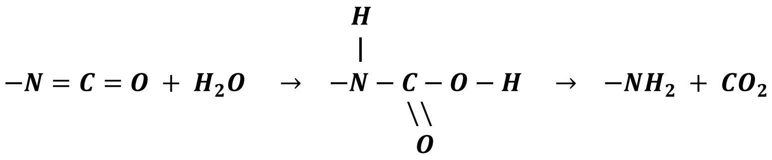

$$-N=C=O + H_2O \rightarrow -\overset{\overset{H}{|}}{N}-\underset{\underset{O}{\backslash\backslash}}{C}-O-H \rightarrow -NH_2 + CO_2 \tag{9}$$

The near perfect packing of the ring structures $[-(C_6H_4)-$ or $-(C_6H_{10})-]$ present in the diisocyanate and the strong intermolecular interactions, namely hydrogen and urethane groups bonding, give rise to rigid microdomains in opposition to the polyol part. The segregation of the hard segment segregation from the bulk is dependent on the type of monomer used, and determines the microdomains formation, crystallinity and the mechanical properties of the compound. Chain packing is also influenced by the size, symmetry and ring rotation, in a way that compact, rigid and symmetrical diisocyanate molecules leads to better packing than asymmetric and flexible ones, and by so increases the mechanical properties. The bulk properties also depend on the type of ring presented by the diisocyanate. The rigidity of the molecule is higher in the presence of an aromatic ring as the π electrons delocalization through the ring does not allow boat/chair conformations making the molecule stiffer [36].

A2. Polyols

The polyol monomer is the polyurethane chain soft segment former. Polyols are oligomer macromolecules with hydroxyl terminal groups and have repeating units based on polyether or polyester, (10) and (11) respectively [36]:

$$HO-[R-O-R']_n-OH \tag{10}$$

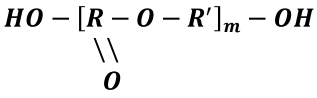

$$HO-[\underset{\underset{O}{\backslash\backslash}}{R}-O-R']_m-OH \tag{11}$$

In which 'OH' is the hydroxyl group, 'R' e 'R'' are carbonated chains, 'O' is oxygen and 'n' and 'm'the number of monomers. The aliphatic structure and low intermolecular interaction allows the macromolecules some degree of rotation and bending by which segregation from the bulk originates soft microdomains. Branched or reticulated structures are obtained by the use of more hydroxyl groups per molecule. [36].

Typical polyol macromolecules are polytetramethylene ether glycol (PTMO, PTMEG or PTMG) (12), polypropylene glycol (PPG) (13), polyethylene adipate (PA) (14) and poly(1,6-hexyl 1,2 ethyl carbonate)diol (PHECD) (15).

$$HO-[(CH_2)_4-O-]_n-H \qquad (12)$$

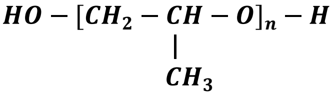

$$HO-[CH_2-\underset{\substack{| \\ CH_3}}{CH}-O]_n-H \qquad (13)$$

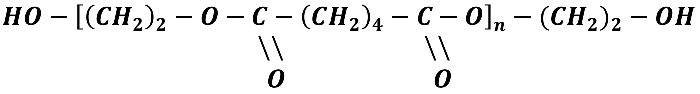

$$HO-[(CH_2)_2-O-\underset{\substack{\backslash\backslash \\ O}}{C}-(CH_2)_4-\underset{\substack{\backslash\backslash \\ O}}{C}-O]_n-(CH_2)_2-OH \qquad (14)$$

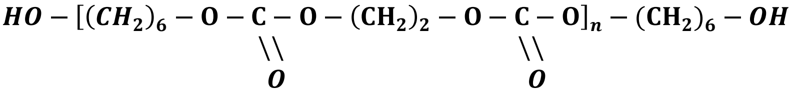

$$HO-[(CH_2)_6-O-\underset{\substack{\backslash\backslash \\ O}}{C}-O-(CH_2)_2-O-\underset{\substack{\backslash\backslash \\ O}}{C}-O]_n-(CH_2)_6-OH \qquad (15)$$

Chain packing of polyols also influences the mechanical properties of the polymer, and it is achieved by structural regularity and symmetry of the molecule [36].

Chemical or hydrolytic degradations are extremely influenced by the polyol choice. Polyester-urethanes hydrogen bonding through ester groups enhances the mechanical properties of the bulk at the expense of an increase in hydrolytic degradation susceptibility. The alternative, polyether-urethanes, are highly chemical resistant with oxygen bond cleavage occurring in acidic medium, which prevents hydrolytic degradations, but instead they oxidize in contact with air [38] with release of peroxides and impoverishment of mechanical performance [36].

A3. Chain extender

The chain extender is a hydroxyl or amino terminated small molecule that plays a key role in the mechanical properties of the PUs. The direct reaction of polyols and diisocyanates often results in soft rubber. When the chain extender molecules react with the diisocyanates ones they form a hard segment that segregates from the bulk, which acts as both a filler and reticulation spot increasing the overall mechanical properties. Polyurethane or polyurethane-urea can be achieved by using either dyols or diamines respectively, typically 1,4-buthanediol (BD) (16) or ethylenediamine (ED) (17) [36].

$$HO-(CH_2)_4-OH \tag{16}$$

$$H_2N-(CH_2)_2-H_2N \tag{17}$$

The mechanical resistance of the polyurethanes is influenced by the type of chain extender molecules that act in the same way as the polyol. Another key aspect is the monomer concentration, as a large concentration originates a large quantity of hard segments by diisocyanate reaction and microdomain segregation, leading to harder, stiffer and more resistant polyurethanes [36].

B. Thermal history

Hard and soft micro-domain distribution depends not only on composition but also on the thermal history of the polyurethane. PUs based in MDI/BD, for example, form semi-crystalline compact domains during annealing, but a change in micromorphology may occur if stretching is also applied. As the micro-domains take an elongated shape, the melting point of the bulk material also changed to lower values. Polymorphs can also form during the material processing which may impact the final properties of the material. The mechanical and thermal properties of a PU may be highly affected by the bulk thermal history [36].

C. Polyurethanes bioaplications

The selection of a biomaterial should be made by finding a material which suits the application, taking into account that their characteristics and behaviour should be as proximate as possible to the chosen substitution part. The bio-stability and biological response characteristics, often determined by surface properties, are the decisive criteria when choosing a biomaterial. In this way mechanical properties are often disregarded as it is difficult to balance them with the host response and the high clinic requisites [36].

Polyurethanes are regarded as heterogeneous materials because of the two distinct micro-phases segregation that occurs in the bulk. The hard/soft segment segregation appears due to the nature of the antagonistic interactions between the polar urethane and the non-polar polyol segments. The segregation may preferably take place in certain locations depending on the interface polymer surface/surrounding environment. In this way when the polymer is surrounded by hydrophobic medium, such as air, the non-polar soft segment rises to the surface. Contrarily if surrounded by biological fluids (hydrophilic) the hard segments are the ones that segregate in the bulk surface. This indicates that the surrounding environment changes the surface characteristics of bulk polyurethanes and by doing so it also changes its biological response [36].

Biocompatibility of PUs has been reported in several studies. B. Saad, et al [39] produced PU formulations that didn’t induce cytotoxicity and were able to promote the adhesion, growth and activity of fibroblasts (3T3 cell line) demonstrating the usefulness of PU in bone implant fixation.

Besides bone implants [40], polyurethanes are widely used as inert materials in many biomedical devices, such as heart valves [41] or catheters.

Controlled drug delivery systems (CDDS) may be achieved by (bio)degradable polyurethanes. E. Jabbari and M. Khakpour [42] have shown that polyurethane microspheres can effectively be used in CDDS, and also proved that changes in chain extender concentration can drastically alter the polymer matrix porosity, a relevant parameter in engineered biomaterials. The authors showed that till 50% molar of chain extender there was a reduction in the pore size from 950 to 600 nm as the chains lose their mobility. For higher concentrations, namely 60 and 67%, the chains became stiffer and porosity formation was inhibited [42].

The use of biodegradable polyurethanes instead of an inert matrix can be very interesting in delivery systems as they convert themselves into simpler organic products that can be mineralized and redistributed through biological cycles (carbon, nitrogen and sulphur) [43]. A challenging proposal by W. N. Sivak, et al [44] suggests that instead of loading the drugs (one or more) in the matrix, they could be chemically bonded to carbonated chains of a biodegradable PU. The authors stress that the implantation of such a device will gradually degrade along time releasing the drugs in a much more controlled way [44].

Chapter II

2. Materials & methods

2.1. Procedure

All the reagents and materials were used as purchased without any further purification. The Zn salt used was a 136.28 g/mole molar mass zinc chloride (Merck) and the chelating agent was a 210.14 g/mole molar mass citric acid monohydrate (Riedel-de Haën and Sigma-Aldrich). Zinc oxide commercial nanosized powder (<100 nm) was acquired from Sigma-Aldrich (denominated cZnO) and polyurethane pellets (medical grade tecoflex SG80A polyurethane) were acquired from Fluka analytical. ZnO nanoparticles suspensor was a Fluka analytical 1,2-dichloroethane, polyurethane solvent was a Carlo Erba reagents chloroform. The base used was Akzo Nobel sodium hydroxide pellets and the absolute ethanol was a Carlo Erba reagents absolute ethanol. The tecoflex SG80A polyurethane and ZnO particles are food and drug administration (FDA) approved products. The polymer used, tecoflex SG80A, is a HMDI (diisocyanate), PTMEG (macrodiol) and BDO (chain extender) based linear polyurethane suitable for solvent evaporation casting, with a typical chemical structure (figure 7). According to the products data sheet this polyurethane properties can be found in table 5 [45]:

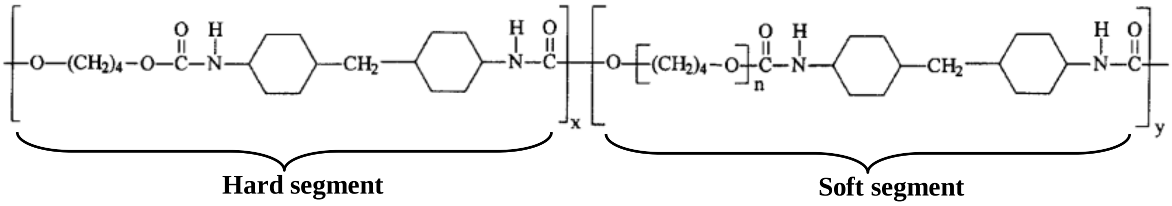

Figure 7. Typical Tecoflex SG80A PU chemical equation, adapted from [46].

Table 5. Thermedics tecoflex SG80A PU reference properties, adapted from [45].

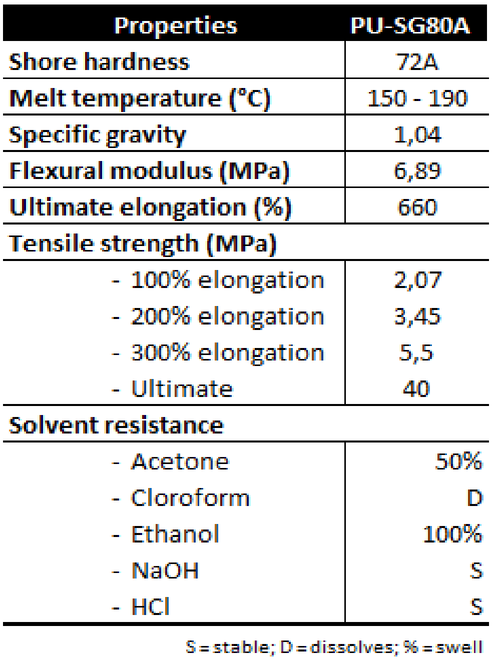

Properties	PU-SG80A
Shore hardness	72A
Melt temperature (°C)	150 - 190
Specific gravity	1,04
Flexural modulus (MPa)	6,89
Ultimate elongation (%)	660
Tensile strength (MPa)	
- 100% elongation	2,07
- 200% elongation	3,45
- 300% elongation	5,5
- Ultimate	40
Solvent resistance	
- Acetone	50%
- Cloroform	D
- Ethanol	100%
- NaOH	S
- HCl	S

S = stable; D = dissolves; % = swell

A. Nanoparticles production & characterization

Different types of ZnO particles were obtained by a chemical precipitation method. The dissolution of citric acid (Cit) and zinc chloride [(Cit)/($ZnCl_2$) molar ratio = (3:1) to ensure the chelation of Zn^{2+} ions] in 20-25 ml of deionized water under vigorous stirring was the common step to all the used precipitation procedures. Such solution will be referred as stock solution. The Zn concentration in the stock solution was 1.89 mmol/ml. After 20 minutes of stirring the stock solution was clear and fully transparent. Three types of powders were produced by changing the processing conditions (figure 8):

Method A: NaOH solution (10 molar) was added in a drop wise manner at an average rate of 6.15 ml/min to the stock solution under vigorous stirring till the formation of a white precipitate at pH 13.5. The final Zn/Na ratio in the precipitating medium was 0.3 (m/m) The precipitate was filtered and washed with deionized water and then dried at a moderate temperature (50 to 110 °C). This powder will be referred as pZnO.

Method B: A second type of powder was obtained by adding an ethanolic solution of NaOH (43%$_{(v/v)}$ ethanol) to the stock solution using the same adding rate as referred for pZnO so as to achieve a final Zn/Na ratio of 0.3 (m/m). The formed white precipitate was centrifuged and washed and then dried at 50 °C. This powder was labelled as mZnO.

Method C: The third type of powder was produced by adding a NaOH solution (10 M) to an ethanolic solution of $ZnCl_2$. This etanolic solution was obtained by adding ethanol and NaOH to the stock solution (43%$_{(v/v)}$ ethanol); the final pH of the resulting solution was ~12. The addition rate of NaOH solution to the ethanolic solution of $ZnCl_2$ was the same as in (i) and (ii). The obtained precipitated powder was centrifuged, washed and then dried 50 °C. This powder is named as rZnO.

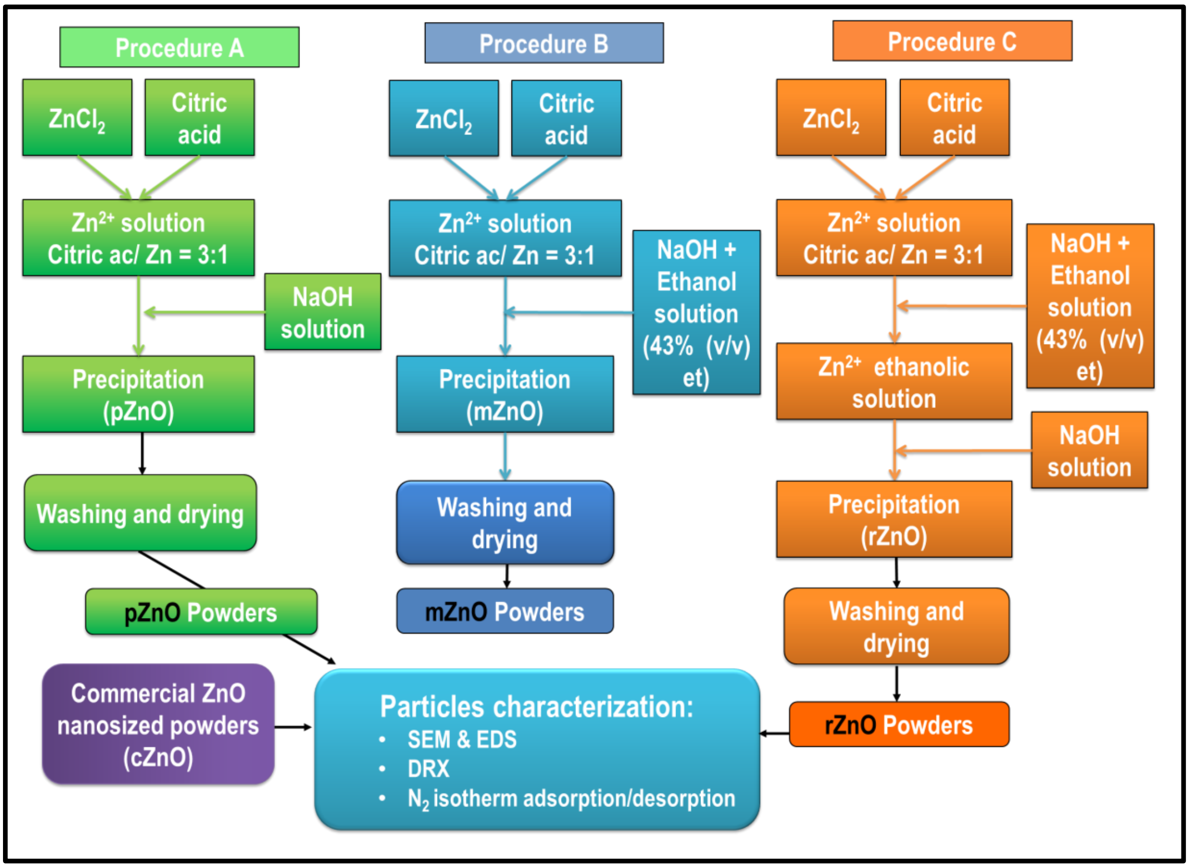

Figure 8. ZnO powders chemical precipitation procedures – pZnO, mZnO and rZnO.

Table 6 summarizes the reagent combinations the different powders (pZnO, mZnO and rZnO).

Table 6. Precipitation conditions for the different ZnO powders.

	Powders		
Materials	**pZno**	**mZnO**	**rZnO**
[Zn^{2+}] on stock solution (mmol/ml)	1.89	1.89	1.89
[CIT] : [Zn^{2+}] (mol/mol)	3:1	3:1	3:1
NaOH : ethanol $\%_{(v/v)}$	no	43*	43
NaOH (M)	10*	-	10*
Zn/Na ratio	0.3	0.3	0.3

* precipitation

All powders were observed by SEM on a SU-70 Hitachi SEM. Crystalline phase and crystallite size were accessed by XRD on a rigaku geiguflex diffractometer in a 10° < 2ϴ < 80° range, speed 3°/minute and a step of 0.02°. Crystallite size of the powders were determined for 2ϴ=46.5°, a coinciding peak of the ZnO powder and the diffractometer internal pattern, with a $\beta_{pattern}= 2 \cdot 10^{-3}$rad and form factor of 0.9. Elemental phase composition was confirmed by EDS equipment coupled with the electron microscope. Specific surface area, pore size and pore size distribution were determined by N_2 isotherm analysis obtained with a micromeritics datamaster equipment with a purge temperature 200 °C and saturation pressure of 102 kPa.

B. PU/ZnO composite films production and characterization

All the composites (0, 2 and 50 $\%_{wt}$ ZnO) samples were prepared by a solvent evaporation method using an adaptation of the J. T. Seil and T. J. Webster procedure (figure 9) [5]. To produce pure tecoflex SG80A films, the polyurethane pellets were dissolved in chloroform (2.47$\%_{wt}$ PU) till complete dissolution and casted on a 10 ml glass cup. The solvent evaporation occurred during at least 12 hours at 37 °C.

Chloroform’s mass and volume was adjusted to correspond the desired weight to either produce 2$\%_{wt}$ or 50$\%_{wt}$ ZnO composite films, maintaining the same PU/chloroform ratio. The powders used were: the commercial cZnO and the precipitated pZnO, mZnO and rZnO. The chosen powders reflect the desire to determine the influence of the different morphologies and crystallinity of the powders in the properties of the composites.

For producing $2\%_{wt}$ PU/ZnO composites 0.239 $\%_{wt}$ ZnO particles ZnO powder were mixed with 1,2-dichloroethane and sonicated during 5 minutes. The sonicated powder was mixed with the PU solution and sonicated further for 10 minutes. Solvents evaporation occurred at 37 °C overnight. The composites (98:2 $\%_{wt}$ PU/ZnO) were nominated as C2, P2 or R2 according to the used ZnO powder label, i.e. cZnO, pZnO and rZnO, respectively.

The $50\%_{wt}$ ZnO composites were obtained following the same procedure, adjusting the mass/volume of PU solution and maintaining the same PU/chloroform ratio. Roughly the ZnO powder was mixed with 1,2-dichoroethane (5,65 $\%_{wt}$ ZnO) and sonicated during 5 minutes, followed by mixture with PU solution and sonicated during 10 minutes. The solvents evaporation occurred overnight at 37 °C, and the resulting films (50:50 $\%_{wt}$ PU/ZnO) were nominated C50, P50 or R50 according to ZnO nomenclature, cZnO, pZnO and rZnO, respectively.

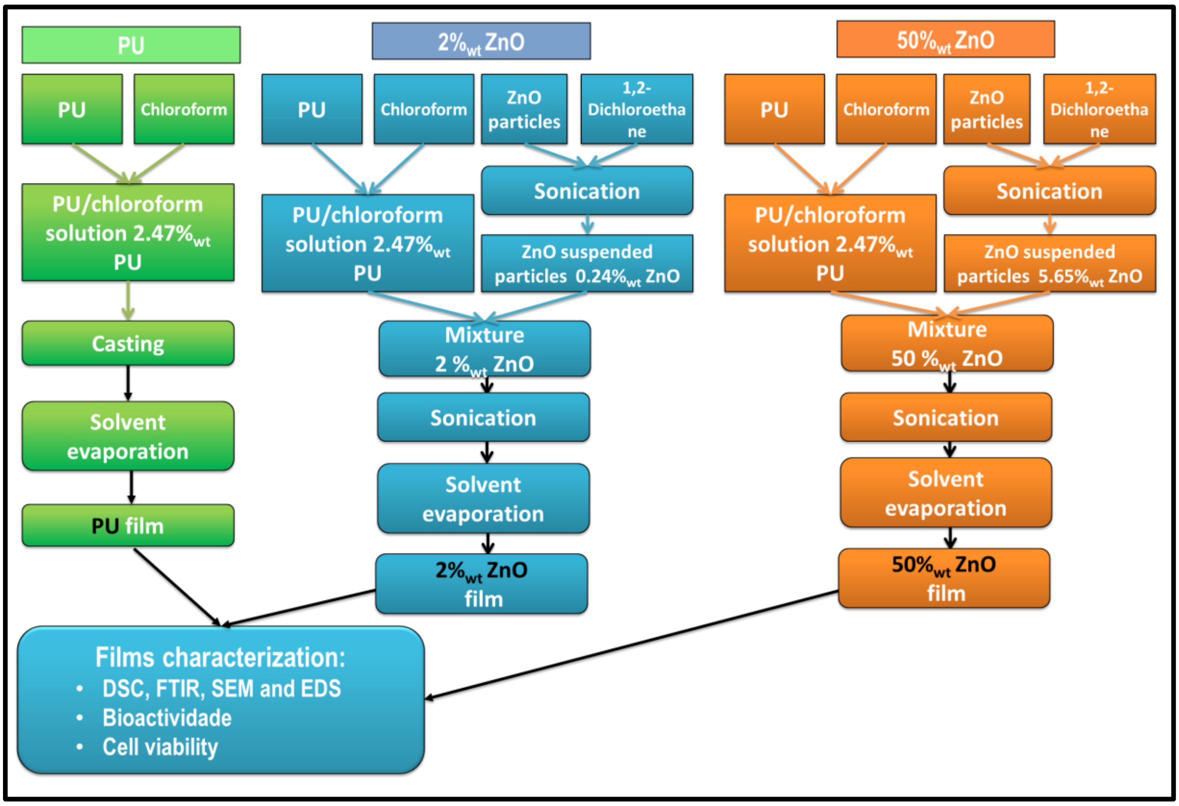

Figure 9. Polyurethane and PU/ZnO composites production procedures.

The polyurethane and composites films were 250 µm thick shaped disks (diameter 20 mm). The PU film was completely transparent and its opacity increased with increasing ZnO particles concentration, in such a way that with 50 $\%_{wt}$ the films were completely opaque.

The composites preparation is summarized in table 7.

Table 7. PU/ZnO composites preparation: reagents and composite nomenclature.

Designation	Powder	Composite		Solutions	
		ZnO [$\%_{wt}$]	PU [$\%_{wt}$]	ZnO : 1,2-D* [$\%_{wt}$]	PU : C** [$\%_{wt}$]
PU	0	0	100	0	2.47
C2	cZnO	2	98	0.24	2.47
P2	pZnO/mZnO	2	98	0.24	2.47
R2	rZnO	2	98	0.24	2.47
C50	cZnO	50	50	5.65	2.47
P50	pZnO/mZnO	50	50	5.65	2.47
R50	rZnO	50	50	5.65	2.47

*1,2-Dichloroethane
**Chloroform

All the films were characterized by SEM using a SU-70 Hitachi equipment and the films elemental composition was determined by EDS. Chemical groups were accessed by ATR-FTIR in a shimadzu IRPrestige-21 fourier transform infrared spectrophotometer with ATR coupled equipment, scanning the wavelengths range of 600 to 4000 cm^{-1} with a resolution of 4 cm^{-1} (at least 10 counts/sample). DSC analysis was performed on pure PU films and P2 and P50 composites on a shimadzu dsc-60 differential scanning calorimeter, from -80 to 200 °C and at a heating speed of 25 °C/min. Polyurethane samples were tested as casted and dried at 70 °C, while P2 and P50 composites were tested only after drying and at least two runs were made by sample.

C. Composites *In vitro* assays

C1. Bioactivity assay

The bioactivity assay was carried out following T. Kokubo, et al procedures and recommendations [47]. Briefly 10 samples of pure PU, 2%wt and 50%wt composites films were deposited in 30 ml flasks. After sterilization with UV light the flasks were filled with corrected synthetic body fluid (SBF) and sterilized again. The samples were incubated at 37 °C and collected after 1, 3, 7, 14 and 21 days of soaking (two samples each). All the samples were observed by SEM and characterized by EDS. The remaining SBF solutions of 1, 7 and 21 days of immersion were analysed by ICP on a Jobin-Yvon JY70 plus equipment for accessing their Ca, P and Zn ion contents. The results displayed as the mean ± standard deviation.

C2. Cell viability

The resazurin metabolic assay (resazuin reduction to fluorescent resorufin) was employed to determine cytotoxicity and biocompatinility of the produced nanocomposites to MC3T3 pre-osteoblastic cell line following S. Pina, et al [48] procedure at 50% cell confluence. The test was conducted with $2\%_{wt}$ C2 and P2 composites, $50\%_{wt}$ C50, P50, R50 as casted and $R50_{21}$ (SBF 21 days) and the controls used were cells incubated in a well, pure PU film and cZnO and pZnO powders, after UV light sterilization. All experiments were conducted in triplicate (except R50 samples that were only one) and expressed as the mean ± standard error. The essay was carried by covering 24 well plates with the polymer/composite samples and 50 mg of either one of the ZnO powders. $1\text{x}10^5$ cells were prior deposited in each well (cell density was $1\text{x}10^4$ cells/cm^2) and cultured in cell medium. The cell medium contained 2mM glutamine (with minimum essential α-medium in Eagle's balanced salt solution supplemented with 10% (v/v) foetal bovine serum), 1% (v/v) of U mg/ml penicillin, 100 mg/ml streptomycin solution (Gibco BRL, Invitrogen) and 3.7 g/l $NaHCO_3$. Cell culture occurred at 37 °C in humified atmosphere with 5% CO_2. The resazurin assay was carried by replacing the growth medium with fresh medium containing 10% resazurin (Sigma Aldrich) in phosphate buffer saline (0.1 mg/ml - Pierce, Perbio). After 4 hours of incubation the medium was collected and cell viability was evaluated by detecting resazurin reduction at 570 and 600 nm with a varian cary 50 BIO spectrometer.

2.2. Techniques description

A. X-ray diffraction – XRD

The X-ray diffraction is a powerful technique that allows the identification of the crystalline phases of a crystalline material. This technique s is based on the constructive phenomenon of diffracted radiation by verifying the Bragg law [49, 50]:

$$\boldsymbol{n\lambda = 2d_{hkl}\ \sin\theta} \qquad \text{(equation 2)}$$

Where '$n\lambda$' is the constructive phase difference, 'd_{hkl}' is distance between two parallel planes and 'θ' the reflection angle between a crystallographic plane and the incident radiation with content wavelength 'λ' [49]:

For each of hkl planes present in the material a characteristic peak appears in the difractogram that can be identified by comparison with datasheets of well identified materials [49].

The crystallite size 'D' may be estimated from a difractogram by following the *Debye-Scherrer* equation [51]:

$$\boldsymbol{D = \frac{K\lambda}{\beta\cos\theta}} \qquad \text{(equation 3)}$$

Where 'K' is a form factor (0.89 to spherical surfaces), 'λ' the X-ray wavelength (typically 1,54056 $\dot{A}$), 'β' the width at half height of the peak (in radians) at 'θ' degrees (radians) were the diffraction occurred.

'β' can be established by relating the half height of the sample and pattern, 'β_{sample}' and 'β_{patern}' respectively, for the same diffraction angle following the equation:

$$\boldsymbol{\beta^2 = {\beta_{sample}}^2 - {\beta_{patern}}^2} \qquad \text{(equation 4)}$$

B. N_2 Isotherm analysis

Isotherm is the relation at constant temperature of the gas quantity adsorbed at the surface of a material and the partial pressure at which it occurs. According to Braunauer, Emmet and Teller (BET), four basic steps can describe the gas adsorption on a material surface (figure 10) [52- 54].

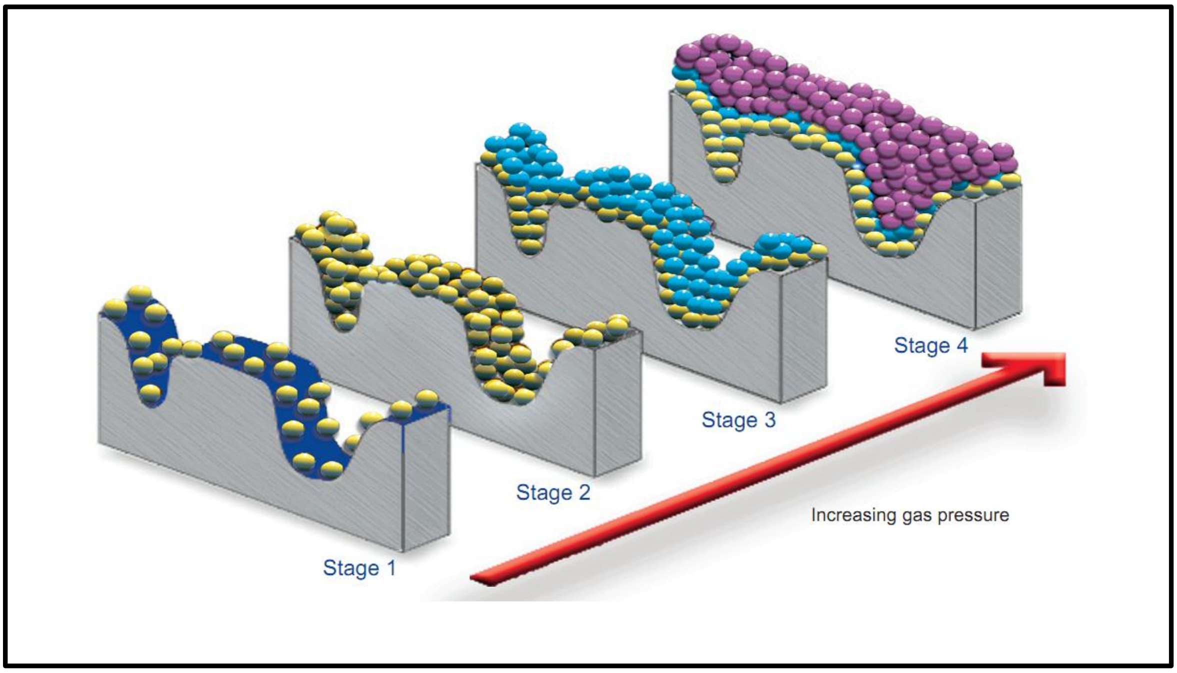

Figure 10. Four steps in BET gas adsorption theory: initial adsorption process, monolayer formation, multilayer formation and pores filling [54].

On the first stage (1) the gas molecules adsorb at material surface through Van der Waals forces. With the raise of pressure more gas molecules adsorb till a complete monolayer is formed (stage 2) and with further pressure increase new gas adsorbed layers are formed (stage 3 and 4). This simplistic model can't fully describe isotherms other than the International Union of Pure and Applied Chemistry (IUPAC) type II isotherms, as other phenomena, such as capillary condensation within mesopores, may give rise to other behaviours and consequentially to other isotherms [52].

Capillary condensation is a phenomenon that occurs after the multilayer formation in which the gas further adsorbed condenses in the remaining pore volume. The liquid phase formed is separated by gaseous phase through a meniscus [52].

The IUPAC defines a pore as a cavity in which its depth is larger than its length. According to IUPAC pores are classified in function of the diameter ‘D_p’ [52]:

- Macropores: $D_p > 50$ nm
- Mesopores: $0.2 < D_p < 50$ nm
- Micropores: $D_p < 0.2$ nm

IUPAC predicts six isotherm patterns, i.e. type I to type VI isotherms as illustrated in figure 11:

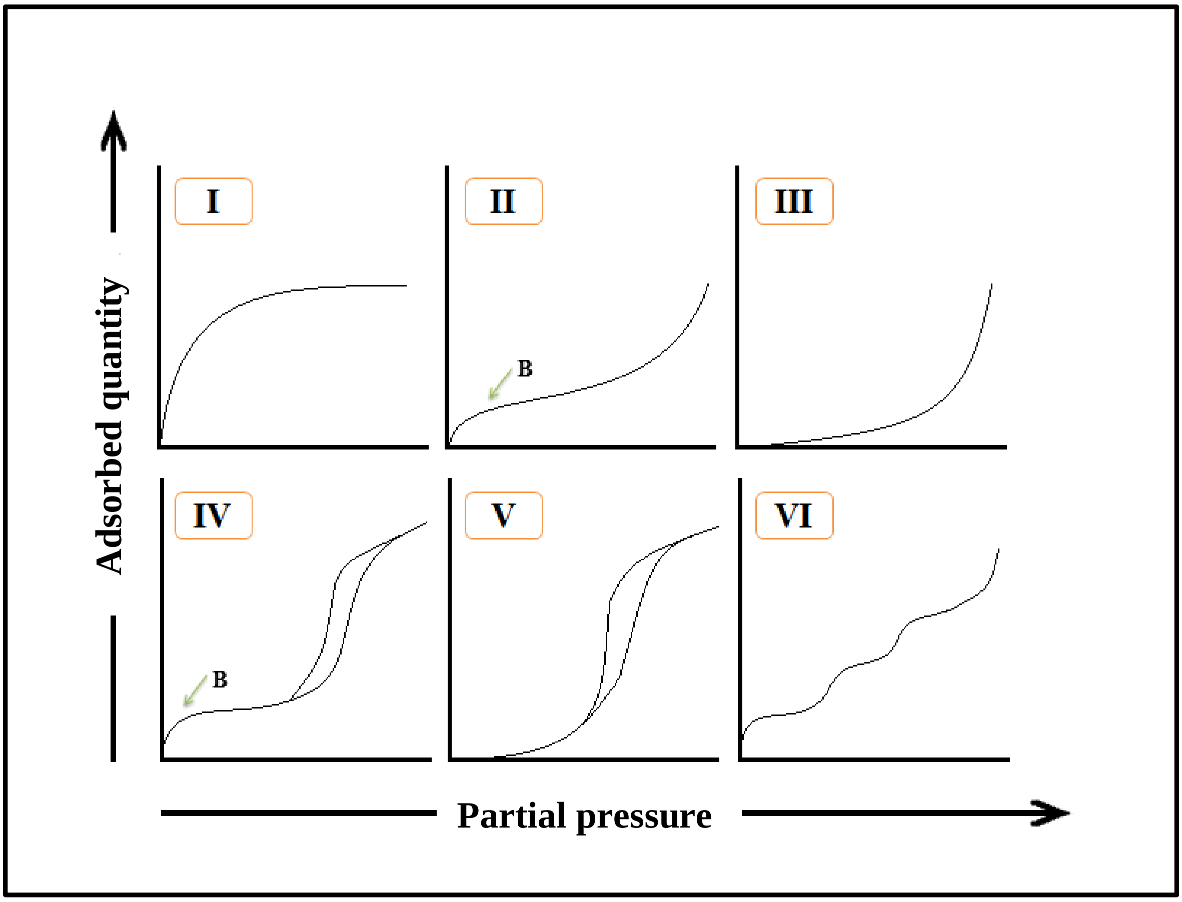

Figure 11. IUPAC isotherms patterns on porous solids or powders [52].

- Type I: This isotherm is also known as *Langmuir* isotherm. This behaviour is found in microporous solids with low external surface area (activated carbon or zeolites). As the curve rises with increasing partial pressure it reaches a *plateau* near the end limited by micropore volume.

- Type II: This isotherm is rather common to nonporous or macroporous solids and is associated to a monolayer formation (point B) and multilayer adsorption without restriction.

- Type III: Type III isotherms are rare cases and generally do not have the B point. Some cases however present an undefined B point and in those cases the interactions adsorbate-adsorbate are more relevant than the adsorbate-adsorbent.

- Type IV: Like type II this isotherm is characterized by multilayer formation and has a hysteresis loop cycle resulting from capillary condensation within mesopores.

- Type V: Type V isotherm is also characterized by a hysteresis loop cycle, but instead of a multilayer formation it follows type III tendency in which the interaction of adsorbate-adsorbent are rather weak.

- Type VI: This isotherm generally represents a step multilayer adsorption on nonporous uniform surfaces and each step is related to one layer formed.

Isotherms IV and V hysteresis loops can exhibit four different patterns (H1 to H4 – see figure 12) normally associated to capillary condensation in mesopores with different geometry [52]:

- Type H1: Related to agglomerates of spherical particles with narrow pore size distributions.

- Type H2: Extremely difficult to interpret; network pore connectivity effects must be considered as the ink bottle pore shape approach as proven to be too simplistic

- Type H3: This loop pattern is exhibited by platelet aggregates with slit shaped pores.

- Type H4: As in type H3, platelet aggregates may give rise to this pattern when slit pores are very narrow.

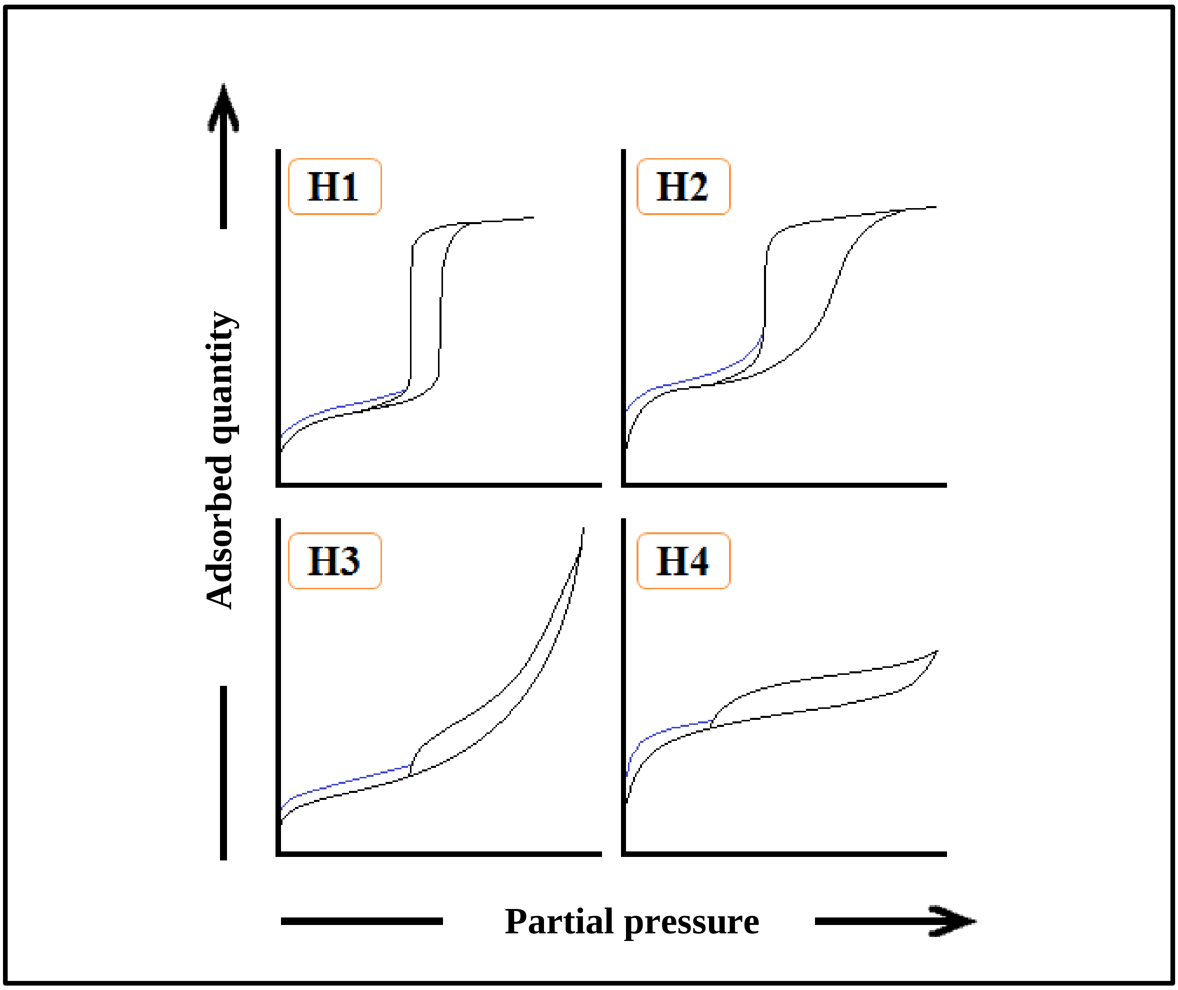

Figure 12. Classification of hysteretic IUPAC isotherms (type IV and V) [52].

B1. BET specific surface area

According to Braunauer, Emmet and Teller (BET) methodology, the specific surface area (SSA) may be determined from the linear part of the adsorption isotherm in the partial pressure range 0.05 to 0.30 through the BET equation (equation 5) [53]:

$$\frac{\frac{p}{p^o}}{n(1-\frac{p}{p^o})} = \frac{Y-1}{n_m Y} \cdot \frac{p}{p^o} + \frac{1}{n_m Y} \qquad \text{(equation 5)}$$

In which '$\frac{p}{p^o}$' is the gas partial pressure, 'n' is the amount of adsorbed gas, 'n_m' the monolayer capacity and 'Y' is a constant related to the energy of monolayer formation é [53].

After the determination of 'n_m' from the BET equation the SSA may be calculated by the equation:

$$SSA = \frac{n_m \cdot N_A \cdot a_m}{m} \qquad \text{(equation 6)}$$

In which 'm' is the sample mass, 'N_A' is the *Avogadro* constant and 'a_m' is the area occupied by one molecule of adsorbate in the complete monolayer. Considering that the adsorbed N_2 gas gives rise to a compact monolayer formation 'a_m' equals 0,162 nm^2 [53].

To be noted that in type II and IV isotherms associated to large mesopores the BET equation linearity is verified between $0.05 < \frac{p}{p^o} < 0.35$. However for rather small mesopores the linearity is verified at lower partial pressures, $0.05 < \frac{p}{p^o} < 0.20$, and SSA is generally overestimated [55].

It is possible to determine the sphere equivalent particle size 'SED' from the SSA determined from the BET procedure [51]:

$$SED = \frac{6}{SSA \cdot \rho} \qquad \text{(equation 7)}$$

Were 'ρ' is the theoretical density and 'SSA' the specific surface area determined by BET procedure.

B2. BJH pore volume and area distribution

The isotherm desorption branch is used to correlate the quantity of lost gas to the pore average size for the case of the pores being emptied during each step of desorption. A pore loses its condensed liquid at a particular relative pressure that is related to the kelvin radius '$\boldsymbol{r_K}$' [52, 55], according to Kelvin equation:

$$\boldsymbol{r_K = \frac{2\cdot\sigma^{1g}\cdot\vartheta^{1}}{RT\ln\left(\frac{p}{p^o}\right)}} \qquad \text{(equation 8)}$$

Were 'r_K' is the Kelvin radius, '$\frac{p}{p^o}$' partial pressure were the condensation occurs, 'σ^{1g}' is the condensed surface energy, 'ϑ^{1}' is the condensed molar volume, 'R' is the gas constant and 'T' the temperature. An adsorbate layer is then left behind whose thickness '$\boldsymbol{t}$' is determined by Halsey equation [52, 55]

$$\boldsymbol{t = 3,54\left[\frac{-5}{\frac{p}{p^o}}\right]^{0,333}} \qquad \text{(equation 9)}$$

The adsorbate layer becomes thinner upon the partial pressure decrease. The total amount of desorbed gas '$\boldsymbol{r_p}$' at a given pressure is equal to the amount of the lost condensed liquid '$\boldsymbol{r_k}$' plus the amount of the evaporated gas from the pores previously emptied '$\boldsymbol{t}$' [47, 49], i.e.:

$$\boldsymbol{r_p = r_k + t} \qquad \text{(equation 10)}$$

Taking this into account it is possible to analyse type IV and V isotherms and determine the specific pore volume, the porosity, the pore size distribution and the average pore size [55].

Following Barret, Joyner, Halenda (BJH) procedure the following assumptions regarding pore morphology have to be kept in mind [55]

- The pores are regularly shaped and rigid
- That micropores are negligible
- The pore size distribution doesn’t continuously extend from meso range to macro range

The average pore size ‘$\boldsymbol{d_{AV}}$’ can be then determined by [55]:

$$\boldsymbol{d_{AV}} = \frac{\boldsymbol{4 \cdot V_p}}{\boldsymbol{S}} \qquad \text{(equation 11)}$$

Were ‘V_p’ is the total volume of pores and ‘S’ is the pore cumulative surface area.

C. Scanning electron microscopy – SEM

The scanning electron microscopy is an observation technique that with its high spatial and focus depth, nanometre range resolution and a heavy magnification capacity enables the observation the morphology and topography of a material’s surface [50, 49].

The basic work principle lies in the bombardment of a materials surface with an electron beam from which results the emission of electrons or photons from the surface that after being detected and conveniently treated give life to the surface image topography [50].

Samples for SEM can have any form but the sample setup should have the minimum operation to preserve surface characteristics. Normally a conductive thin coat is sputtered on the materials surface to ensure conductivity. Thicker coatings may lead to undesired artefacts crystallization or rupture and distortion of the original surface [49].

From the many interactions of the materials surface and the electron beam, the decay of excited electrons from high energy levels with liberation of characteristic X-rays may occur. If the intensity of this X-ray is detected and plotted against the energy it is possible to identify the element that is the origin of the X-ray, as each element releases its own specific X-ray that carries a specific energy. This is the basics of energy dispersive spectroscopy (EDS) that is normally coupled with SEM systems and allows the analysis of elements in a material [49].

D. Differential scanning calorimetry - DSC

The differential scanning calorimetry (DSC) is used for the determination of the thermal events (exo/endothermic) that occur on materials when heated or cooled. These events may be phase transformations, glass transitions, crystallizations or melting and the method is based on the comparison of the material behaviour with that of a reference material which is not subjected to changes at those temperatures. Therefore in a typical polymer DSC curve it is possible to observe the endothermic changes (glass transition, melt and degradation) and the exothermic reactions (crystallization and oxidation) [49].

E. Attenuated total reflectance Fourrier transform infrared spectroscopy: ATR-FTIR

Fourier Transform InfraRed (FTIR) is a spectroscopic method used to gain information about the chemical bonding in a material, and so it is very useful to study a chemical bond of interest rather than being a generic probe. This technique studies the changes of intensity of an IR beam as a function of its wavelength (200 to 4000 cm^{-1}) when it interacts with the sample, and each intensity peak can be related to a specific known chemical bond. If a sample is opaque the use of attenuated total reflection (ATR) crystal may be employed, and thus exploit the reflection of the beam as it propagates throughout the sample and crystal enhancing the signal [50].

F. Bioactivity assay

It is generally accepted that the formation of bonelike apatite on the surface of a material is a requirement to improve the bone bonding capability of the material, as long as it does not induce cytotoxicity to the cells. Kokubo et al [47] found that this *in vivo* behaviour can be reproduced and predicted *in vitro* with simulated body fluid (SBF) with ion concentration near to that of human blood plasma (HBP). The SBF assay is relatively accurate in defining the bioactivity (bone bonding capability) of a material. In some cases no apatite materials can bond to human bone and in others apatite materials do not do so. The reason this occurs is manly related to antibody foreign reaction that prevents the bonding [47].

Because the original SBF solution (table 8) did not contain the correct amount of SO_4^{2+}, a modified SBF solution was proposed to obviate this problem. The modified SBF Cl^- and HCO_3^- ion content differ from those in HBP, the stability and reproducibility of the results is no different from the new formulations that more accurately reproduce HBP. It should be mentioned that modified SBF it's easier to prepare that the new formulations [47].

Table 8. Human body fluid (HBP) and simulated body fluid (SBF) ion concentrations, [47].

	Na^+ [mM]	K^+ [mM]	Mg^{2+} [mM]	Ca^{2+} [mM]	Cl^- [mM]	HCO^{3-} [mM]	HPO_4^{2-} [mM]	SO_4^{2-} [mM]
HBP	142.0	5.0	1.5	2.5	103.0	27.0	1.0	0.5
Original SBF	142.0	5.0	1.5	2.5	148.8	4.2	1.0	0.0
Corrected SBF	142.0	5.0	1.5	2.5	147.8	4.2	1.0	0.5

G. Resazurin cell viability assay

The resazurin cell viability assay is a rapid quantitative method to determine the growth state of living cells. It is a reversible nontoxic method that lies on the conversion of the non-fluorescent dye resazurin (7-hydroxy-3H-phenoxazin-3-one-10-oxide) to the highly fluorescent resorufin (7-hydroxyphenoxazin-3-one). This change occurs as a response due to cell growth. The medium maintains a reduced state when cells are growing and an oxidized one if growth is inhibited, so the redox indicator changes from the oxidized purple colour resazurin to the reduced state pink resorufin when the environment is reduced by cell growth. The colorimetric signal is proportional to the number of living cells in the sample. It should be noted that resorufin can be converted in hydroresorufin, which is colourless and non-fluorescent, and that causes the signal to decrease even with cell growth. Final resazurin value 'ODF' is determined as the ratio of the absorbance detected at 570 nm 'OD_{570}' and the intensity at 600 nm 'OD_{600}' minus 1 [48, 56].

$$\boldsymbol{ODF = \frac{OD_{570}}{OD_{600}} - 1} \qquad \text{(equation 12)}$$

For the controls ODF is taken as 100% and the samples media ODFs are converted as percentage of this value.

Chapter III

3. Results and discussion

3.1. Zinc oxide particles

A. Crystal phase composition, shape and particle size

The XRD patterns of all the particles synthesized by chemical precipitation method (pZnO, rZnO, mZnO) as well as that of the commercial ZnO powder (cZnO) confirm that a single Wurtzite hexagonal phase (JPCDS 00-036-1451) is obtained (figure 13).

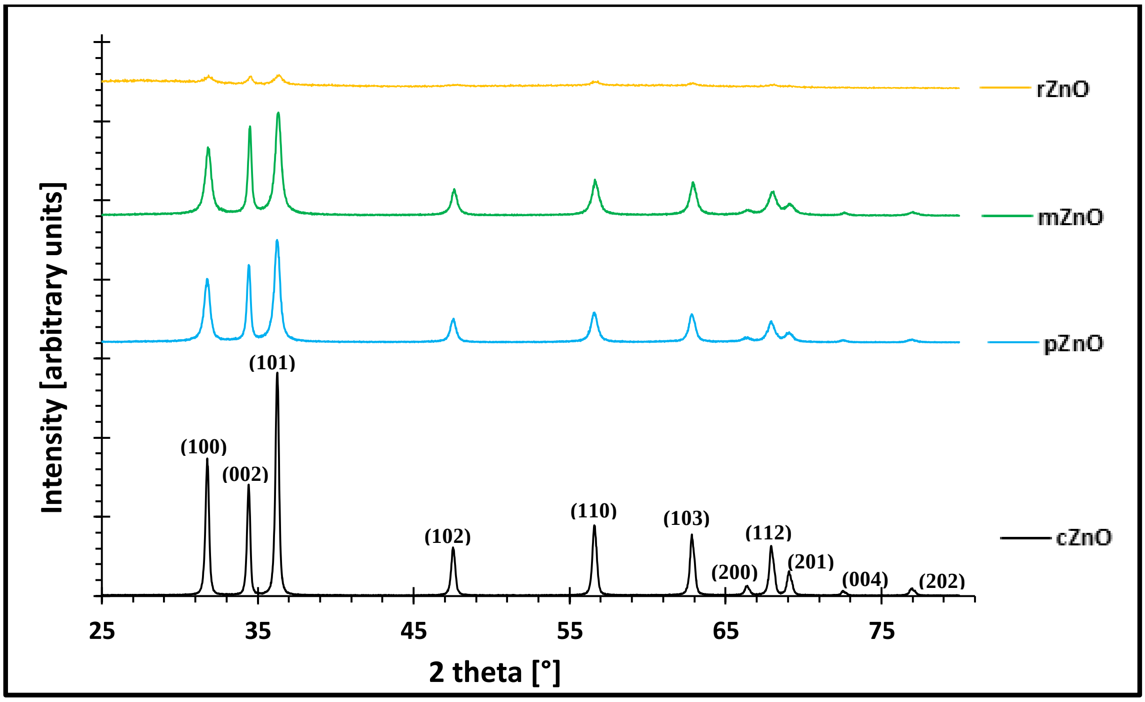

Figure 13. XRD patterns of the commercial (cZnO) and precipitated ZnO particles (pZnO, mZnO and rZnO).

The cZnO powder appears to have higher crystallinity than the precipitated powders, probably reflecting a high temperature processing. The rZnO shows incipient crystallisation, as its peaks intensity is lower than those of the remaining powders. pZnO and mZnO developed a well-defined crystal structure reflected by their sharp and intense XRD peaks.

The average crystallite sizes of cZnO, pZnO and mZnO powders, determined by Debye-Scherrer equation, were 67, 46 and 56 nm respectively. It was not possible to determine accurately the crystallite size of rZnO powder due to its poorly defined XRD pattern.

The purity of all the ZnO powders was further confirmed by EDS spectra (figure 14) which revealed that the elements present in the samples are uniquely Zinc and Oxygen. The detected aluminium and carbon are attributed to the used aluminium sample holder and deposited carbon on the samples for SEM observation, respectively, indicating absence of powder contamination.

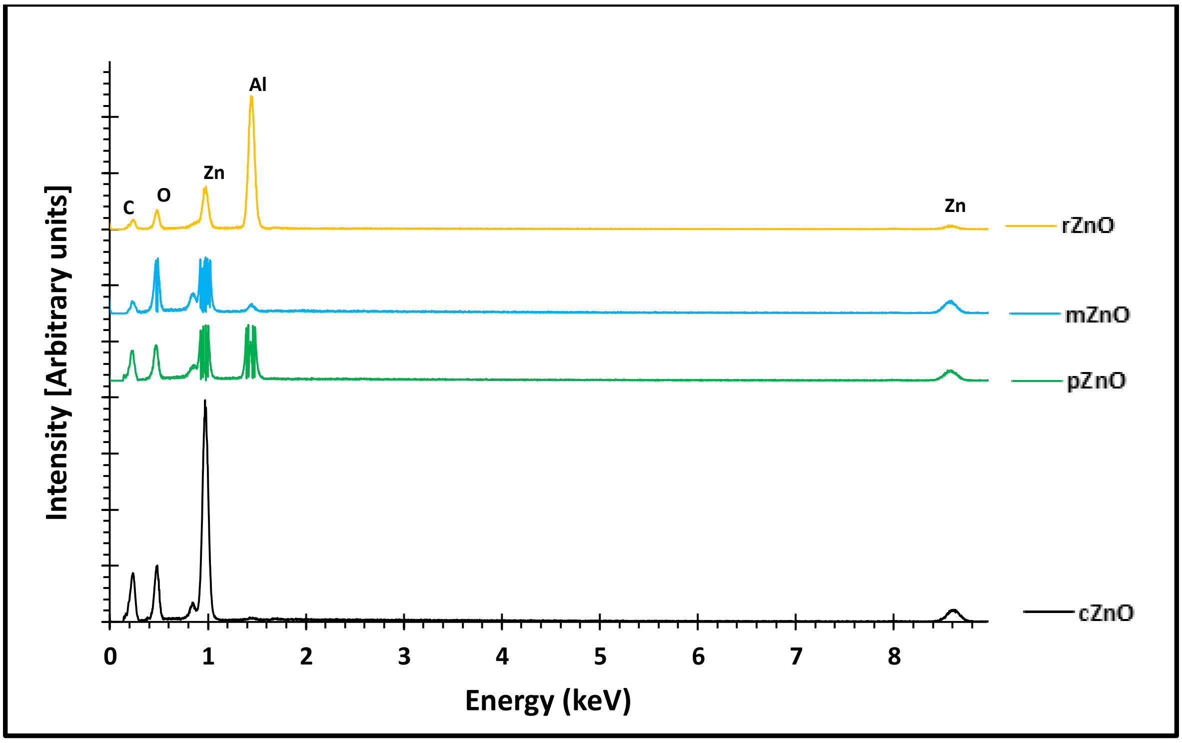

Figure 14. EDS analysis of ZnO particles (cZnO, pZnO, mZnO and rZnO).

SEM observation of the commercial powders (figure 15) reveals a mixture of large aggregates of merged ZnO nanosized spherical, platelet and nanosized particles. This powder appears to be extremely uneven regarding particle size, size distribution and morphology. This feature probably reflects its industrial processing mode that is based on high temperature treatments of either Zn metal or ore. The high cristalinity and crystalite size of the powder previously commented are in line with this reasoning.

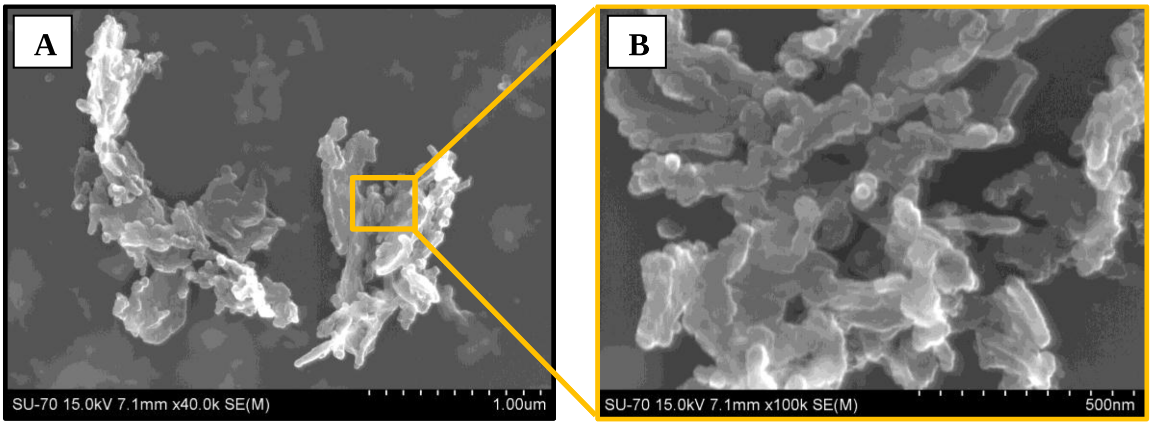

Figure 15. A) and B): SEM images of the commercial ZnO powder particles at different magnifications.

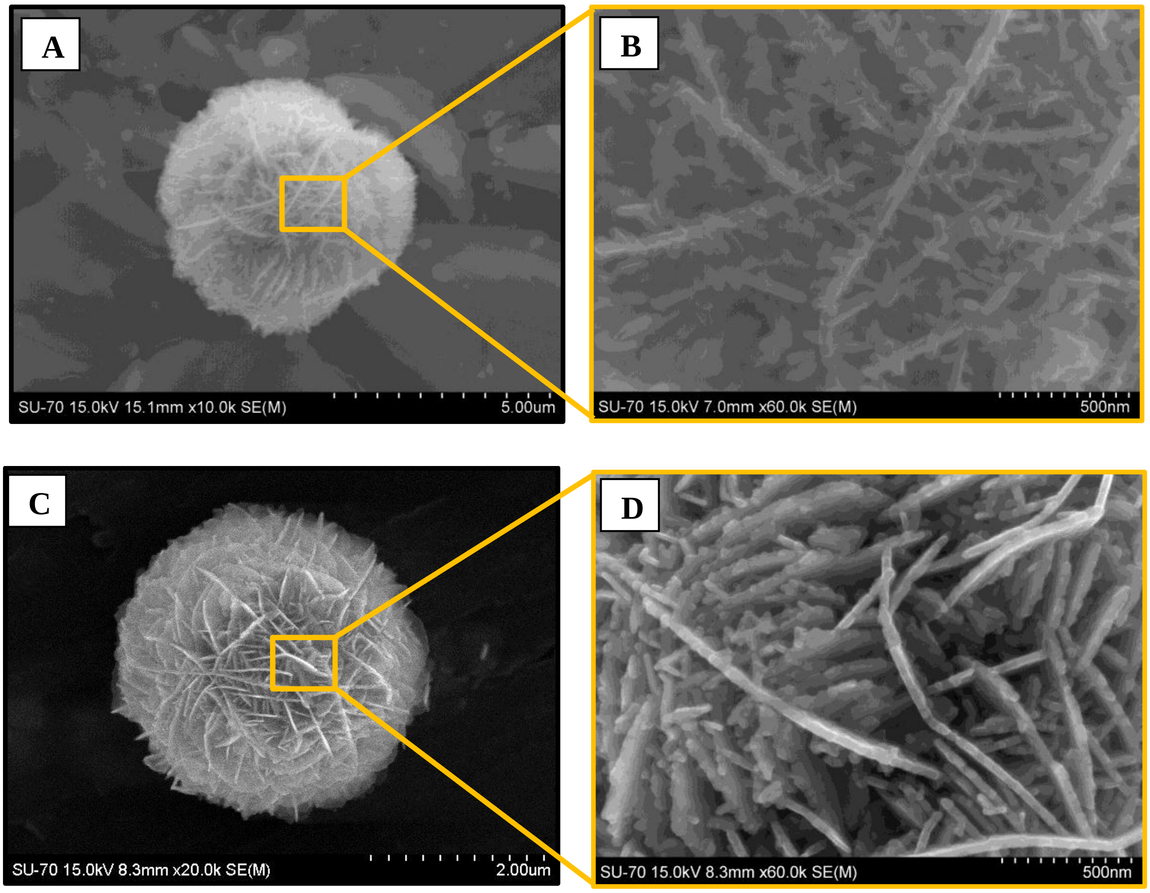

Figure 16. SEM images of precipitated ZnO particles: A) and B) pZnO at different magnifications; C) and D) mZnO at different magnifications.

The electronic images of pZnO (figure 16 A and B) and mZnO (figure 16 C and D) powders reveal complex structures which appear as spherical assemblages of nanometric sized platelets or fine dendrites with an average thickness of about 50 nm. Regarding rZnO particles (figure 17), they present themselves with morphology rather different as compared to the other powder particles: rZnO particles are nanometric sized spheres with an average diameter of about 100 nm. The average crystallite sizes stated above are in according to the corresponding SEM images, as the thicker structures have a larger crystallite size.

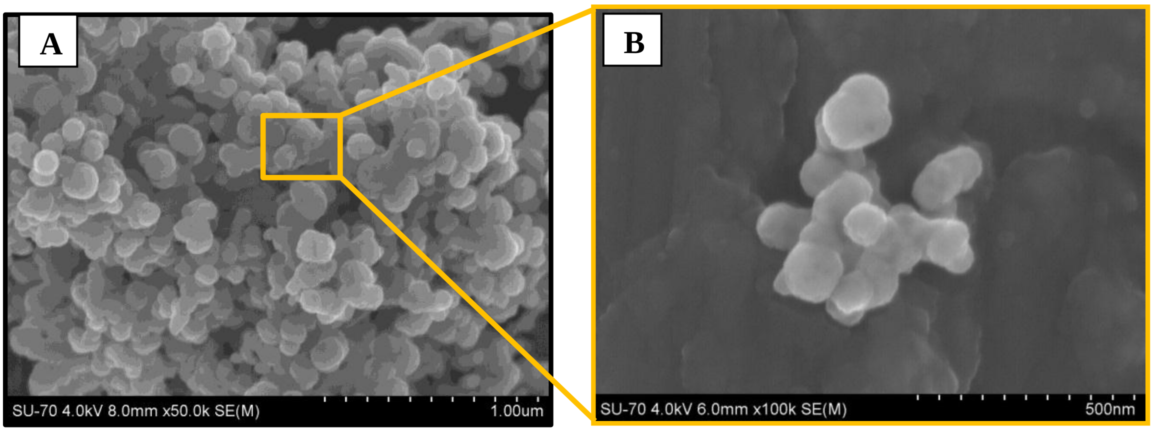

Figure 17. A) and B): SEM images of precipitated rZnO powder particles at different magnifications.

The morphology differences exhibited by the precipitated particles reflect the differences among their synthesis conditions. In the case of rZnO particles, the used ethanol was added to Zn^{2+} solution prior to the start of precipitation. Ethanol thus could act not only as surfactant but also as a modifier of the precipitation medium chemical composition. It is here suggested that ethanol might have decrease ZnO solubility in the ethanolic precipitation medium thus contributing to enhance supersaturation and thereby favour the ZnO nucleation rate. Favouring the nucleation rate, ethanol would contribute to the genesis of a large number of nuclei which would grow to a less extent as compared to the smaller number of nuclei formed in the other different conditions which would be allowed to grow more. In the case of mZnO powders which also grow in etaholic medium, nucleation was differently affected by ethanol as ethanol was added during precipitation, thus implying a low concentration of ethanol at the early stage of nucleation.

These results thus suggest that ethanol concentration in the precipiating medium is a critical condition impacting strongly the nucleation rate of ZnO particles. Similar effects on ZnO nucleation were already reported for etanolic medium where nanometric sized ZnO particles were precipitated [57].

B. Porosity and specific surface area

The isotherm adsorption/desorption branches and the corresponding pore size distributions (insets) respecting cZnO, pZnO, mZnO and rZnO are represented in figure 18, 19, 20 and 21 respectively.

cZnO isotherm (figure 18) is very close to a IUPAC type II isotherm [52] which is a characteristic isotherm of non-porous or macroporous materials. Although a pore size distribution has been determined with an average pore size of 7 nm (table 9), the pore volume is rather small as compared to pore volume of the remaining powders and thus the mesopores exist in a small amount. Micropores were not found in this material. On the other hand pZnO, mZnO and rZnO powders present type IV isotherms [52] (figures 19, 20 and 21 respectively) which are characteristic of mesoporous materials displaying mesopore capillary condensation. Furthermore both pZnO and mZnO present type H3 hysteresis loop branches which are indicative of a platelet aggregates with slit like pores [52]. This indication is in line with the powders morphology revealed by SEM, particularly in the case of mZnO which exhibits slit like pores between its nanometric sized platelets. The average pore sizes of pZnO and mZnO were determined as 14 and 12 nm respectively (table 9). Concerning rZnO nanopowder, it exhibits an H4 type hysteresis loop [52] which is normally associated to very small slit like pores; in this case the average pore size was determined as 7 nm, which is indeed a lower value than the previous ones. It is necessary to keep in mind that the BJH procedure of pore size and the pore size distribution calculation may underestimate the pore size as it assumes that all pores are cylindrical in shape.

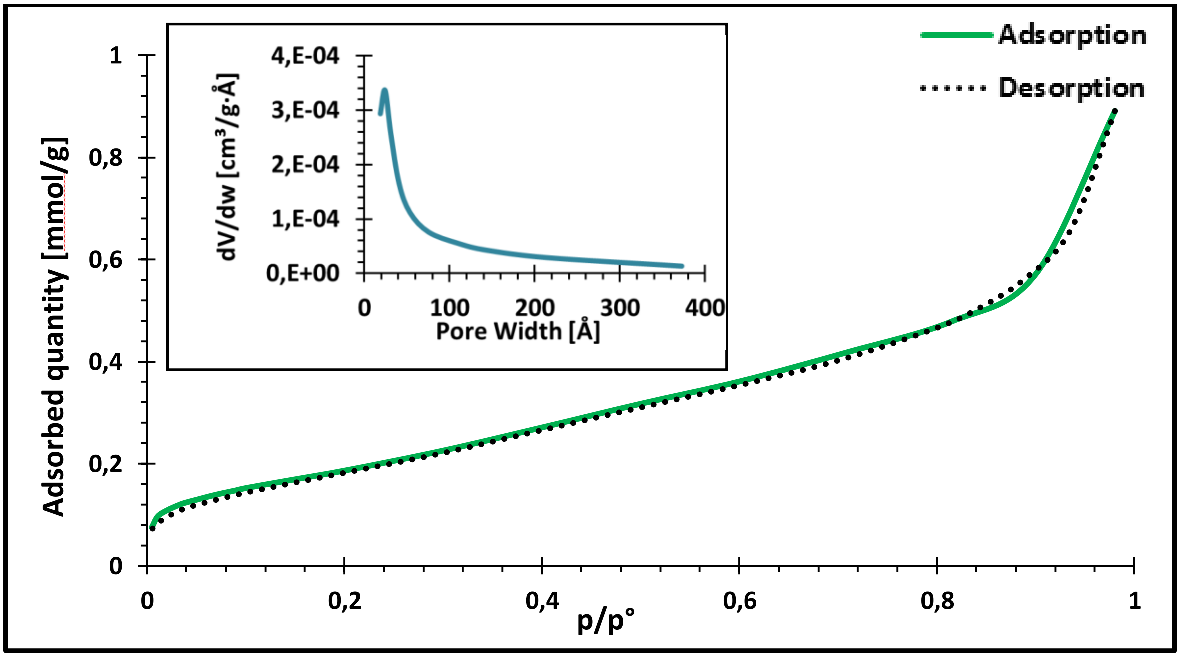

Figure 18. cZnO powder adsorption/desorption type II isotherm and pore size distribution (inset).

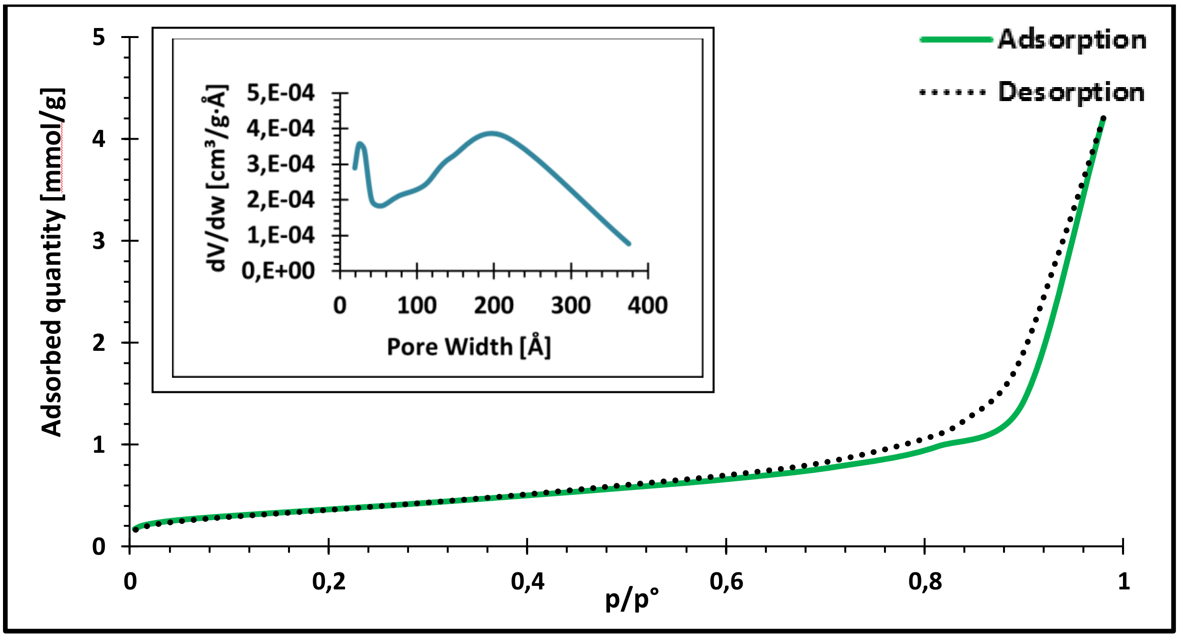

Figure 19. pZnO powder adsorption/desorption type IV isotherm, H3 hysteresis loop and pore size distribution (inset).

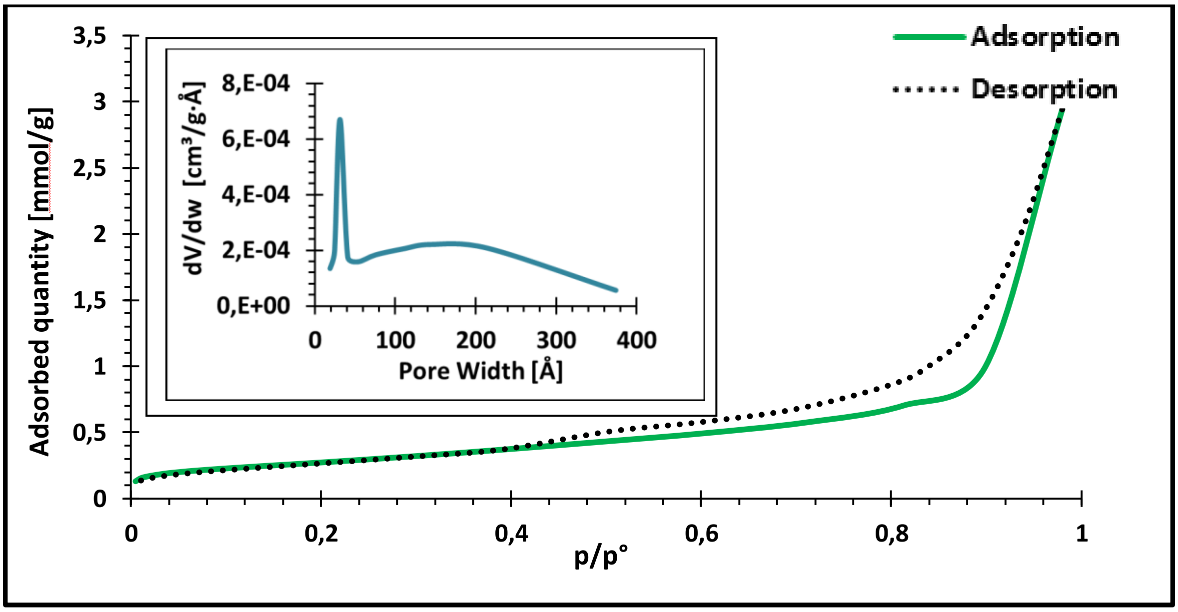

Figure 20. mZnO powder adsorption/desorption type IV isotherm, H3 hysteresis loop and pore size distribution (inset).

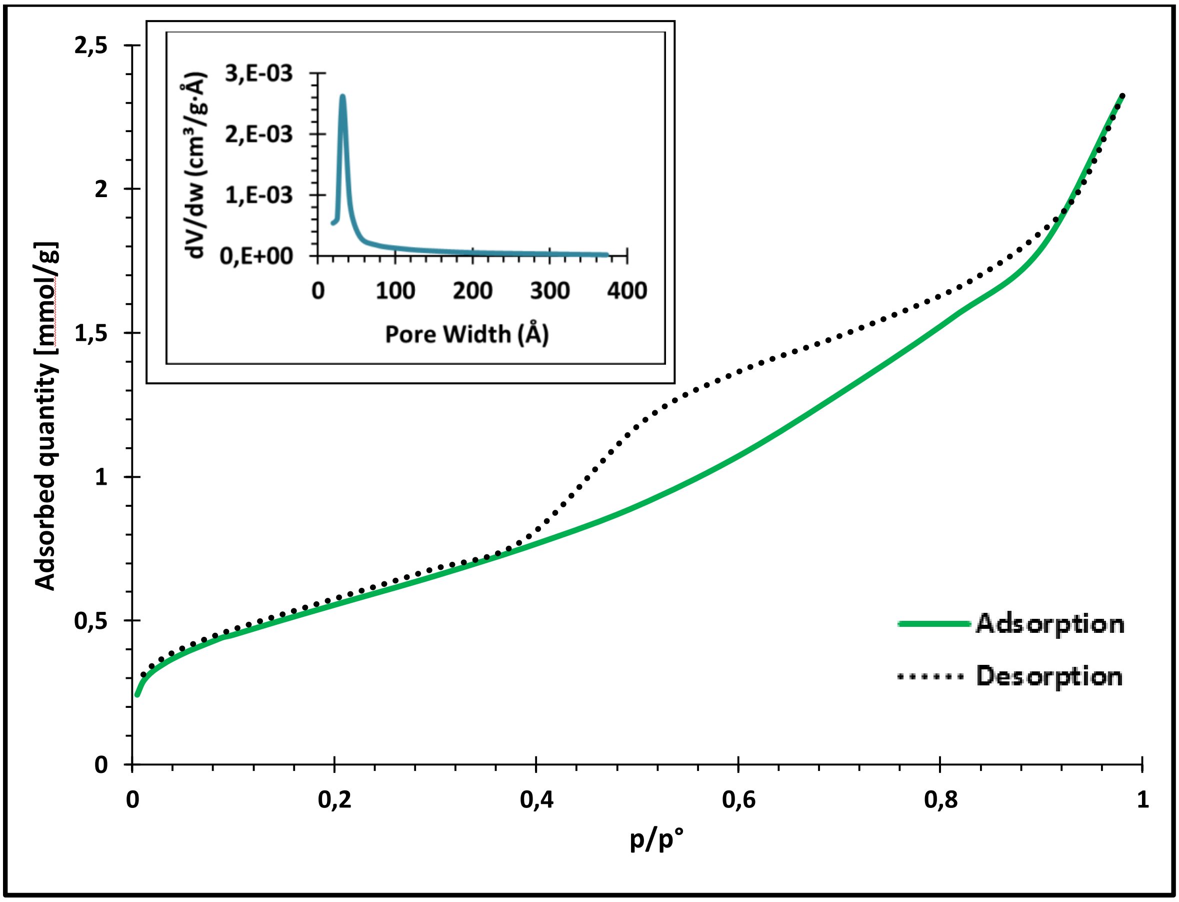

Figure 21. rZnO powder adsorption/desorption type IV isotherm, H4 hysteresis loop pore size distribution (inset).

The specific surface areas (SSA) (table 9) determined according to BET equation were 15, 29, 45 and 21 m^2/g for cZnO, pZnO, rZnO and mZnO respectively. As expected the rZnO exhibited the highest surface area because of its nanometric particle size and of its mesopore walls contribution. Contrarily cZnO being a very aggregated and almost pore devoid powder, it exhibits the lowest surface area. The surface areas of pZnO and mZnO are in a range between cZnO and rZnO values. The pZnO and mZnO powders have similar morphology and very similar SSA values as well. The main difference between these two powders is due to the thicker plate of mZnO which originate a more clustered and dense nanoflower like structure as compared to pZnO. The more open structure of pZnO also explains its larger pore volume as determined by BJH procedure. The precipitated ZnO particles have thus larger specific surface area and larger pore volume than the commercial ZnO nanoparticles.

The cumulative surface area of the powders cZnO, pZnO, rZnO and mZnO, determined by BJH procedure, are respectively 17, 41, 62 and 31 m^2/g (table 9). As these values are superior to the corresponding BET based values (15, 29, 45 and 21 m^2/g, respectively), it is indicative of the existence of bottle shaped pores that favours small diameters, for a given volume of absorbed gas, thus leading to an overestimation of the surface area [55].

Taking into account the BET surface areas and assuming the powders to be spherically shaped, the equivalent sphere diameter (ESD) was calculated as 71, 37, 24 and 51 nm for. cZnO, pZnO, rZnO and mZnO, respectively. This result means that despite their particle size exceeds 100nm which is considered to be the limit dimension for “nano” classification [8], their surface area is equivalent to that of a spherical particle under 71 nm, and as such their particle should be considered as a nanoparticle or nanostructured particle. Furthermore the fact that all the surface areas per unit of volume (m^2/cm^3) are 84, 161, 252 and 118 m^2/cm^3 for cZnO, pZnO, rZnO and mZnO respectively, staying above 60 m^2/cm^3 which is lower limit for “nano” classification [8], corroborates the adequateness of the “nano” label for the powders synthesized in the present work.

The particles characteristics are summarized in table 9 and their relevance will be addressed in the coming sections.

Table 9. Characteristics of commercial (cZnO) and precipitated ZnO particles (pZnO, mZnO and rZnO).

Powder	Phase	Crystallite	Isotherm	SSA	Cum. SSA	VSSA	AVR$_{\text{Pore sise}}$	ESD
	DRX - EDS	(nm)	type	(m^2/g)	(m^2/g)	(m^2/cm^3)	(nm)	(nm)
cZnO	ZnO	67	II	15	17	84	-	71
pZnO	ZnO	46	IV - H3	29	41	161	14	37
rZnO	ZnO	I. C.	IV - H4	45	62	252	5	24
mZnO	ZnO	56	IV - H3	21	31	118	12	51

SSA = Specific surface area
Cum. SSA = Cumulative specific surface area
VSSA = Volume specific surface area
AVR$_{\text{Pore sise}}$ = Average pore size
ESD = Equivalent sphere diameter
IC = incipient crystallization

As a final conclusion of the present sections it is worthy to emphasize that the manipulation of the chemical composition of the precipitating medium by ethanol addition allowed the control of the morphology, i.e. shape and size, of the final precipitate while maintaining its chemical composition and purity.

3.2. Polyurethane characterization

The importance of the characterization of one material is extremely important in the biomedical area. It is relevant to understand the material and its reaction with the human body as it could lead to a cascade of events with arising problems if the inserted material is not known. Therefor even if the material is FDA approved, such as tecoflex SG80A polyurethane, the evaluation of its structure and properties is still needed, as a way to predict and understand its behaviour *in vitro* and *in vivo*.

A. Attenuated total reflectance Fourrier transform infrared spectroscopy: ATR-FTIR

Figure 22 presents the ATR - FTIR spectrum of the polyurethane used in the present work, Tecoflex SG80A polyurethane. The identification of the various peaks and bands is presented in table 10 where some literature data are also presented for comparative purposes. The wavenumbers values are very close to those referred by C. Guignot, et al [58]. PU typical peaks were found at 3294 cm^{-1} (figure 22 - B) attributed to H-bounded NH stretching, at 2916, 2845 and 2783 cm^{-1} (figure 22 – C, D and E respectively) assigned to C-H stretching from both polyether and cyclohexane (table 22 for details) and at 1716 cm^{-1} ascribed to free C=O stretching (figure 22 - F). The peak corresponding to free N-H could not be identified (around 3445 cm^{-1} – table 10) in the present analysis thus indicating that practically all the NH groups are bonded and actively reinforcing the bulk. The peaks found at 1093 and 1035 cm^{-1} (figure 22 – N and Q) are attributed to C-O-C stretching of the polyether and the urethane components respectively, confirming that this is indeed a polyether-urethane polymer. Other peaks identification, available in table 10, further corroborates this evidence [46, 58, 59].

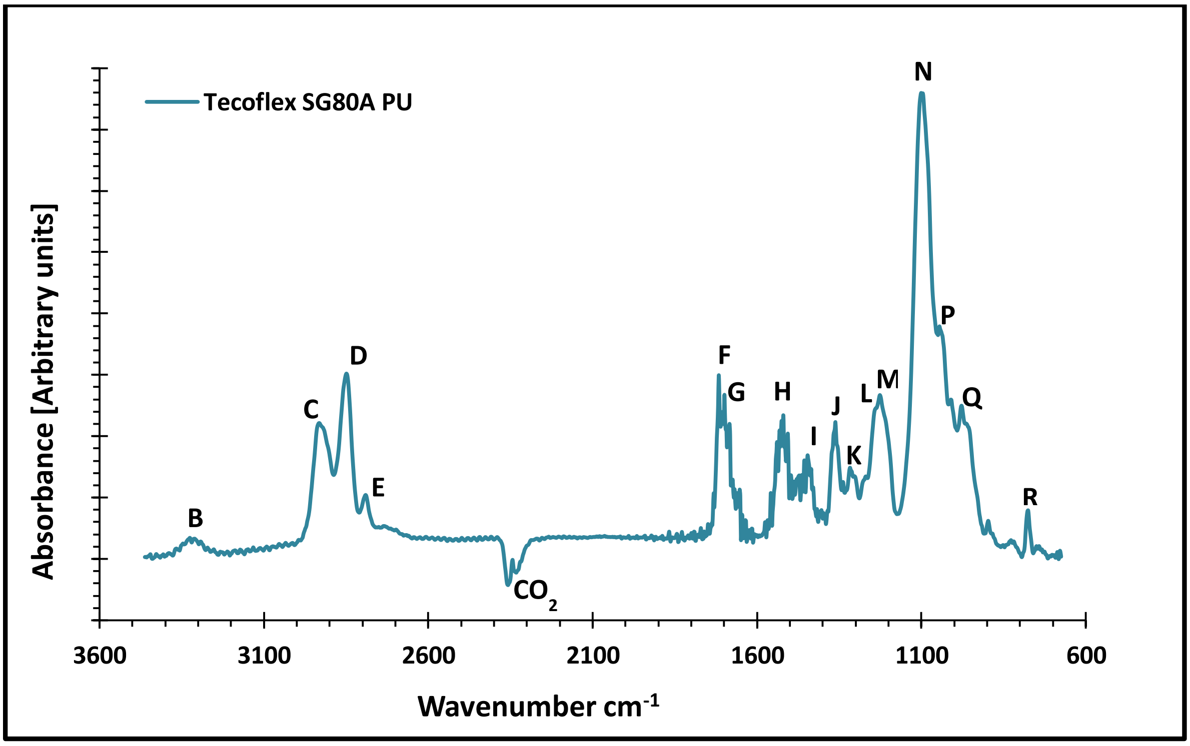

Figure 22. FTIR spectrum of the biomedical grade PU (reference: Tecoflex SG80A).

Table 10. Identification of the FTIR spectrum corresponding to the biomedical grade PU (reference: Tecoflex SG80A).

Peak label	Wavenumber		Chemical bond descripton
	reference	present work	
R	779	773	Ring breathing: cyclohexane
Q	900	974	Asymmetric ring stretching: cyclohexane
P	1044	1035	Asymmetric C-O-C stretching: urethane
N	1110	1093	Asymmetric C-O-C stretching: polyether
M	1228	1220	C-N stretching
L	1245	1232	CH_2 wagging
K	1320	1301	C-C stretching: cyclohexane
J	1367	1361	CH_2 wagging
I	1447	1440	CH_2 bending
H	1529	1520	C-N stretching & N-H bending
G	1701	1699	H-bonded C-O stretching
F	1719	1716	Free C=O stretching
E	2795	2783	Symmetric CH_2 stretching: αC of polyether
D	2854	2845	Asymmetric CH_2 stretching: αC/βC of polyether & cyclohexane
C	2933	2916	Asymmetric CH_2 stretching: βC polyether & cyclohexane
B	3323	3294	H-bonded N-H stretching
A	3445	-	Free N-H stretching

B. Differential scan calorimetry: DSC

The differential calorimetric assay underwent by Tecoflex SG80A in the temperature range of -60 ºC < T < 200 ºC is described in figure 23 where a typical behaviour of a linear polyether-urethane polymer is displayed. On figure 23 the DSC curves of tecoflex SG80A are presented as run1, run2 and cast. The cast curve refers to the polyurethane film that was after solvent evaporation at 37 °C without any subsequent thermal treatment. Run1 refers to the same polymer but submitted to a drying step at 70 °C after casting in order to release the moieties that might have been present.Run2 refers to the same sample used in run1 which further was subjected to the same assay as a way to clear undesired peaks and reveal more accurately the PU behaviour. Typically polyurethanes have at least one glass transition temperature originated by the soft segments mobility increase, one crystallization temperature associated to the hard segments ordering and a melt temperature at which the polymer is in a viscous state. The common features to all the samples are the glass transition temperature T_g under 0 °C, given by the endothermic inflection point, the crystallization temperatures, revealed by the exothermic transformations above 60 °C and a melt temperature above 140 °C, given by the endothermic transformations.

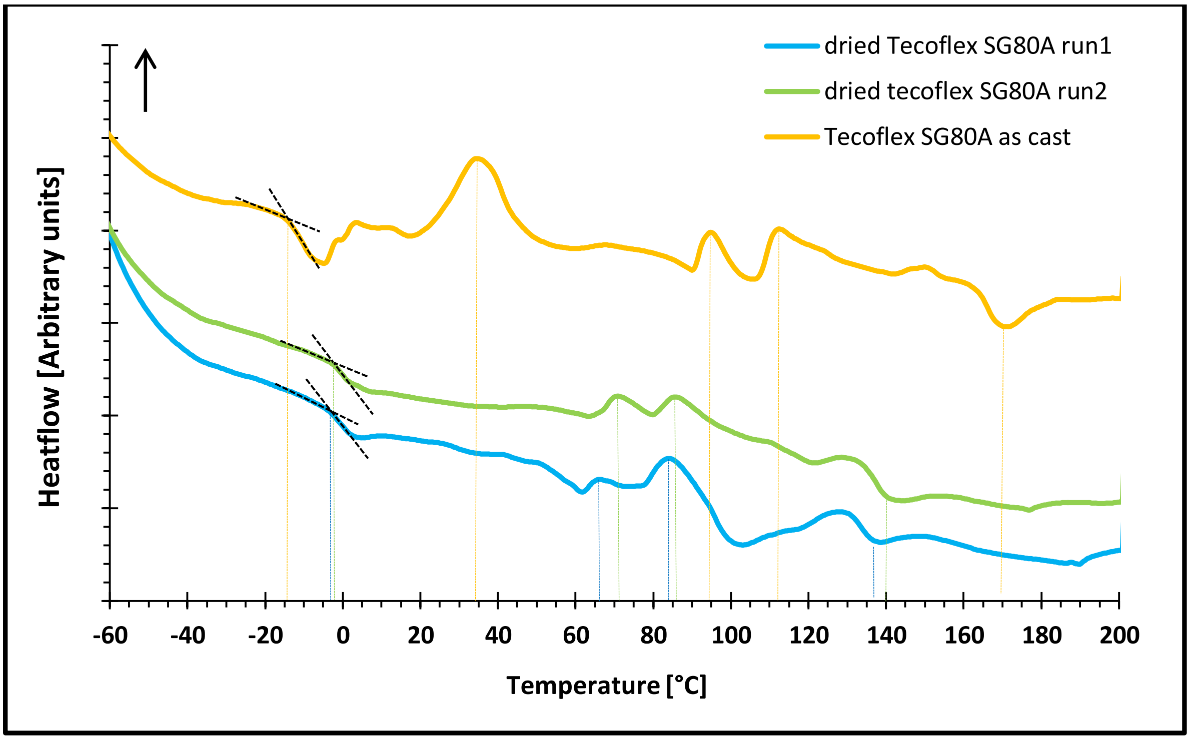

Figure 23. DSC curves of the biomedical grade PU tecoflex SG80A. Run 1 and 2 (curves blue and green, respectively) stand for PU dried at 70 °C to release adsorbed moeties being the second run carried out to reveal more acurate exo/endothermic behaviours location; the yellow curve respects the PU as casted, without any thermal treatment after solvent evaporation at 37 °C.

Regarding the cast polymer some phenomena are evidenced along its DSC curve pathway. The first one, attributed to the softening of the soft segment, is identified at -15 °C (T_g) [37]; the second one appearing at 35 °C is probably due to the release of solvents. At 95 ºC and 112 °C the exothermal peaks are attributed to the crystallization temperatures reactions occur with the softening of the hard segments [37]. Both peaks may correspond to two different packings associated to hard chain segments with different lengths. The meltdown of the polymeric mass occurs at 170 °C. After drying the polymer at 70 °C (run1), the DSC curve changes as the glass transition temperature (T_g), the crystallization and melt temperatures are now detected at different values as compared to the cast sample. The peak previously detected at 35 °C is now completely absent thus agreeing with the former assignment of such peak to solvents release or degasification. The increase of T_g to about -4 °C may be viewed as a consequence of a better packing of the macromolecular soft segments enabled by the referred solvent degasification. As the solvents affected negatively the soft segment packing they were helping the hard segment packing. As this helpful contribution for packing consistency is lost, crystallization occurs sooner, at about 66 and 84 °C, and meltdown occurs in a broader temperature range, from 137 °C to about 190 °C. The second run of the same polymer denounces a more refined structure. Tg does not change too much as it appear at ~ -3 °C, indicating that the soft segments could not improve further their packing, but the effective changes in crystallization and melt temperatures (71, 82 and 140 °C respectively) point to a better packing of the hard segments [60].

3.3. Composites characterization

A. Attenuated total reflectance Fourrier transform infrared spectroscopy: ATR-FTIR

The ATR-FTIR spectra of ZnO composites with $2\%_{wt}$ and 50 $\%_{wt}$ nanoparticles can be observed in figure 24 and 25 respectively. The $2\%_{wt}$ composites FTIR spectra show almost no difference relative to the pure PU spectra, indicating no new covalent bonding between PU and ZnO particles. It was reported elsewhere [61] that in polyurethanes membranes filled with nanosized ZnO there is a new peak at 1619 cm^{-1} with the attenuation of the 1687 cm^{-1}. In $2\%_{wt}$ composites a new peak at 1614 cm^{-1} was found confirming the binding of ZnO to the polymer but no attenuation was detected. Also the change in peak at 3294 cm^{-1} due to H-bounded NH stretching indicates that ZnO particles may be bonded to it, thus acting in the reinforcement of the polymer matrix.

The $50\%_{wt}$ composites were so heavily loaded with ZnO particles that the spectra were completely deformed when compared to pure PU. As the typical peaks of PU disappear, the characteristic peaks of ZnO are found near the limit range of the equipment (between 500 - 600 cm^{-1}), and so they are not represented [62].

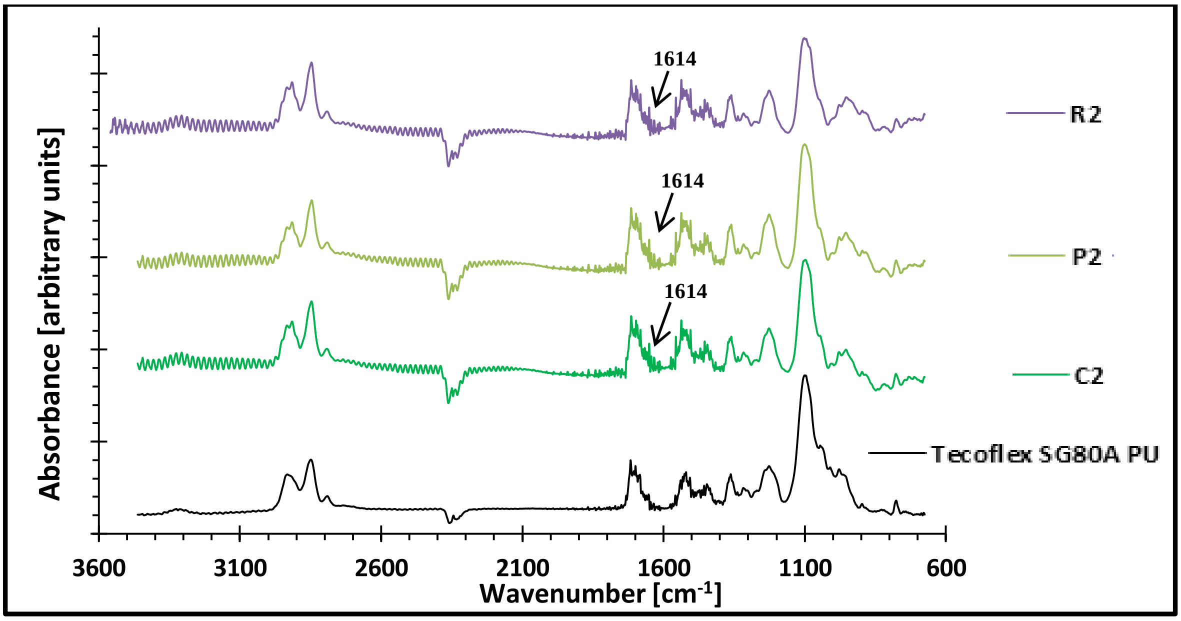

Figure 24. FTIR spectra of PU and 2%$_{wt}$ PU/ZnO composites (fillers are respectively cZnO in C2, pZnO in P2 and rZnO in R2).

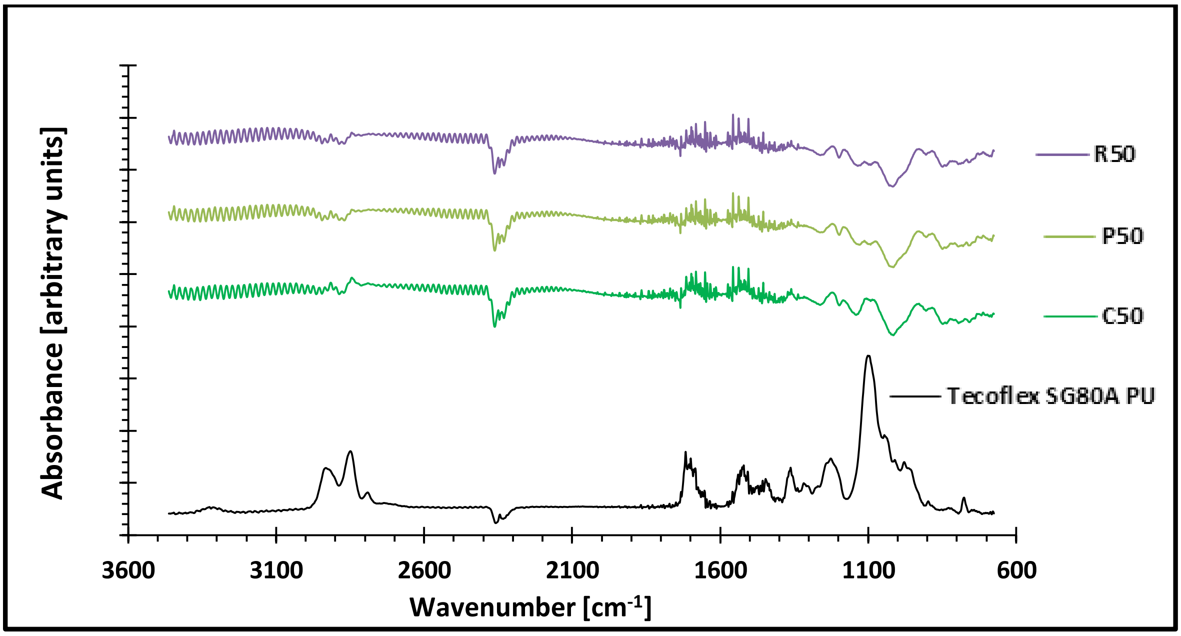

Figure 25. FTIR spectra of PU and 50%$_{wt}$ PU/ZnO composites (fillers are respectively cZnO in C50, pZnO in P50 and rZnO in R50).

B. Differential scan calorimetry: DSC

The effects of pZnO content on the PU matrix can be observed on figure 26. Two major changes occur, namely in the glass transition temperature and in the crystallization temperatures. With 2%$_{wt}$ ZnO particles the glass transition temperature diminishes from -3 °C to -13 °C and crystallization temperatures increases from 71 and 82 °C to, respectively, 77 and 93 °C. The presence of ZnO polar particles probably disrupts the packing of the non-polar soft segments of the PU and contributes to the higher packing of the polar hard segments. Considering the P2 composite structure as a whole, it seems that the addition of 2%$_{wt}$ ZnO to PU facilitates the chains mobility when heating during the thermal treatment, which corresponds in the DSC curve to a decrease in the glass transition temperature, when compared with the unfilled PU [62]. As to the crystallization temperature, assuming that ZnO particles promote a denser packing of the rigid PU segments by linkage with urethane group [62], it is likely that a higher temperature should be required to rearrange the PU structure in the composite. The melting temperatures basically remain the same, at 140 °C.

The PU loaded with 50%$_{wt}$ ZnO particles has suffered heavier changes, namely the appearance of two T_gs, at -20 °C and 15 °C. The T_g diminished to about -20 °C due to ZnO particles influence which also aided in the hard chains packing leading to a raise in crystallization temperatures to 81 and 98 °C. The new T_g at 15 °C (figure 26) appears because of particles agglomeration, as some zones of the polymeric mass becomes free of the interaction of ZnO particles and hard segments influence, the soft segments could organize themselves better reflected on the new T_g. With this ZnO content the melt temperature also doesn’t change.

It should be stressed that in both composites ZnO particles appeared well connected with the PU, thus acting as reinforcing filler and both formulations remain stable at temperatures between 34 and 42 °C, the range of the human body temperatures.

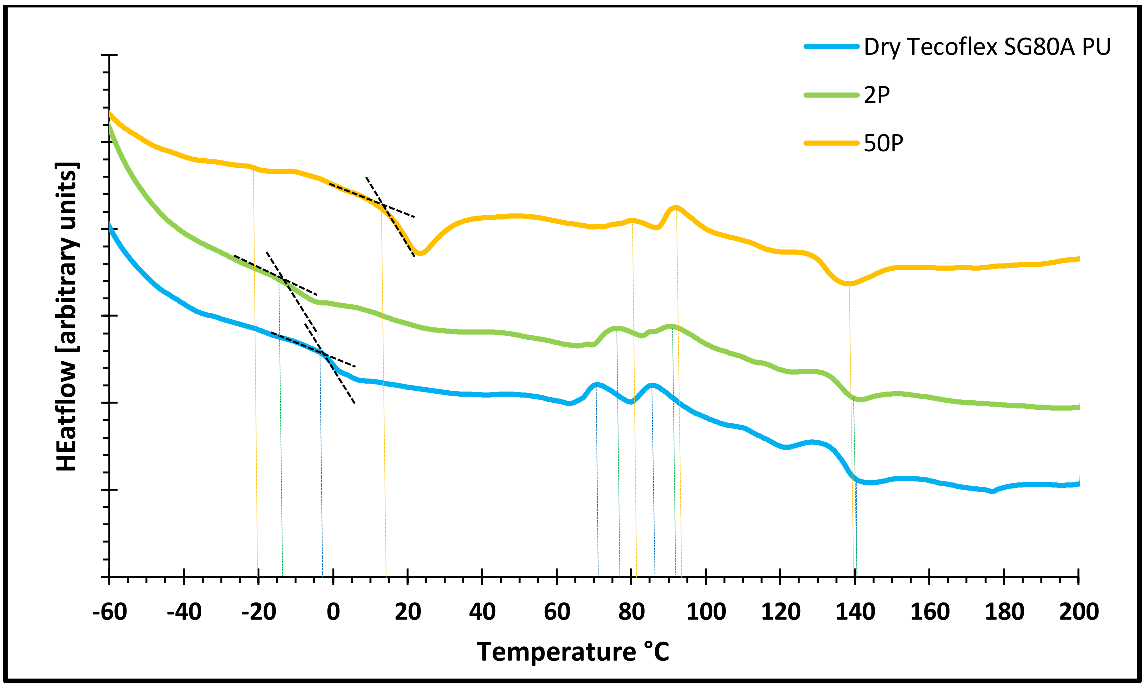

Figure 26. DSC curves of the biomedical grade PU tecoflex SG80A (blue), 2%$_{wt}$ pZnO composite (2P - green) and 50%$_{wt}$ pZnO composite (50P - orange).

C. *In vitro* tests

C1. Bioactivity

Bioactivity assays were performed on 2%$_{wt}$ ZnO composites (C2, P2, and R2) and 50%$_{wt}$ ZnO composites (C50, P50 and R50) - where C, P and R refer to the type of ZnO filler, respectively cZnO, pZnO and rZnO and on pure polyurethane. Tests were carried out for time periods up to 21 days.

The pure polyurethane didn’t show any calcium-phosphor compounds precipitation at the surface even after 21 days of immersion (figure 27), and thus, as expected, it is concluded to be a non-bioactive material.

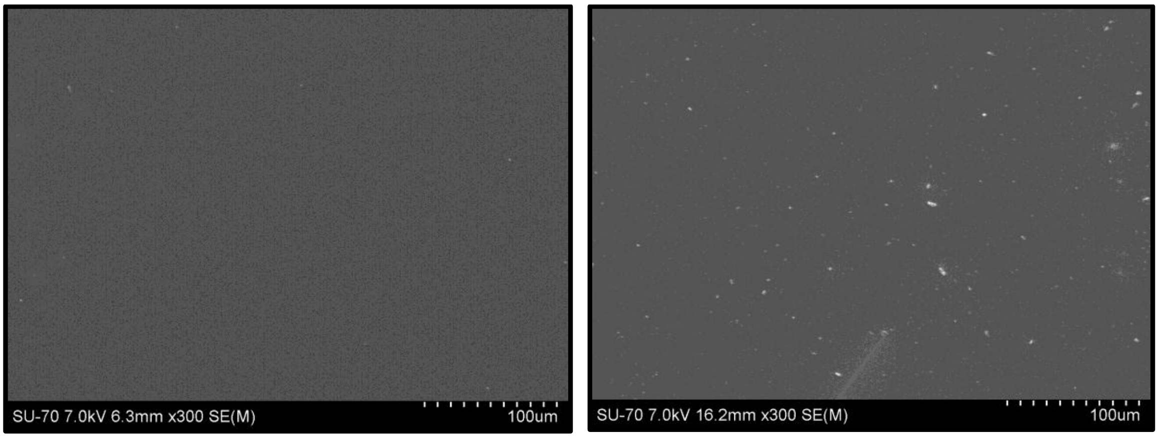

Figure 27. SEM images of polyurethane surface: A) after 1 day of immersion in SBF and B) after 21 day of immersion in SBF.

The C2 composite after 1 day of SBF immersion appears to have a very thin layer of precipitate (figure 28A), but after 7 days no precipitate was found (figure 28B) and after 21 days some agglomerates were found (figure 28C).

The formed precipitates after day 1 correspond possibly to a transient precipitate which is thought to be mainly related to a Zinc compound as revealed by EDS analysis (figure 28D) although the phase could not be identified by XRD due to its low amount. The peak in EDS analysis at 1 keV can be also attributed to sodium, Na, which is present in the SBF solution, and thus the possibility of sodium compounds being formed is not ruled out. The ICP analysis showed that some Zn^{2+} ions were released to SBF media (figure 31) from the very beginning confirming the idea of a Zinc precipitate being formed whereas phosphate and calcium SBF solution depletion were negligible even after 21 days of immersion (figures 30 and 29, respectively). It is thus concluded that the formed precipitated is mainly a Zn-based precipitate with a minor amount of a calcium phosphate being detected after 21 days according to EDS analysis as ICP analysis appear to be less sensitive to the Ca and P withdraw from SBF solution. It is reported that the Zn^{2+} released from bone cements enhances apatite phases formation [33, 34] and in some cases these are formed in polyurethanes in hydrophilic segment of polyetherurethanes, through calcium attraction to the oxygen ether bond [40].

In this way although the pure polyurethane films did not show any precipitates formation, even after 21 days of SBF immersion (figure 27), with the aid of released Zn^{2+} ions the formation of precipitated phases could be enhanced.

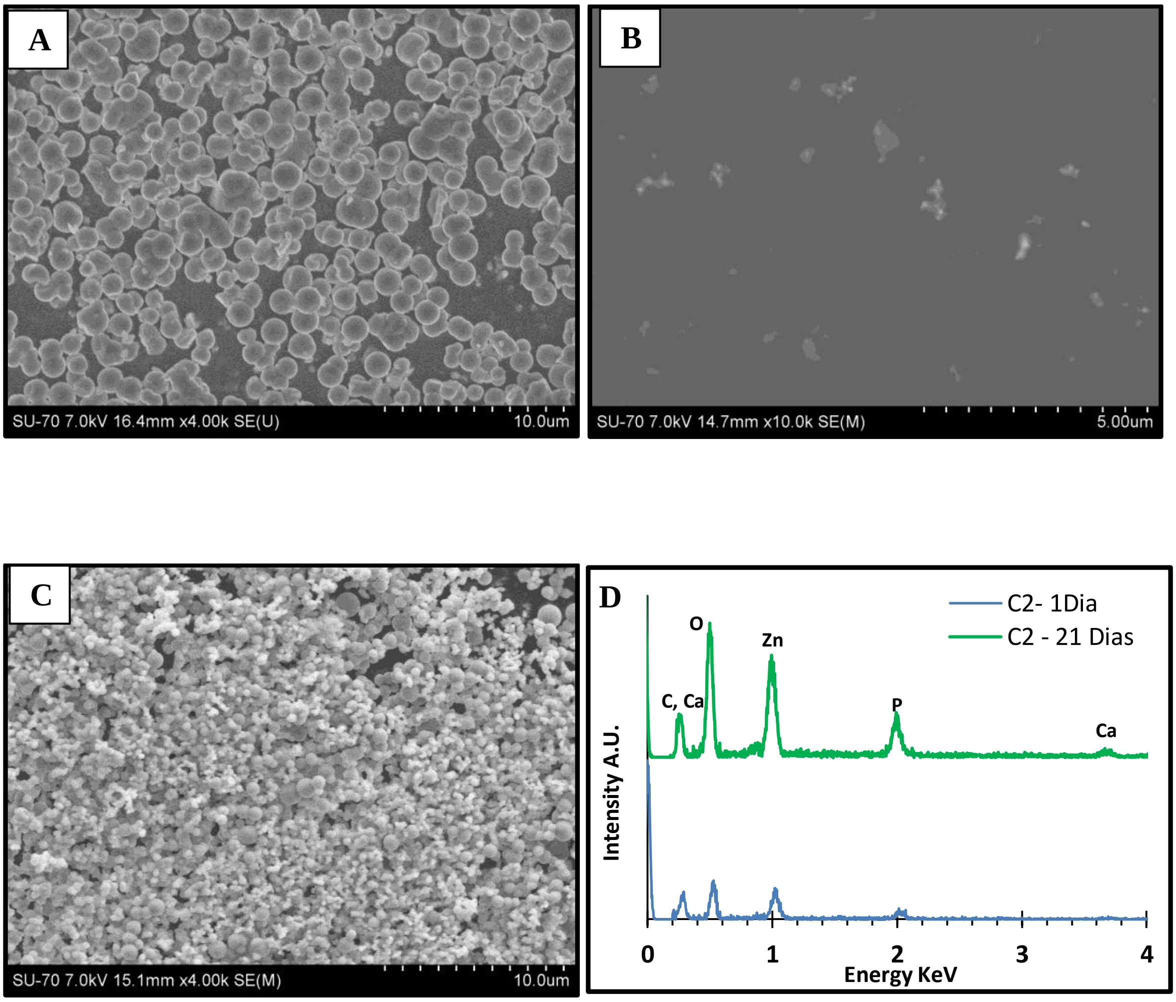

Figure 28. SEM image of C2 composite after soaking in SBF for: A) 1 day. B) 7 days. C) 21 days. D) EDS analysis of the 1 day and 21 days layers.

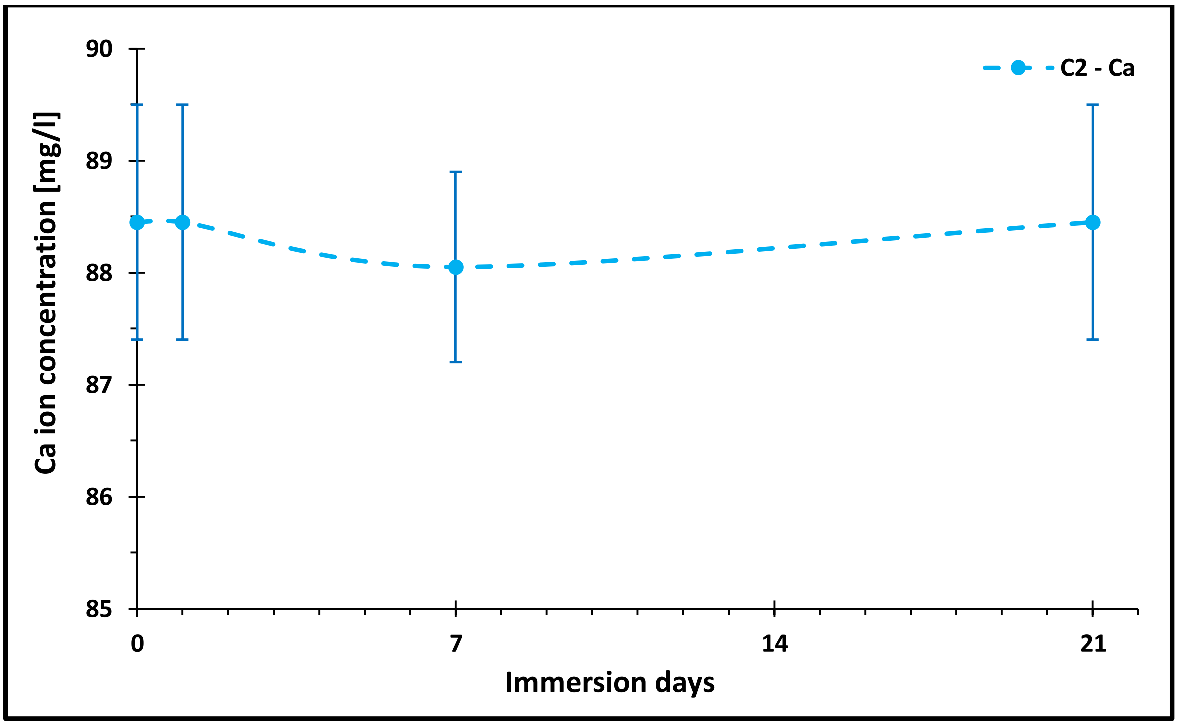

Figure 29. Ca ion concentration of the SBF solution after immersion of C2 composites (dashed lines serve to guide the eyes).

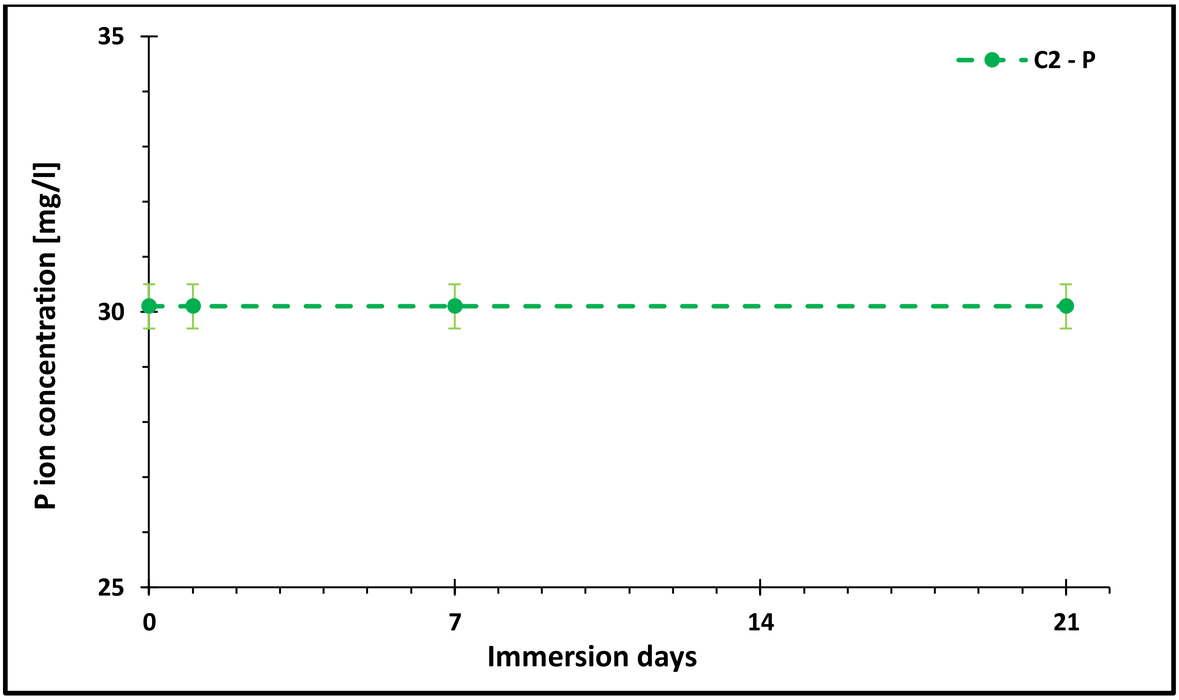

Figure 30. P ion concentration of the SBF solution after immersion of C2 composites (dashed lines serve to guide the eyes).

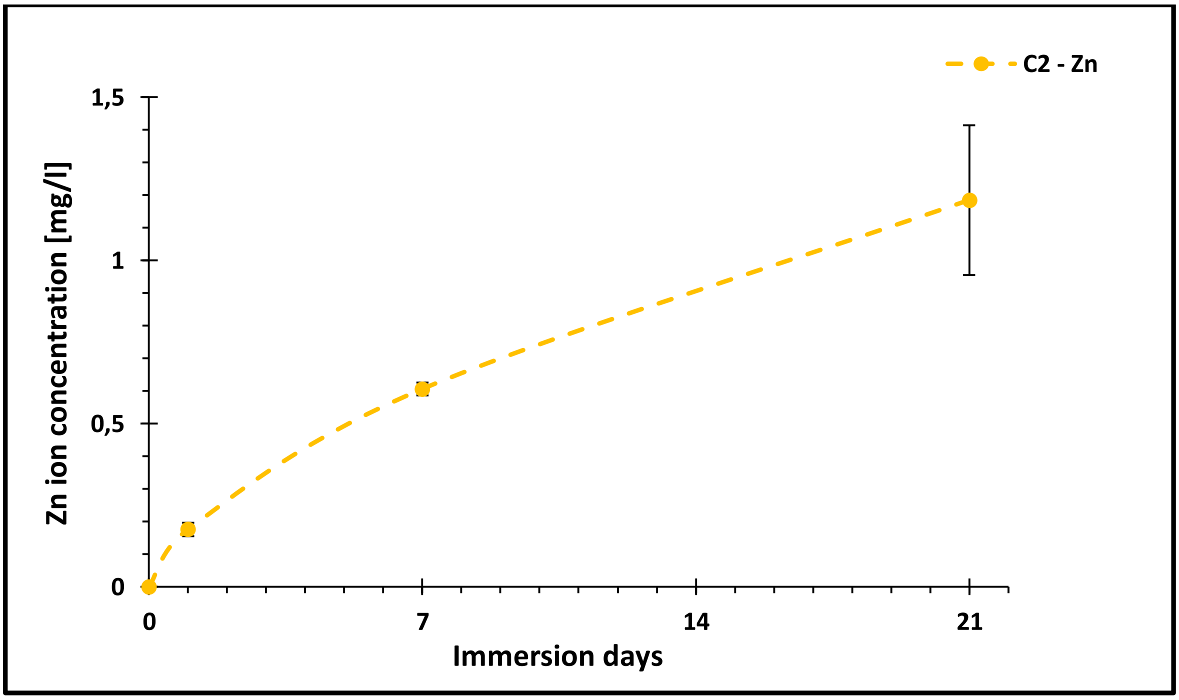

Figure 31. Zn ion concentration of the SBF solution after immersion of C2 composites (dashed lines serve to guide the eyes).

The P2 composites behaviour followed basically the same pattern of C2 composites, showing some spots of precipitated phases at the end of 1, 7 and 21 days (figure 32: A, B, C respectively) accompanied by the release of Zn^{2+} ions from the composite films to the liquid media (figure 35). The EDS analysis (figure 32D) confirms that the elements present are P, Zn and Ca. The P2 behaviour is further confirmed by ICP analysis (figures 33 and 34), with small amounts of Ca and P being lost by the SBF solution and a simultaneous Zn^{2+} enrichment. These results further confirm the possibility of phosphorus, zinc and calcium compounds being formed during the SBF assay.

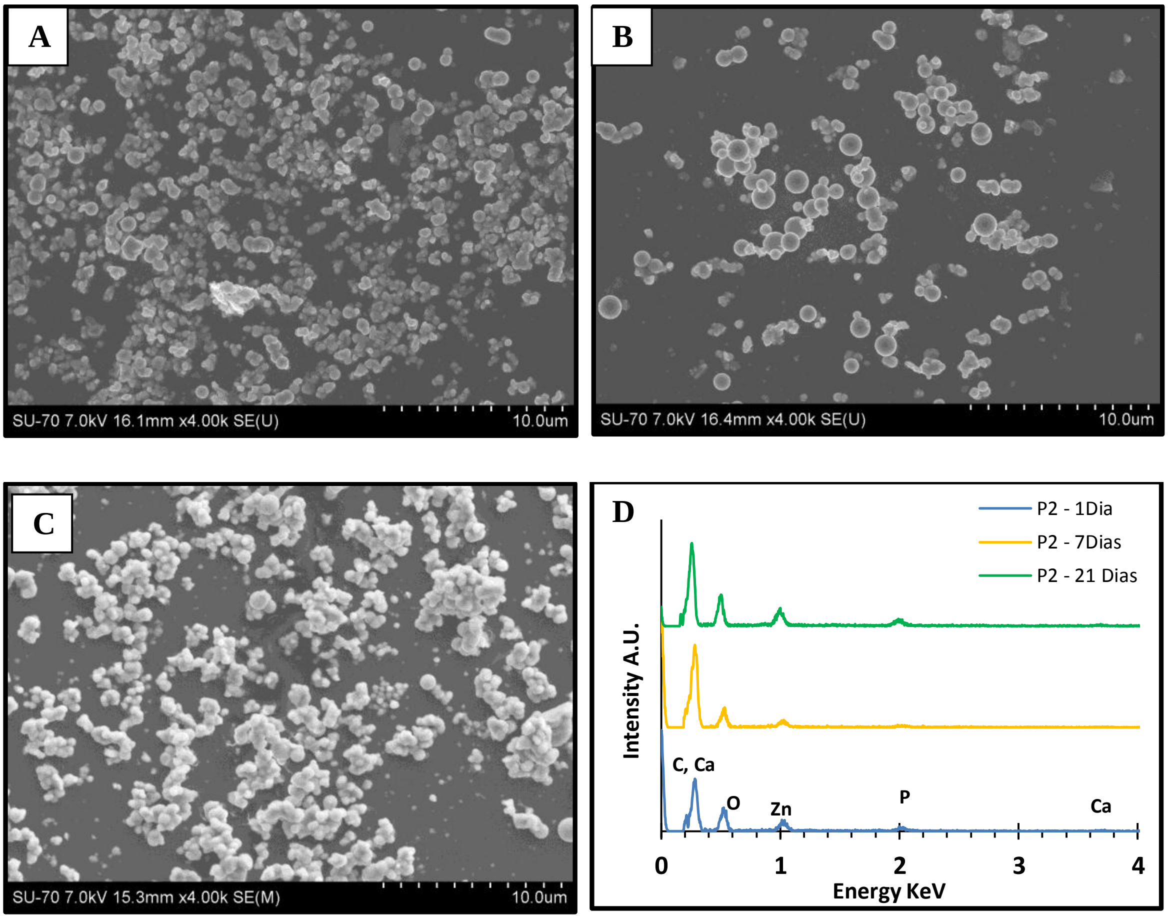

Figure 32. SEM image of P2 composite after soaking in SBF for: A) 1 day. B) 7 days. C) 21 days. D) EDS analysis of the 1 day, 7 days and 21 days layers.

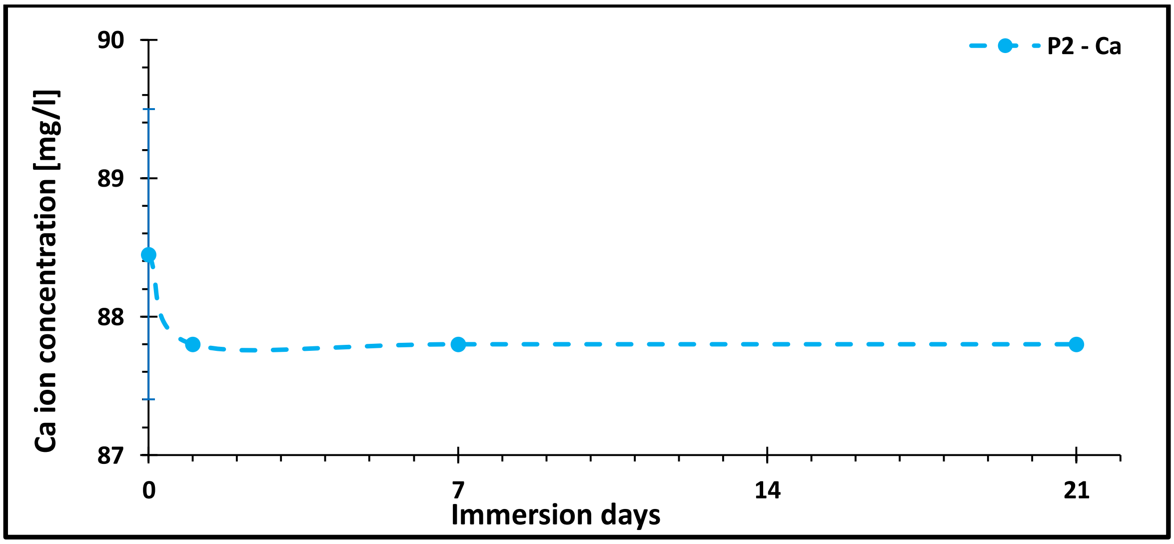

Figure 33. Ca ion concentration of the SBF solution after immersion of P2 composites (dashed lines serve to guide the eyes).

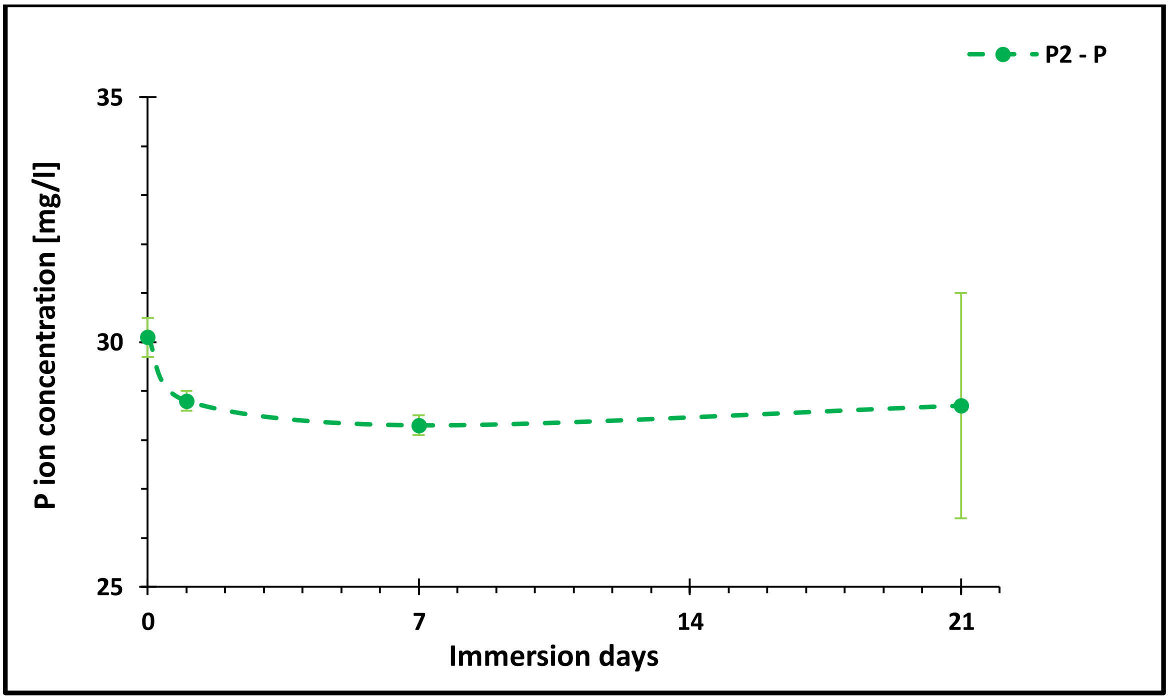

Figure 34. P ion concentration of the SBF solution after immersion of P2 composites (dashed lines serve to guide the eyes).

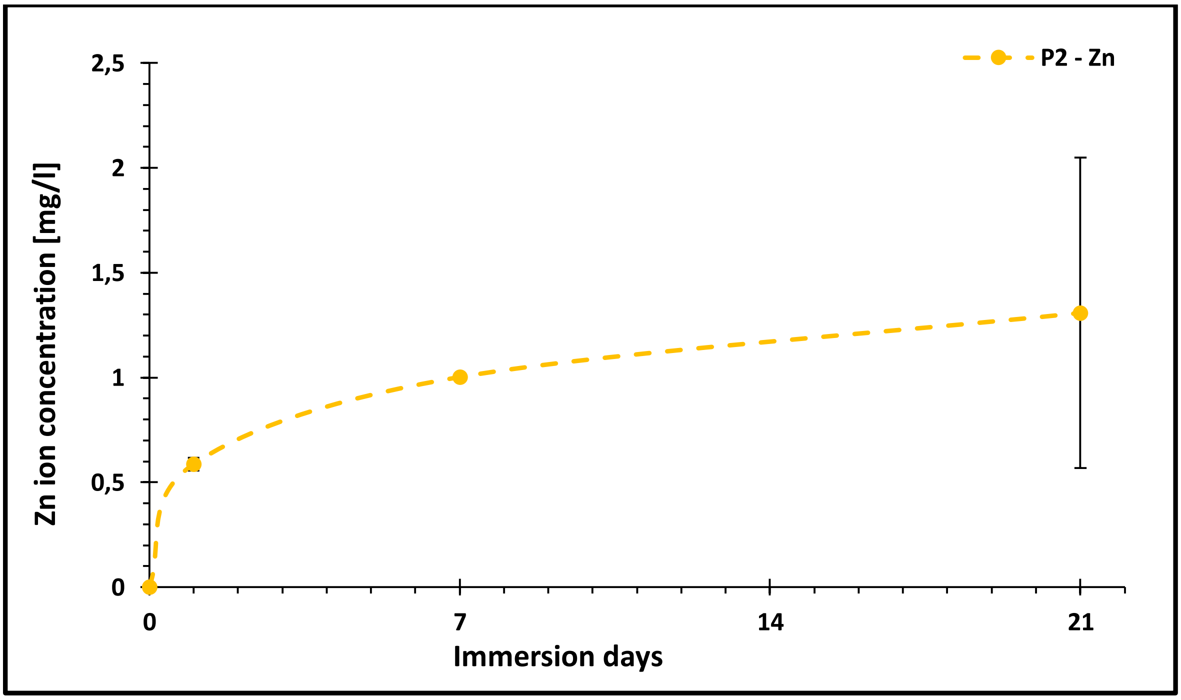

Figure 35. Zn ion concentration of the SBF solution after immersion of P2 composites (dashed lines serve to guide the eyes).

R2 composites followed the same trend of both C2 and P2 composites, as small amounts of precipitate were deposited during the 21 days of immersion (figure 36A, B, C and D). The ICP analysis (figure 39) detected small amount of Zn^{2+} ions in the SBF solution released by the composite, with a minor loss of calcium and phosphorus (figures 37 and 38, respectively). Once again the phases formed are thought to be possibly phosphorus, calcium and zinc compounds.

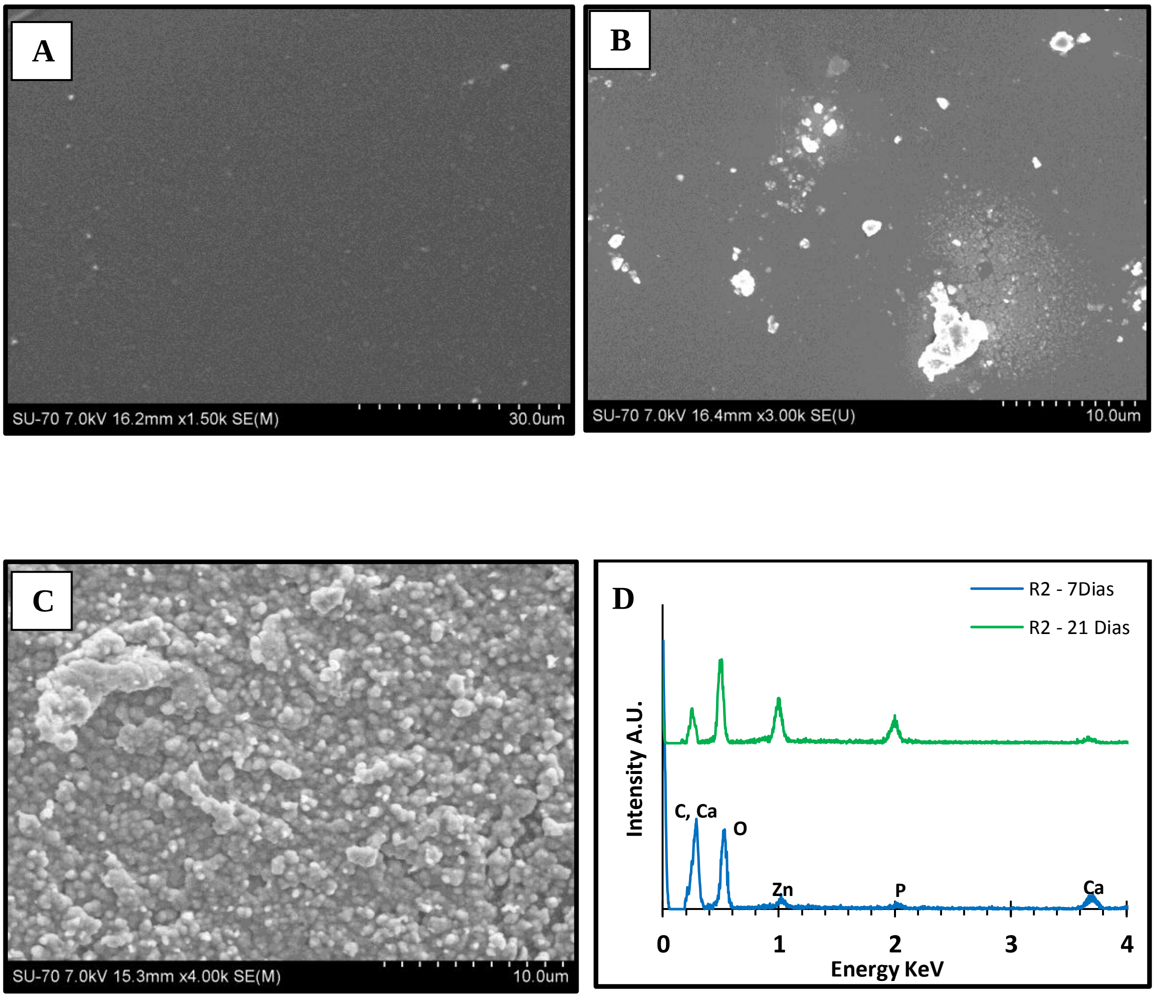

Figure 36. SEM image of R2 composite after soaking in SBF for: A) 1 day. B) 7 days. C) 21 days. D) EDS analysis of the 7 and 21 days layers.

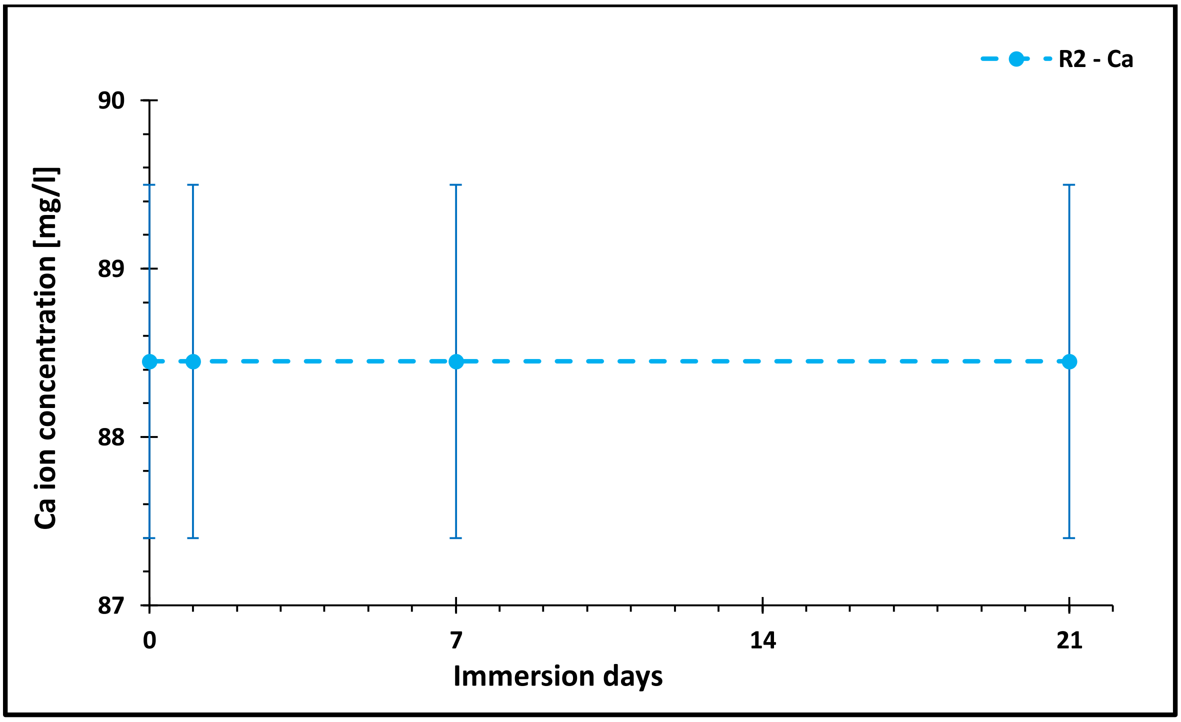

Figure 37. Ca ion concentration of the SBF solution after immersion of R2 composites (dashed lines serve to guide the eyes).

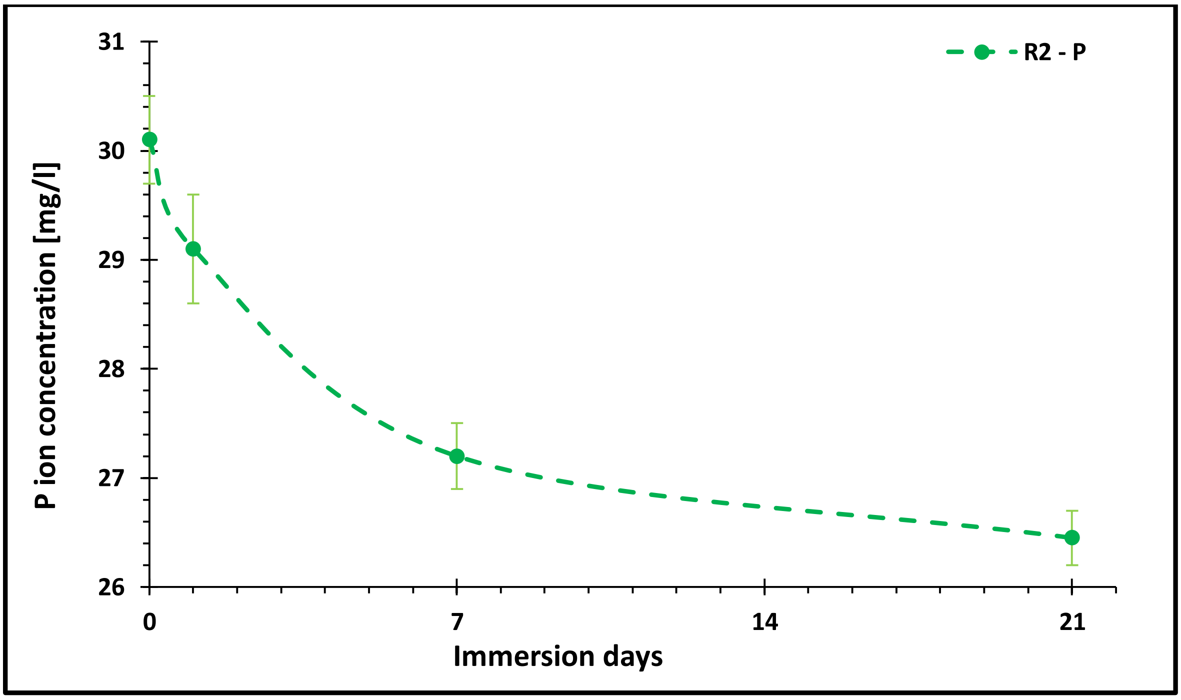

Figure 38. P ion concentration of the SBF solution after immersion of R2 composites (dashed lines serve to guide the eyes).

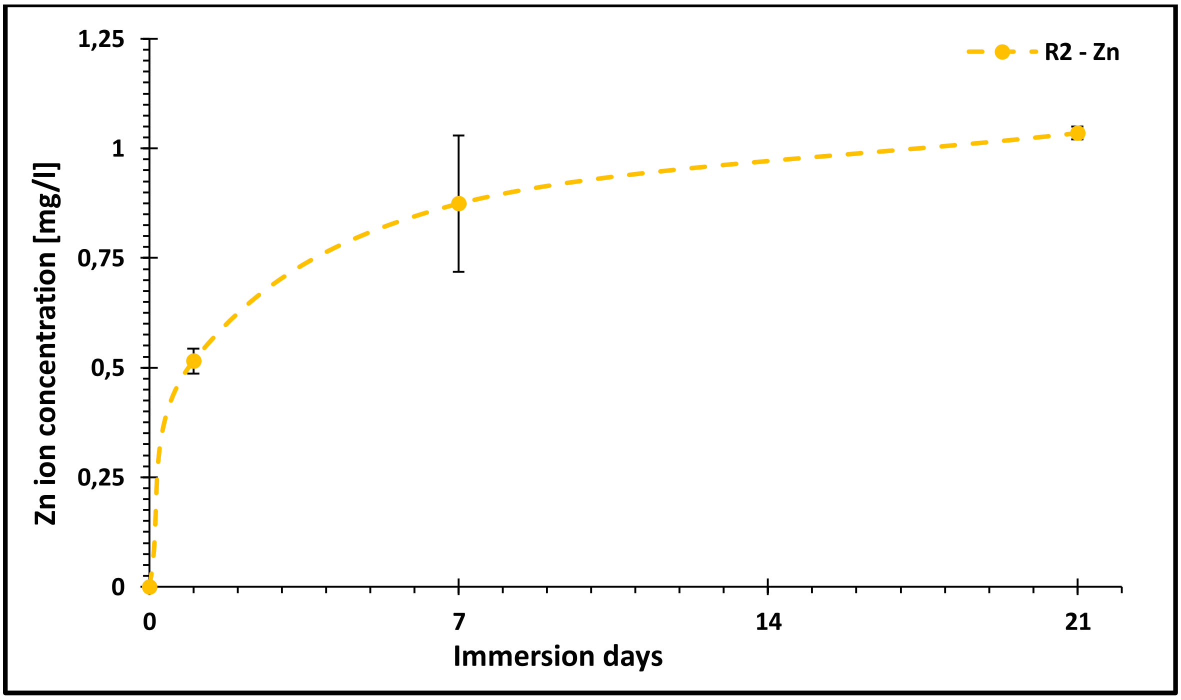

Figure 39. Zn ion concentration of the SBF solution after immersion of R2 composites (dashed lines serve to guide the eyes).

The C50 composites exhibit the behaviour shown in figure 40: A, B and C. The addition of 50%$_{wt}$ of cZnO particles to PU did not change the behaviour of the PU as very small quantities of precipitate were deposited on the composites surface throughout the 21 days, which are believed to be phosphorus; calcium zinc compounds (figure 40 D). The low quantities of Zn^{2+} released (figure 43) to the SBF solution are probably due to the low surface area and high crystallinity of the powder; After 7 days of immersion the quantity diminishes and this can be possibly explained by the incorporation of Zn ions in the precipitated phases. The aluminium detected in EDS belongs to the sample holder. It seems that the crystallization of the new phases is not enhanced when commercial ZnO powder having a low specific surface area and a high crystallinity is involved in the composite formulation.

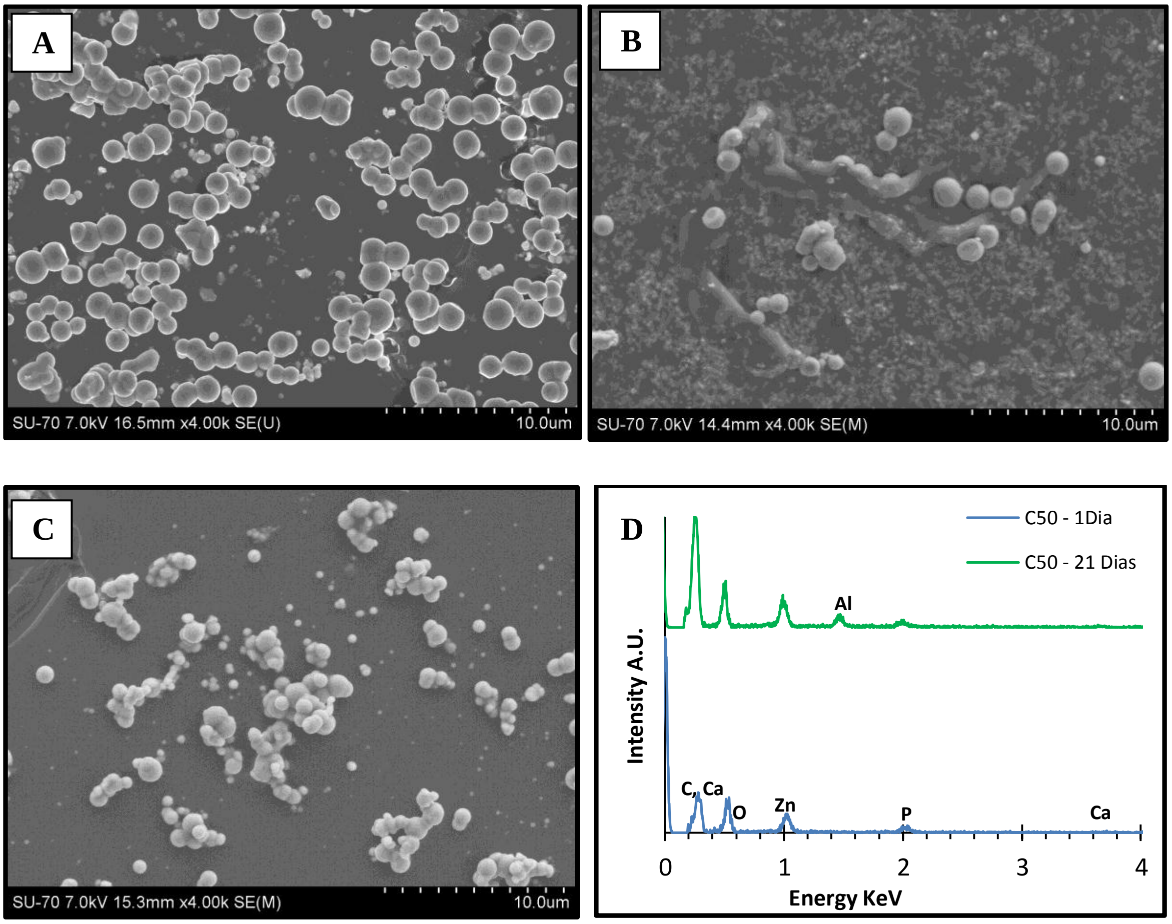

Figure 40. SEM image of C50 composite after soaking in SBF for: A) 1 day. B) 7 days. C) 21 days. D) EDS analysis of the 1 day and 21 days layers.

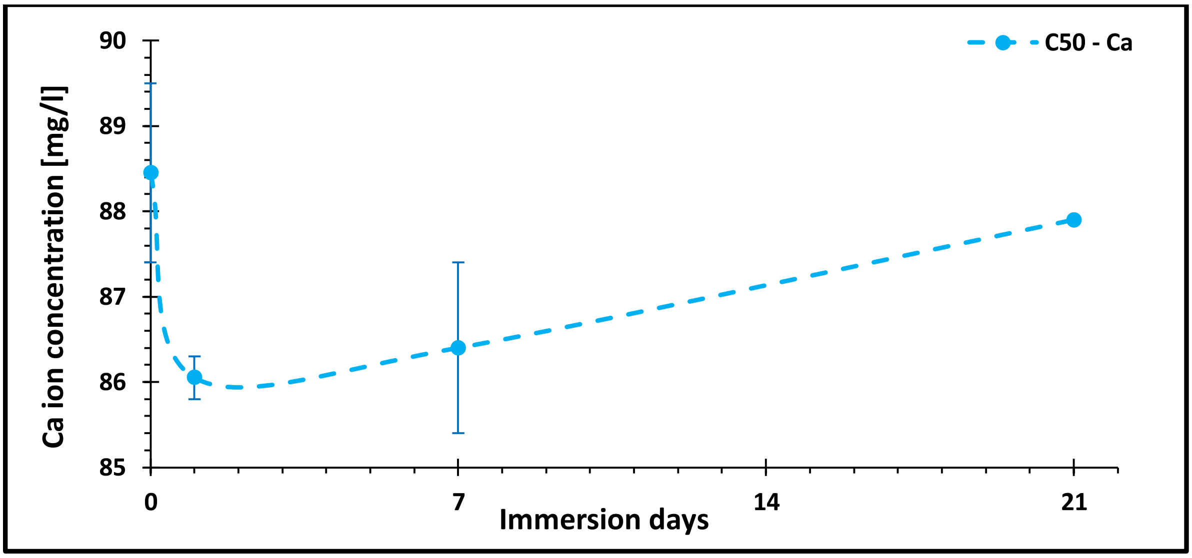

Figure 41. Ca ion concentration of the SBF solution after immersion of C50 composites (dashed lines serve to guide the eyes).

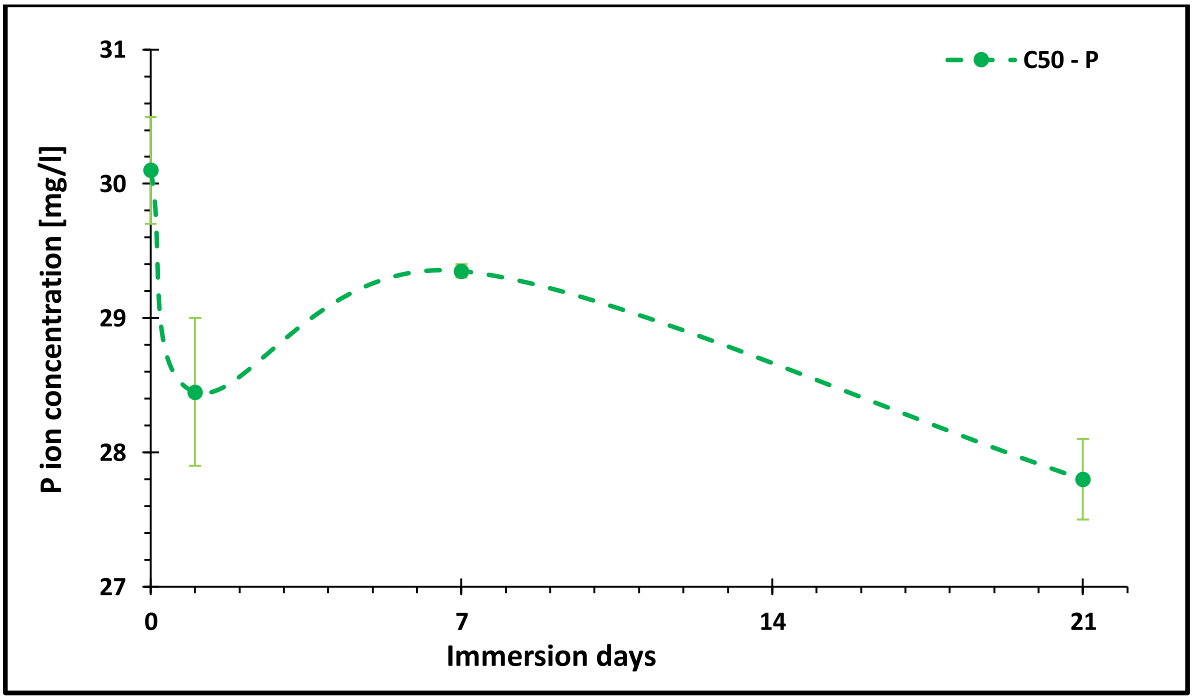

Figure 42. P ion concentration of the SBF solution after immersion of C50 composites (dashed lines serve to guide the eyes).

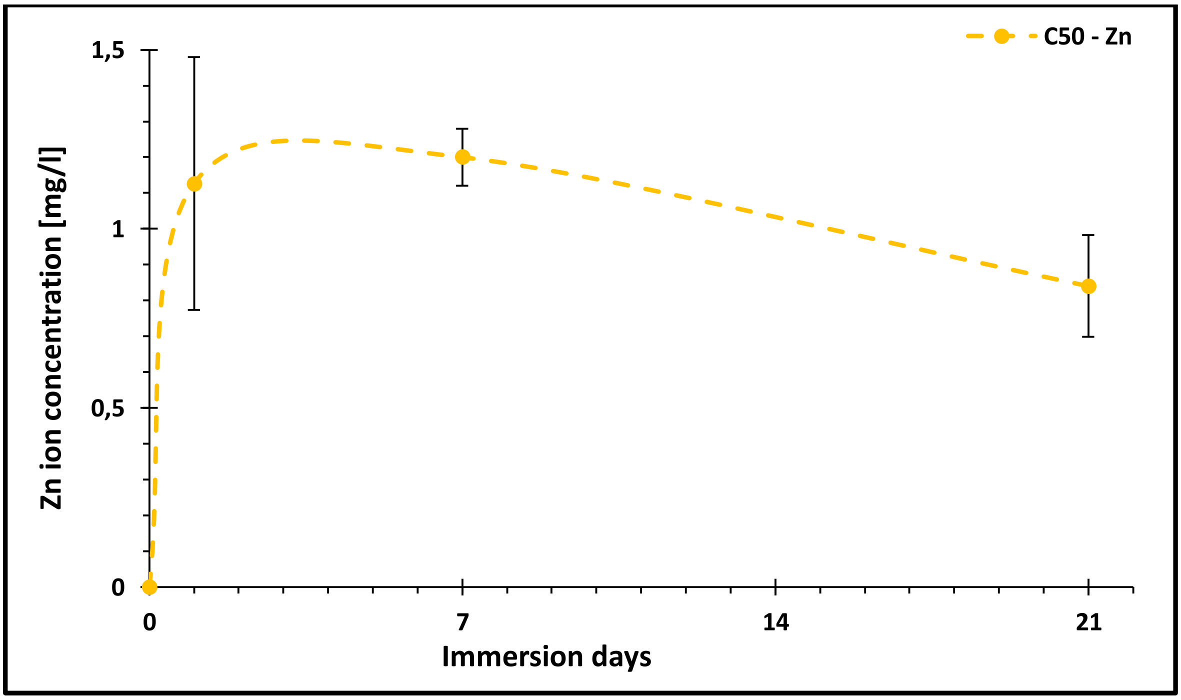

Figure 43. Zn ion concentration of the SBF solution after immersion of C50 composites (dashed lines serve to guide the eyes).

The P50 composites show a different behaviour when compared to the other samples as larger quantities of precipitate were deposited on the surface of the films (figure 44A, B, C). The EDS (figure 44D) analysis confirms that the elements present are P, Ca and Zn and ICP spectroscopy (figure 45) reveals that almost all of the calcium consumption from the SBF solution took place during day 1.

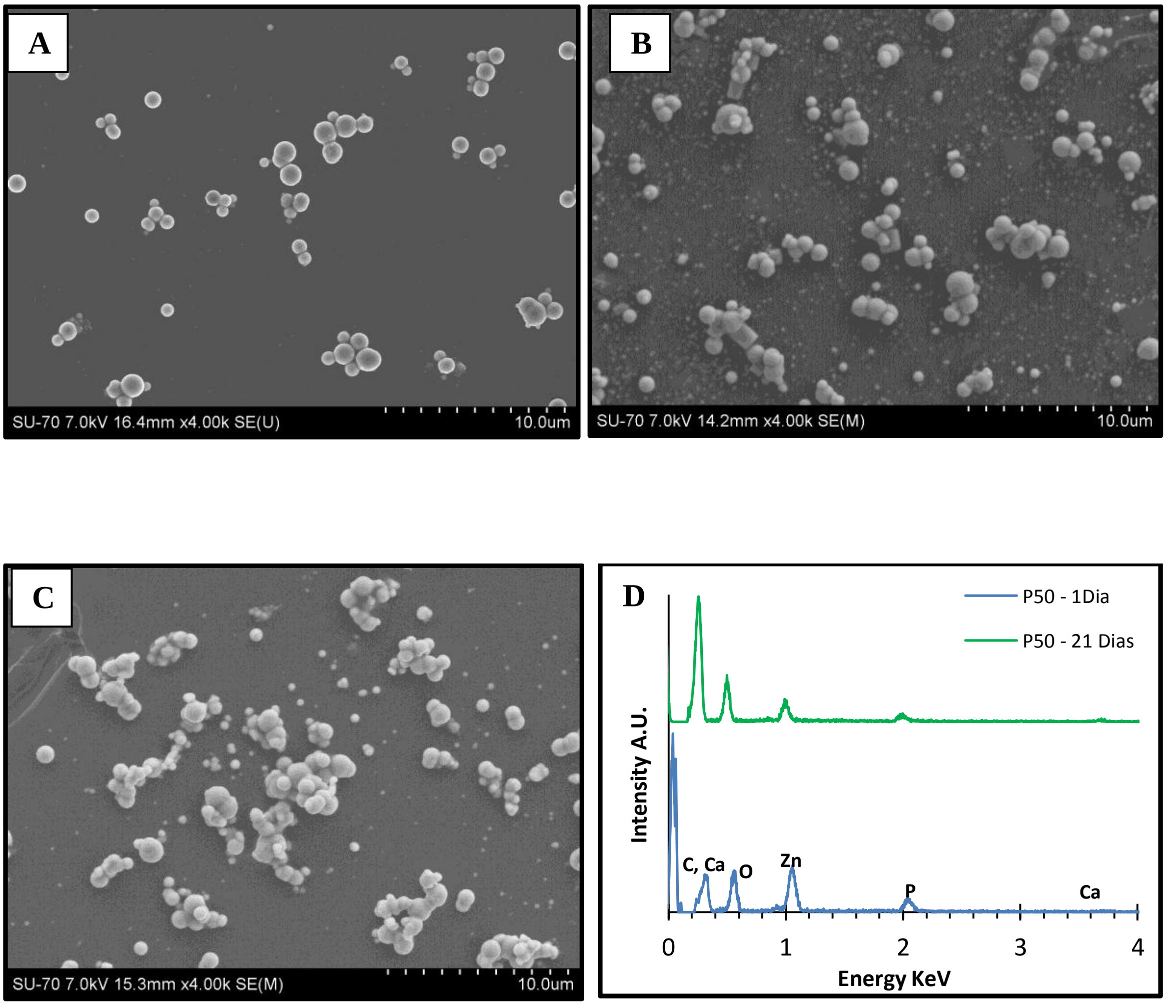

Figure 44. SEM image of P50 composite after soaking in SBF for: A) 1 day. B) 7 days. C) 21 days. D) EDS analysis of the 1 day and 21 days layers.

ICP also reveals that both the calcium and phosphorus (figure 46) amounts consumed from the SBF solution were much larger than those observed for the composites analysed before (C2, P2, R2 and C50), as well as the Zn^{2+} ions released from the composite (figure 47). There are two main factors that have to be taken into account for explaining this behaviour: the specific surface area and the crystallinity of the powders. This powder has large specific surface area (SSA) and thus is more reactive than the one with lower surface area as cZnO, It seems that its lower crystallinity and high SSA enhance ZnO dissolution. P50 composite results also indicate the possibility of Zn^{2+} ions being incorporated in the phosphorus and calcium compounds network. The effect of Zn^{2+} in calcium phosphates phase formation was addressed before, and the high released amount of Zn^{2+} could promote further precipitation by saturating the solution with Zn^{2+} ions that could possibly lead to the formation of new Zn-based compounds. Contrarily to the powder referred before this powder seems to be bioactive.

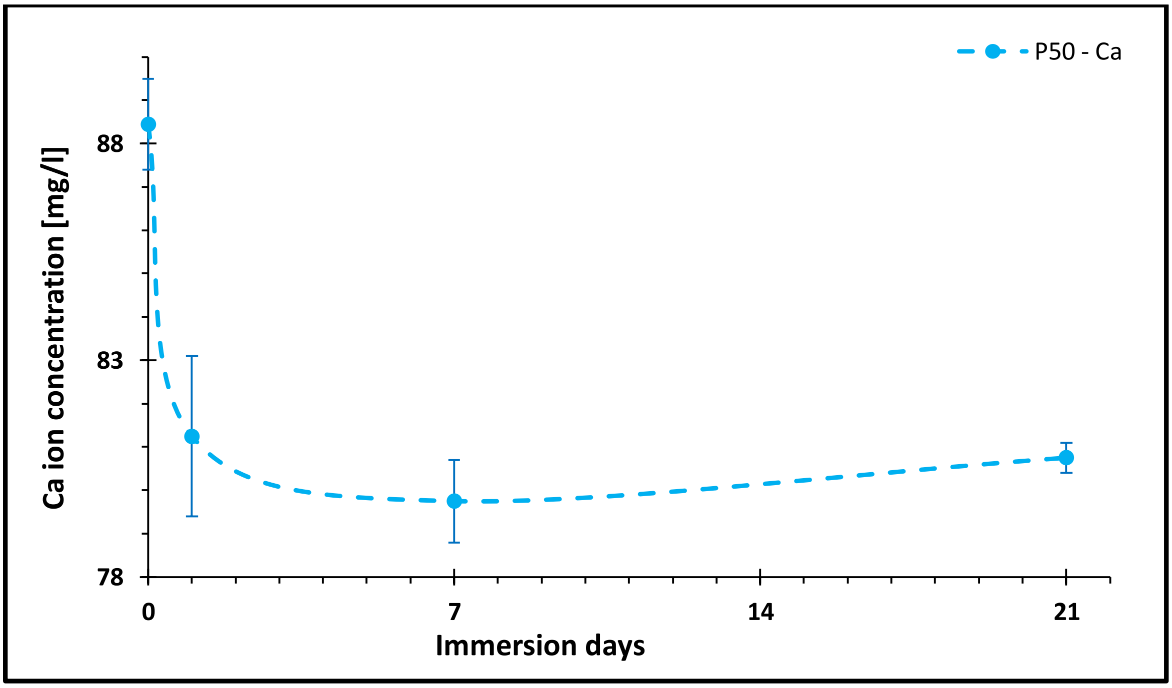

Figure 45. Ca ion concentration of the SBF solution after immersion of P50 composites (dashed lines serve to guide the eyes).

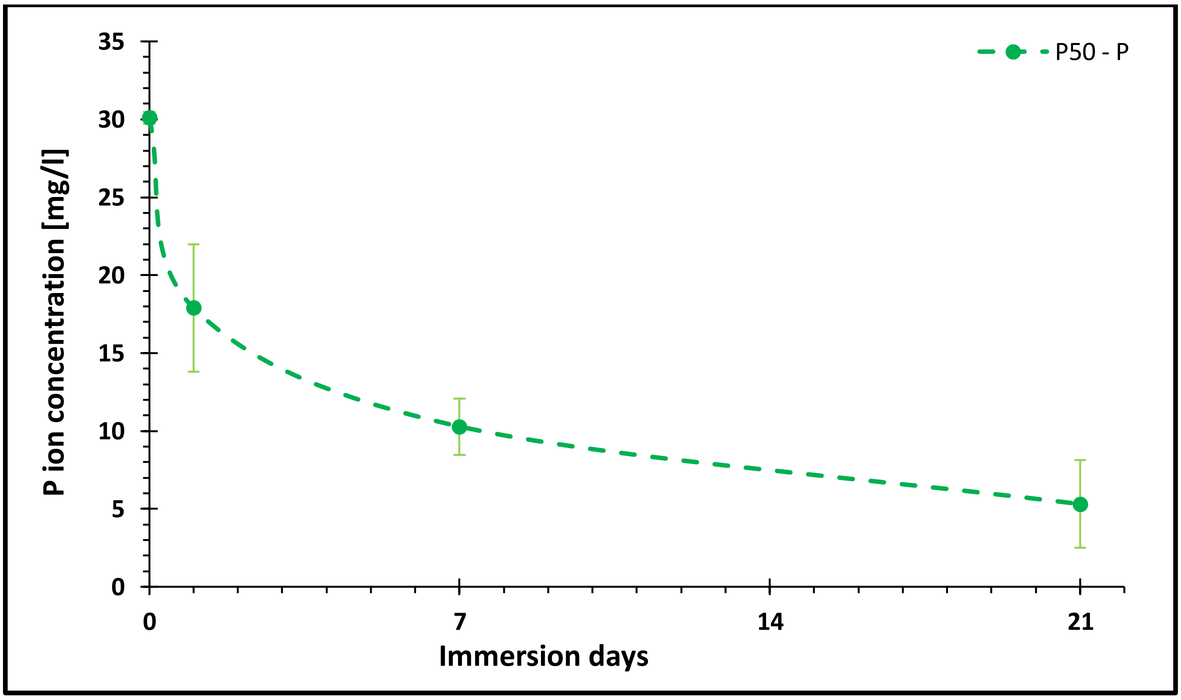

Figure 46. P ion concentration of the SBF solution after immersion of P50 composites (dashed lines serve to guide the eyes).

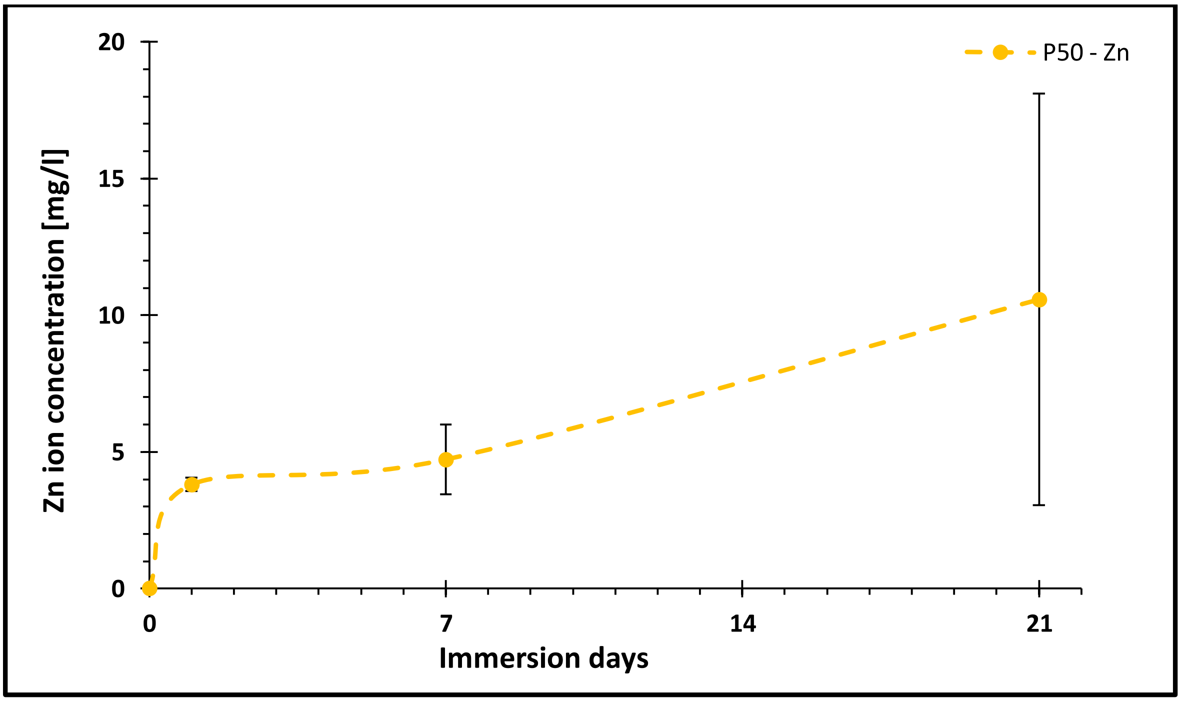

Figure 47. Zn ion concentration of the SBF solution after immersion of P50 composites (dashed lines serve to guide the eyes).

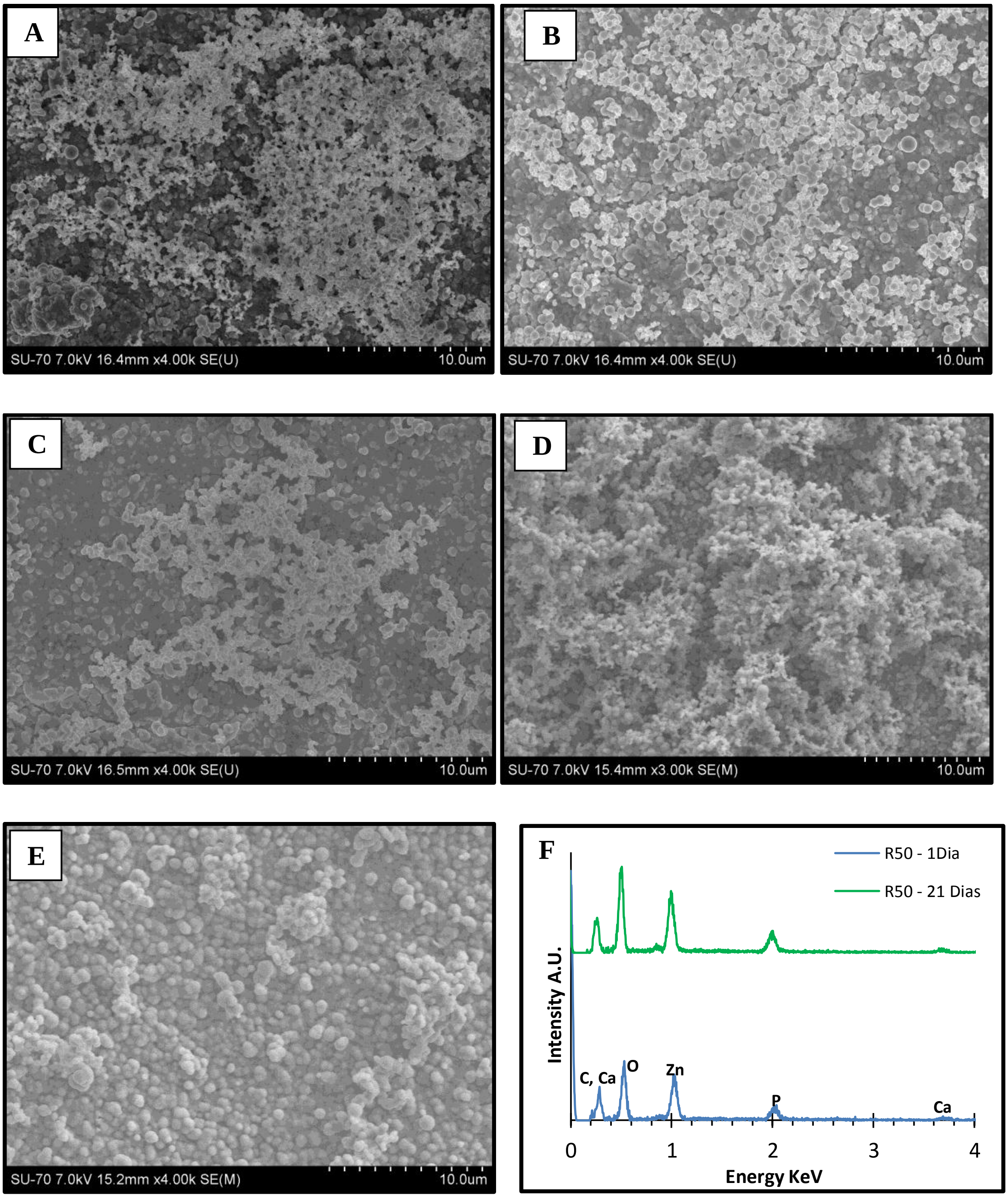

Figure 48. SEM image of R50 composite after soaking in SBF for: A) 1 day. B) 3 days. C) 7 days. D) 14 days. E) 21 days. D) EDS analysis of the 1 day and 21 days layers.

R50 composites exhibit heavy amounts of precipitate (figure 48 A-E) layers formed from day 1 till the end of the bioactivity assay at 21 day, which makes this composite probably bioactive. SEM images correspond to days 1, 3, 7, 14 and 21 (Figure 48A, B, C, D, E respectively) and the EDS analysis (figure 48F) shows that the elements present are Ca, P and Zn. The Zn^{2+} ions release is heavier that for the previous composites, and thus Zn^{2+} incorporation on calcium phosphate compounds network was also the largest as observed in the ICP analysis of SBF (figures 49-51). This powder, pZnO, was the one having the highest SSA and crystallinity as compared to the other powders, and thus supports the idea that high surface area and less crystallinity enhances Zn^{2+} ion release which in turn may favour new precipitate formation. Thus the diminishing of the Zn^{2+} ions from the solution is possibly due either to ionic adsorption by the precipitated calcium phosphate phases or to the formation of other Zn compounds. This effect was not obviously observed in the other composites because the layer formation was not a so evident and the Zn^{2+} release was not so intense.

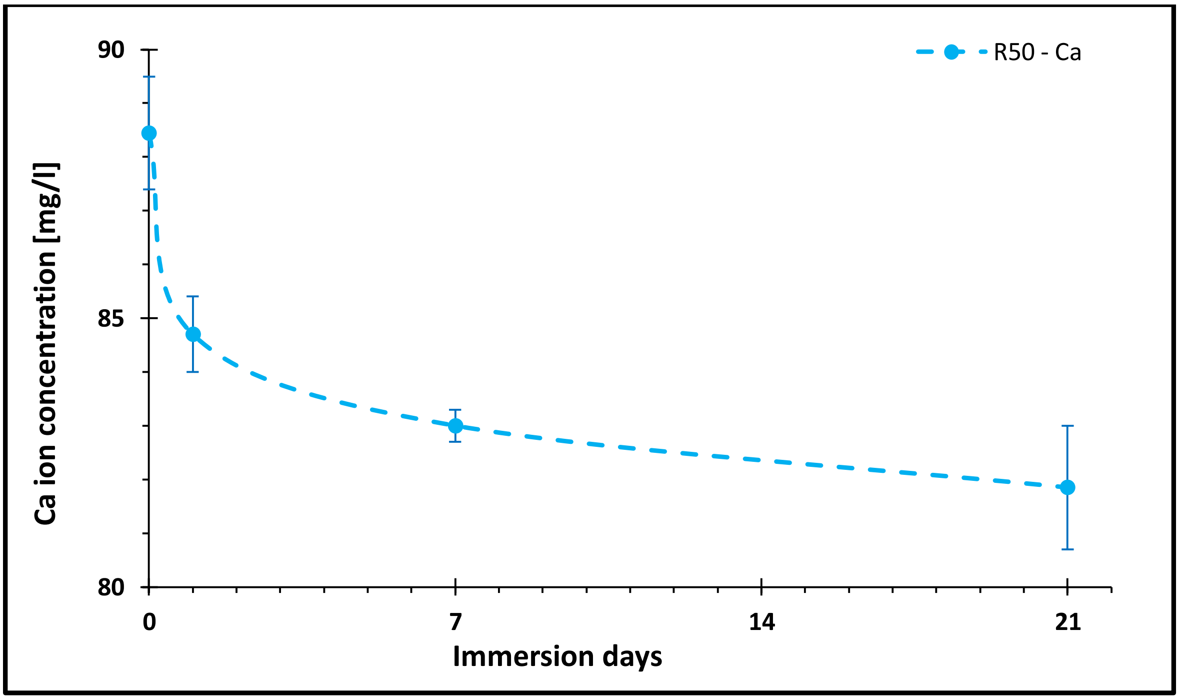

Figure 49. Ca ion concentration of the SBF solution after immersion of R50 composites (dashed lines serve to guide the eyes).

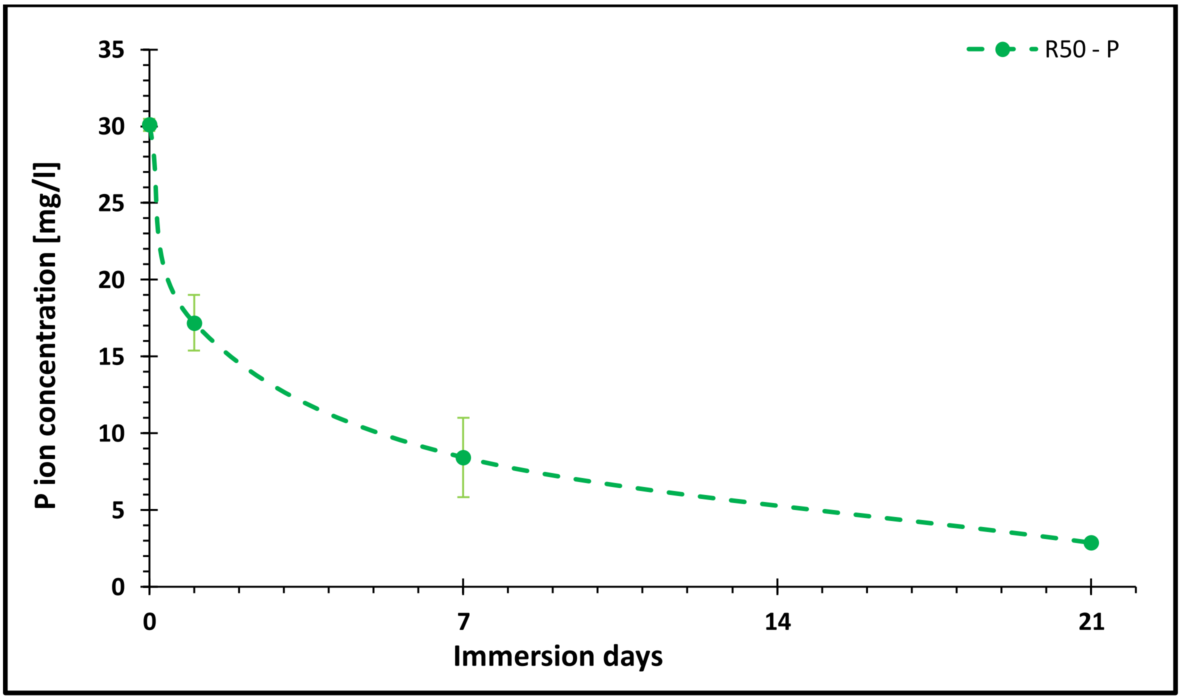

Figure 50. P ion concentration of the SBF solution after immersion of R50 composites (dashed lines serve to guide the eyes).

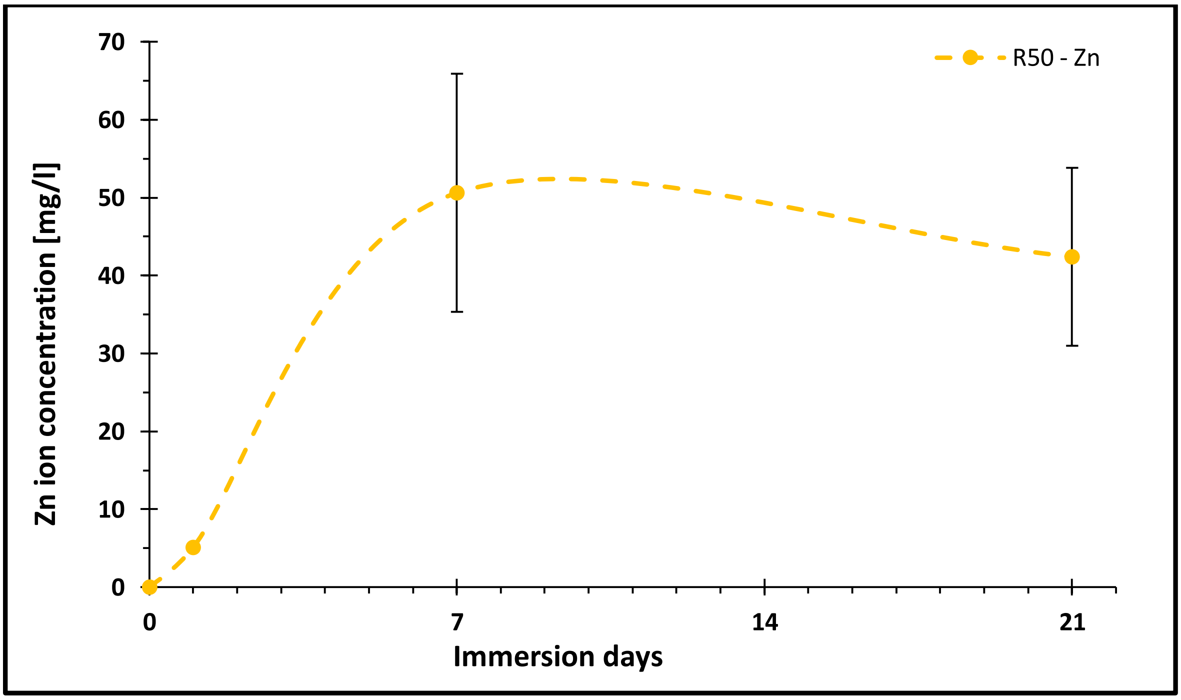

Figure 51. Zn ion concentration of the SBF solution after immersion of R50 composites (dashed lines serve to guide the eyes).

In this case it is possible to identify the precipitated phases from XRD patterns (figure 52) as the deposited layers cover the whole surface of the samples. Most of the peaks are due to zinc oxide embedded on the polymer matrix and the peaks from A to N are associated to the new phases formed (table 12), and its incipient crystallization. The phases that were taken into consideration were calcium phosphate (CP), monetite (M), brushite (B), hydroxyapatite (HA) and zinc phosphate (ZP) (table 11).

Table 11. Phosphorus, calcium and zinc compounds relevant XRD peaks location: CP (JPCDS 01-076-6031); HA (JPCDS 01-076-0694); M (JPCDS 00-009-0080); ZP (JPCDS 00-029-1390); B (JPCDS 00-009-0077).

	Phase				
	Calcium phosphate	**Hydroxyapatite**	**Monetite**	**Zinc Phosphate**	**Brushite**
	$Ca_3(PO_4)_2$	$Ca_5(PO_4)_3OH$	$CaPO_3(OH)$	$Zn_3(PO_4)_2$	$CaPO_3(OH){\cdot}2H_2O$
2 Theta	34.14	31.771	30.19	28.96	29.26
	59.16	59.94	n.a.	59.59	n.a.
	n.a.	56.33	n.a.	n.a.	n.a.

n.a. = non avaiable

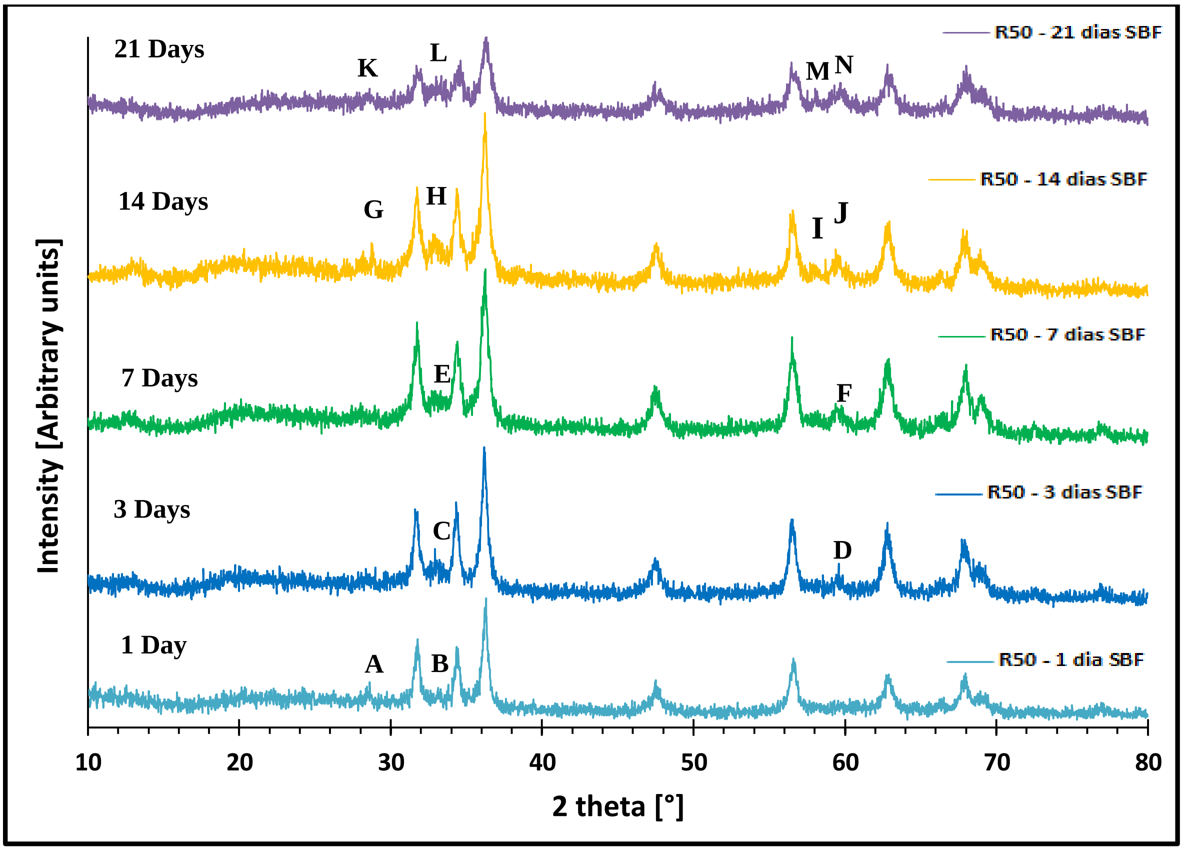

Figure 52. XRD patterns of R50 samples after immersion in SBF solution: light blue 1 day; dark blue 3 days; green 7 days; orange 14 days and purple 21 days.

Table 12. Possible fits of the new identified peaks in R50 samples XRD patterns to various crystalline phases after immersion in SBF during 1, 3, 7, 14 and 21 days.

Composite	Peak lable	2 theta	Phase				
			Calcium phosphate	Hydroxyapatite	Monetite	Zinc Phosphate	Brushite
			$Ca_3(PO_4)_2$	$Ca_5(PO_4)_3OH$	$CaPO_3(OH)$	$Zn_3(PO_4)_2$	$CaPO_3(OH)\cdot 2H_2O$
R50 -1D	**A**	28.62	n	n	n	**y**	~
	B	32.64	~	~	~	n	n
R50 - 3D	**C**	31.18	n	**y**	~	n	n
	D	59.58	**y**	**y**	n	**y**	n
R50 - 7D	**E**	31.72	n	**y**	~	n	n
	F	59.38	**y**	**y**	n	**y**	n
R50 - 14D	**G**	28.72	n	n	n	**y**	~
	H	32.06	~	~	~	n	n
	I	56.56	~	**y**	n	~	n
	J	59.40	**y**	**y**	n	**y**	n
R50 - 21D	**K**	28.60	n	n	n	**y**	~
	L	33.34	~	~	~	n	n
	M	57.52	~	**y**	n	~	n
	N	59.66	**y**	**y**	n	**y**	n

n = dosent fit
y = fits
~ = possible fit

After 1 day of immersion the layer formed on the R50 sample is revealed on the XRD pattern by the peaks A and B. The peak A ($2\theta = 28.62$) can be attributed to calcium zinc phosphide, zinc phosphate and possibly brushite. The B peak ($2\theta = 32.64$) can possibly be attributed to several calcium phosphate compounds, namely hydroxyapatite or monetite. This evidence suggests that in early stages this composite leads to the formation of several phosphorus compounds that depend on the Zn^{2+} ions released to the medium that can enhance the formation of those phases. After 3 days of immersion the precipitated phases shift to more specific phases, as the C peak ($2\theta = 31.18$) can only be attributed to hydroxyapatite or possibly monetite. The D peak ($2\theta = 59.58$) can be attributed to several compounds, namely calcium phosphate, hydroxyapatite or zinc phosphate. After 7 days of immersion the sample shows the same pattern as that corresponding to 3 days of immersion as, the C peak corresponds to the E peak ($2\theta = 31.72$) and the D peak to the F peak (2ɵ =59.38). After 14 days of immersion the XRD patterns slightly change as four peaks can be identified instead of two. As the amount of Zn^{2+} ions released to the medium enhanced the formation of calcium phosphorus phases till the 10th day of the assay; (figure 51) at day 14 the Zn^{2+} ions concentration started decreasing in the medium probably due to further precipitation of a zinc phosphorus phase or to the incorporation of zinc ions in the network of the already formed phases which reflected on the appearance of new peaks due to new compounds formation. The possible formed phases are brushite (2ɵ = 28.72), calcium phosphate (2ɵ = 32.06, 56.56, 59.40), hydroxyapatite (2ɵ = 32.06, 56.56, 59.40), monetite (2ɵ = 32.06) or zinc phosphate (2ɵ = 28.72, 56.56, 59.40). After 21 days of immersion the samples reflects the same behaviour as the one socked 14 days. These results show that a myriad of phosphorus compounds can be formed during the 21 days of immersion in SBF. It appears that initially both calcium phosphates and zinc phosphates are precipitated on the composites surface. As SBF media become enriched in Zn2+ ions more of these compounds are formed with consequent losses of phosphorus and calcium ions that give rise to the phosphorus calcium rich phases. The stabilization of calcium loss from the SBF solution further enhances the idea that at later times the phosphorus compounds formed are zinc rich as the Zn2+ ions are depleted from the SBF solution. The loss of ZnO phase is possible to be detected on the XRD patterns as ZnO peaks lose their intensity from day 1 to 21.

C2. Cell viability

The results of the resazurin cell viability assay performed on 50 mg of nanopowders, polyurethane, 2%$_{wt}$ (C2, P2) and 50%$_{wt}$ composites (C50, P50, R1 and R2) can be observed on figure 53.

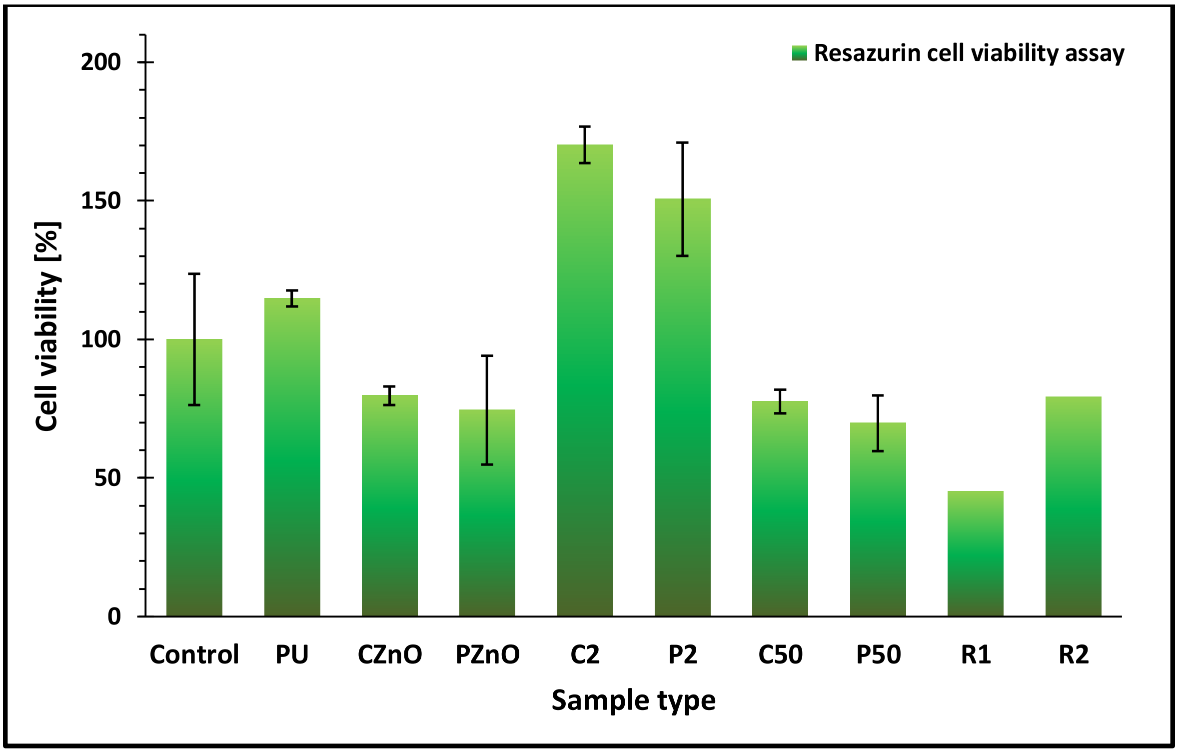

Figure 53. Resazurin cell viability assay of MC3T3-preosteoblastic cell line on 50 mg of commercial nanopowder (cZnO) or precipitated nanoflowers (pZnO), pure polyurethane (PU), PU composites with 2%$_{wt}$ of either commercial or precipitated nanoflowers (C2, P2, respectively), 50%$_{wt}$ composites of commercial or precipitated nanoflowers (C50 and P50, respectively) and composites with 50%$_{wt}$ nanospheres before and after SBF assay (R1 and R2, respectively).

When observing the behaviour of the materials alone, namely the PU and both powders, it can be seen two distinct behaviours, the rise of 15% in cell viability for the PU sample and a decrease of 20 and 25% for the nanopowders, commercial (cZnO) and nanoflowers (pZnO). The diminishing values shows that 50 mg of both these nanoparticles alone may induce cell death, probably due to the release of ROS species, Zn^{2+} excess ions release and mechanical action, but contrarily to the observed growth and osseointegration of MC3T3-E1 osteoblasts on ZnO nanoflowers by J. K. Park, et al (2010) [35]. As the toxicity of the nanopowders is not 100%, the difference in results may be due to ZnO particles concentration, and at smaller quantities growth and proliferation may be observed due to Zn^{2+} ions feed to the media and particle agglomeration. The increase of cell viability shows the biocompatibility of the selected polymer, and what may be the cause of failure in some applications when cell proliferation is not desired. The result shows the possibility of use in the orthopaedic area as a bioactive material that can improve the bonding at the interface prosthesis/bone. The surprising fact is that both composites loaded with $2\%_{wt}$ nanoparticles have an increase in cell viability of 70 and 50%, cZnO and pZnO powders respectively, which shows an enhancement on capability of cell proliferation of the polymer alone. This was probably due to the release of Zn^{2+} ions and to the changes in the polymer surface caused by the ZnO particles. With 50% nanoparticles loading the decreases in cell viability are evident, with a decrease of about 22 and 30% (C50 and P50, respectively), very similar to the effect of the powders alone. This fact supports the idea that the Zn^{2+} excess ion release diminishes the cell viability and that in the case of these composites cell viability is regulated by Zn^{2+} ions released to the media, and cytotoxicity is not majorly related to ROS liberation or mechanical action. The trial tests on R1 and R2 composites shows interesting results, as both composites shows a decrease in cell viability. The R1 composite ($50\%_{wt}$ rZnO) show a 60% decrease in cell viability, probably due to a large amount of Zn^{2+} release, related to both nanoparticles heavy concentration, larger SSA and low crystallinity. The R2 composite ($50\%_{wt}$ rZnO) shows a cell viability decrease of only 20% very similar to the composites (C50 and P50). The heavy release of Zn^{2+} ions occurred during the SBF assay, and the release of this composite probably is very low and similar to the C50 and P50 composites. Besides the Zn^{2+} effect, it cannot be taken outside the possibility of nanoparticles action or the calcium phosphate layer possible inconvenience to cell proliferation. In this case the fact that cell proliferation diminished with $50\%_{wt}$ of ZnO particles may be useful in applications were cell proliferation is a cause of failure, namely in mechanical devices or catheters or in cases were toxicology is needed, like cancer treatment.

4. Conclusions and future work

4.1. Conclusions

In the medical area novel biomaterials are needed to comply with the various demands and requisites of the many applications. Zinc oxide establishes itself as a polyvalent material that is suitable for many applications in the medical area, not only for its electrical properties (such as sensors or biomarker) but also for its antibacterial properties and cytotoxic effects. Engineered nanoparticles show to be highly promising in the biomedical area as a novel material, but as this type of particles are not fully known, accurate characterization and careful properties evaluation is needed. As the processing of such fine particles is extremely difficult and the size results often lye in a broad size range with poor particle shape control, suitable processing methods are needed.

In this work we successfully obtained pure phase ZnO nanopowders by a chemical precipitation method. Through a careful manipulation of the precipitation conditions nanoflowers-like particles consisting of agglomerated 50 nm thick ZnO platelets and 100 nm ZnO nanospheres were engineered. These powder particles when compared with commercial ZnO nanopowders exhibit higher SSA, narrower size range and distribution which make them suitable for uses in biomedical applications such as drug carriers. Although appearing suitable for drug transport these nanoparticles have a slight cytotoxic effect on MC3T3 cell line and the toxicity may be related to an excess Zn^{2+} ion release to the media.

The bioactivity assay revealed interesting behaviours from the composites produced with the engineered ZnO nanoparticles. The used polymer, a medical grade thermedics SG80A polyurethane, did not exhibit bioactivity in SBF because after 21 days of immersion no calcium phosphate layer was formed. In spite of this the cell viability assay with MC3T3 cell line showed that this polyurethane induces a small cell growth, thus confirming its biocompatibility. Problems of mechanical device failure in vivo may arise from its use in inert devices as heart valves or catheters induced either by cell adhesion or proliferation. Such problems may be solved by adding an adequate quantity of ZnO particles (50w%) to the polymer that induces cell mortality. This cytotoxicity is thought to be due to the Zn^{2+} ion release to the medium as most of the particles are entrapped in the polymer matrix. Moreover it closely correlates to the higher SSA of the nanospheres which have higher Zn^{2+} ion release capability. The $50\%_{wt}$ nanospheres loaded composite was surprisingly bioactive as inferred from its calcium phosphates compounds forming capability but was also the composite with the highest mortality rate. Although not tested, these particles may also help reducing biological films that form at the surface of medical devices thus helping to reduce infections and device failure.

In the framework of the ZnO particles cytotoxicity which is being currently addressed for new cancer therapies, it was shown that depending on the ZnO load, some of the produced composites may carry such potential as is the case of the 50 w% composites. However, less loaded composites such as the ones with $2\%_{wt}$ ZnO showed the higher cell viability rate thus predicting its usefulness in aiding the bonding of prosthesis to the bone in spite of their negligible capability of inducing calcium phosphates compounds, it was thus observed that the cytotoxicity of the produced composites varies between the noncytotoxic ($2\%_{wt}$) and the cytotoxic ($50\%_{wt}$) loaded composites, being the highest toxicity associated to the highest SSA of ZnO particles.

As a final conclusion it may be pointed out that engineered ZnO particles with different properties allowed producing PU/ZnO composites with the ability of eliciting distinct cell responses, i.e. enhanced cell viability or, contrarily, enhanced cell toxicity effects. Consequently, PU/ZnO composites may be designed for applications where bone growth is required or for applications where the aim is to block the growth and spread of cells, as in targeted cancer therapies.

4.2. Future work

In this work two limits of ZnO loading in which cytotoxicity to MC3T3 pre-osteoblastic cell line lies were found, but further works are needed to carefully characterize both nanoparticles and composites. Accurate evaluation of particles properties should be extended to include Zeta potential, solubility, hydrophobic character, electronic related properties, reactivity and toxicity for enabling the identification of new applications for these particles, namely in areas like cancer treatment or nerve regeneration.

Furthermore the study carried out in this project was focused on surface properties of films, and thus the bulk properties must be evaluated and balanced among composition, materials engineering and cells response.

The clear identification of distinct toxicity limits induced by the developed composites pushes to the need of investigating *in vitro* behaviour of other compositions both in acellular and in the presence of different cell lines in order to establish a comprehensive panel of applications suggested by the specific responses obtained.

Bibliography

[1] A. P. Kumar, D. Depan, N. S. Tomer, R. P. Singh, “Nanoscale particles for polymer degradation and stabilization-Trends and future perspectives”, Progress in Polymer Science, 34, 2009, 479–515.

[2] J. Kosk-Bienko, “Literature Review -Workplace exposure to nanoparticles”, European Agency for Safety and Health at Work (EU-OSHA), Spain.

[3] W. H. De Jong, P. J. A. Borm, “Drug delivery and nanoparticles: aplications and hazards”, International journal of nanomedicine, 2, 2008, 133-149.

[4] D. Guo, C. Wu, H. Jiang, Q. Li, X. Wang, B. Chen, “Synergistic cytotoxic effect of different sized ZnO nanoparticles and daunorubicin against leukemia cancer cells under UV irradiation”, Journal of Photochemistry and Photobiology B: Biology, 93, 2008, 119–126.

[5] J. T. Seil, T. J. Webster, “Decreased astroglial cell adhesion and proliferation on zinc oxide nanoparticle polyurethane composites”, International Journal of Nanomedicine 2008, 4, 523–531.

[6] K. Byrappa, S. Ohara, T. Adschiri, “Nanoparticles synthesis using supercritical fluid technology – towards biomedical applications”, Advanced Drug Delivery Reviews, 60, 2008, 299–327.

[7] C. Buzea, I. I. Pacheco, K. Robbie, “Nanomaterials and nanoparticles: Sources and toxicity”, Biointerphases 4, 2007, 18-65

[8] W. G. Kreyling, M. Semmler-Behnke, Q. Chaudhry “A complementary definition of nanomaterial”, Nano Today, 5, 2010, 165—168.

[9] M. Yoshimura, K. Byrappa, “Hydrothermal processing of materials: past, present and future”, Journal of Materials Science, 43, 2008, 2085–2103.

[10] C. T. Chalfoun, G. A. Wirth, G. R. D. Evans, “Tissue engineered nerve constructs: where do we stand?” Journal of Cellular and Molecular Medicine, 10, 2006, 309-317.

[11] R. L. Reis, S. Weiner, “Learning from Nature How to Design New Implantable Biomaterials: From Biomineralization Fundamentals to Biomimetic Materials and Processing Routes”, 2004, Kluwer Academic Publishers, Dordrecht, Netherlands.

[12] C. E. Schmidt, J. B. Leach, “Neural tissue engineering: Strategies for Repair and Regeneration”, Annu. Rev. Biomed. Eng., 5, 2003, 293–347.

[13] L. Zhang, T. J. Webster, “Nanotechnology and nanomaterials: Promises for improved tissue regeneration”, Nano Today, 4, 2009, 66—80.

[14] R. Murugan, S.S. Liao, S. Ramakrishna, P. Molnar, Z. M. Huang, M. Kotaki, K. P. Rao, J. J. Hickman, "Skeletal Regenerative Nanobiomaterials, Materials science foundations (monograph series), 62, 2010, 1-34.

[15] Bernadette Miara, Eduard Rohan, Mustapha Zidi, Beatrice Labat, "Piezomaterials for bone regeneration design--homogenization approach", Journal of the Mechanics and Physics of Solids, 53, 2005, 2529–2556.

[16] C. Halperin, S. Mutchnik, A. Agronin, M. Molotskii, P. Urenski, M. Salai,G. Rosenman, "Piezoelectric Effect in Human Bones Studied in Nanometer Scale", Nano Letters, 4, 2004, 1253-1256.

[17] OV Salata," Applications of nanoparticles in biology and medicine", Journal of Nanobiotechnology, 2, 2004, 1-6.

[18] C. Jagadish, S. Pearton, "tZinc Oxide Bulk, Thin Films and Nanostructures: Processing, Properties, and Applications", 2006, Elsevier, Hong Kong.

[19] C. Klingshirn, "ZnO: Material, Physics and Applications", ChemPhysChem, 8, 2007, 782 – 803.

[20] Cory Hanley, Aaron Thurber, Charles Hanna, Alex Punnoose, Jianhui Zhang, Denise G. Wingett, "The Influences of Cell Type and ZnO Nanoparticle Size on Immune Cell Cytotoxicity and Cytokine Induction", Nanoscale Res Lett., 4, 2010, 1409–1420.

[21] H. Zhang, B. Chen, H. Jiang, C. Wang, H. Wang, X. Wang, "A strategy for ZnO nanorod mediated multi-mode cancer treatment", Biomaterials, 32, 2011, 1906-1914

[22] M. Hashemi, S. Ghavami, M. Eshraghi, E. P. Booy, M. Los, "Cytotoxic effects of intra and extracellular zinc chelation on human breast cancer cells", European Journal of Pharmacology, 557, 2007, 9–19.

[23] C.Hanley, J. Layne, A. Punnoose, K. M. Reddy, I. Coombs, A. Coombs, K. Feris, and D. Winget, "Preferential Killing of Cancer Cells and Activated Human T Cells Using ZnO Nanoparticles", Nanotechnology, 19, 2008, 1-10.

[24] M. Premanathan, K. Karthikeyan, K. Jeyasubramanian, G. Manivannan, "Selective toxicity of ZnO nanoparticles toward Gram-positive bacteria and cancer cells by apoptosis through lipid peroxidation", Nanomedicine: Nanotechnology, Biology, and Medicine, 7, 2011, 184–192.

[25] J. Li, D. Guo, X. Wang, H. Wang, H. Jiang, B. Chen, "The Photodynamic Effect of Different Size ZnO Nanoparticles on Cancer Cell Proliferation In Vitro", Nanoscale Res , 5, 2010, 1063–1071.

[26] S. Nair, A. Sasidharan, V. V. D. Rani, D. Menon, S. Nair, K. Manzoor, S. Raina, "Role of size scale of ZnO nanoparticles and microparticles on toxicity toward bacteria and osteoblast cancer cells", J Mater Sci: Mater Med, 20, 2009, 235–241.

[27] R. Wahab, N. K. Kaushik, A. K. Verma, A.Mishra , I. H. Hwang, Y. Yang, H. Shin • Y. Kim "Fabrication and growth mechanism of ZnO nanostructures and their cytotoxic effect on human brain tumor U87, cervical cancer HeLa, and normal HEK cells", J Biol Inorg Chem, 2010

[28] W. Songa, J. Zhangb, J. Guoa, J. Zhanga, F. Dingc, L. Li, Z. Suna, "Role of the dissolved zinc ion and reactive oxygen species in cytotoxicity of ZnO nanoparticles", Toxicology Letters, 2010.

[29] P. J. Moos, K. Chung, D. Woessner, M. Honeggar, N. S. Cutler, J. M. Veranth, "ZnO Particulate Matter Requires Cell Contact for Toxicity in Human Colon Cancer Cells", Chem. Res. Toxicol., 23, 2010, 733–739.

[30] M. Ahamed, M. J. Akhtar, M. Raja, I. Ahmad, M. K. J. Siddiqui, M. S. AlSalhi, S. A. Alrokayan, "ZnO nanorod-induced apoptosis in human alveolar adenocarcinoma cells via p53, survivin and bax/bcl-2 pathways: role of oxidative stress", Nanomedicine: Nanotechnology, Biology, and Medicine, 7, 2011, 904–913.

[31] O. Yamamoto, "Influence of particle size on the antibacterial activity of zinc oxide" International Journal of Inorganic Materials, 3, 2001, 643-646.

[32] K.Hirota, M. Sugimoto, M. Kato, K. Tsukagoshi, T. Tanigawa, Hiroshi Sugimoto, "Preparation of zinc oxide ceramics with a sustainable antibacterial activity under dark conditions", Ceramics International, 36, 2010, 497–506.

[33] D. Xie, D. Feng, Il-Doo Chung, A. W. Eberhardt, "A hybrid zinc–calcium–silicate polyalkenoate bone cement", Biomaterials, 24, 2003, 2749–2757.

[34] H. Oudadesse, E. Dietrich, Y. L. Gal, P. Pellen, B. Bureau, A.A. Mostafa and G. Cathelineau," Apatite forming ability and cytocompatibility of pure and Zn-doped bioactive glasses", Biomed. Mater., 6, 2011, 1-9

[35] J. K. Park, Yong-Jin Kim, J. Yeom , J. H. Jeon , Gyu-Chul Yi , J. H. Je, S. K. Hahn, "The Topographic Effect of Zinc Oxide Nanoflowers on Osteoblast Growth and Osseointegration", Adv. Mater., 22, 2010, 4857–4861.

[36] Patrick Vermette, Hans J. Griesser, Gaétan Laroche, Robert Guidoin, " Biomedical applications of polyurethanes", 2001, Eurekah.com, Georgetown, Texas, U.S.A.

[37] H. B. Machado, Rui N. Correia, J. A. Covas, "Synthesis, extrusion and rheological behaviour of PU/HA composites for biomedical applications", J Mater Sci: Mater Med, 21, 2010, 2057–206.

[38] S. Yanhui, Q. Kunyuan, V. Sing-tuh, "Studies on the oxidation and graft copolymerization of polyethers", Polymer communications, 1, 1984, 48-56.

[39] B. Saad, T. D. Hirt, M. Welti, G. K. Uhlschmid, P. Neuenschwander, U. W. Suter, "Development of degradable polyesterurethanes for medical applications: In vitro and in vivo evaluations", Journal of Biomedical Materials Research, 36, 1997, 65–74.

[40] K. Gorna, S. Gogolewski, “Preparation, degradation, and calcification of biodegradable polyurethane foams for bone graft substitutes”, Materials Research Society Spring Meeting, San Francisco, April, 2002 1–5.

[41] V. L. Gott, D. E. Alejo, D. E. Cameron, “Mechanical heart valves: 50 years of evolution”, The Annals of Thoracic Surgery, 76, 2003, 2230–2239.

[42] E. Jabbari, M. Khakpour, “Morphology of and release behavior from porous polyurethane microspheres”, Biomaterials, 21, 2000, 2073-2079.

[43] R. Chandra, R. Rustgi, “Biodegradable polymers”, Prog. Polym. Sci., 23, 1998, 1273–1335.

[44] Q. Guo, P. T. Knight, P. T. Mather, “Tailored drug release from biodegradable stent coatings based on hybrid polyurethanes”, Journal of Controlled Release, 137, 2009, 224–233.

[45] Tecoflex SG80A polyurethane data sheet

[46] Martin K. McDermott, LeRoy W. Schroeder, Shay L. Balsis, Nicole A. Paradiso, Michelle L. Byrne, Robert M. Briber, “Mechanical Properties of Polyurethane Film Exposed to Solutions of Nonoxynol-9 Surfactant and Poly(EthyleneGlycol)”, Journal of Applied Polymer Science, 91, 2004, 1086–1096.

[47] T. Kokubo, H. Takadama, “How useful is SBF in predicting in vivo bone bioactivity?”, Biomaterials, 27, 2006, 2907–2915.

[48] S. Pina, S.I. Vieira, P. Rego, P.M.C. Torres, O.A.B. da Cruz e Silva, E.F. da Cruz e Silva, J.M.F. Ferreira, “Biological responses of brushite-forming Zn- and ZnSr-substituted β-tricalcium phosphate bone cements”, European Cells and Materials, 20, 2010, 162-177.

[49] Y. Leng, “Materials characterization - Introduction to Microscopic and Spectroscopic Methods”, 2008, John Wiley & Sons, Singapore, Asia.

[50] C R. Brundle, C. A. Evans, Jr. S. Wihon, “Encyclopedia of materials characterization – Surfaces, Interfaces, Thin Films”, 1992, Manning Publications Co., Butterworth-Heinemann, USA.

[51] W. L. Suchanek, “Systematic study of hydrothermal crystallization of zinc oxide (ZnO) nano-sized powders with superior UV attenuation”, Journal of Crystal Growth, 312, 2009, 100–108.

[52] K. S. W. Sing, D. H. Everett, R. A. W. Haul , L. Moscou, R. A. Pierotti, J. Rouqueroll, T. Siemieniewska, “Reporting physisorption data for gas/solid systems with Special Reference to the Determination of Surface Area and Porosity”, Pure & Appl. Chem., 57, 1985, 603—619.

[53] F. Rouquerol, L. Rouquerol, K. Sing, “Adsorption by Powders and Porous Solids: Principles, Methodology and Applications”, 1999, Academic Press, London, United Kingdom.

[54] Micromeritics Instrument Corporation, “Gas Adsorption Theory – poster presentation”

[55] I. Siminiceanu, I. Lazau, Z. Ecsedi, L. Lupa, C. Burciag, "Textural Characterization of a New Iron-Based Ammonia Synthesis Catalyst", Chem. Bull., 2008, 53, 1-2.

[56] Resazurin Cell Viability Assay Kit, Catalog Number: 30025-1, 2011

[57] M.E.V. Costa, J.L. Baptista, "Characteristics of zinc oxide powders precipitated in presence of alcohols and amines", J. Europ. Ceram. Soc., 11(1993) 275-281.

[58] C. Guignot, N. Betz, B. Legendre, A. L. Moel, N. Yagouby, "Degradation of segmented poly(etherurethane) Tecoflex induced by electron beam irradiation: characterization and evaluation, Nuclear instruments and methods in physics research B, 185, 2001, 100

[59] Anne Simmons, Jari Hyvarinena, Ross A. Odell, Darren J. Martin, Pathiraja A. Gunatillake, Kathryn R. Noble, Laura A. Poole-Warrena, "Long-term in ™vivo biostability of poly(dimethylsiloxane)/poly(hexamethylene oxide) mixed macrodiol-based polyurethane elastomer", Biomaterials, 25, 2004, 4887–4900.

[60] Nirmala R. James,Juby Philip,A. Jayakrishnan, "Polyurethanes with radiopaque properties", Biomaterials, 27, 2006, 160–166.

[61] S. Vlad, C. Ciobanu, R. V. Grandinaru, L. M. Grandinaru, A. Nistor, P. Poni, Al. I. Cuza, "Antibacterial evaluation of some polyurethane membranes modified by zinc oxide nanoparticles", Digest Journal of Nanomaterials and Biostructures, 6, 2011, 921-930.

[62] Somia Awad, Hongmin Chen, Guodong Chen, Xiaohong Gu, James L. Lee, E. E. Abdel-Hady, Y. C. Jean, "Free Volumes, Glass Transitions, and Cross-Links in Zinc Oxide/Waterborne Polyurethane Nanocomposites", Macromolecules, 44, 2011, 29–38.

[URL1] http://en.wikipedia.org/wiki/File:Wurtzite_polyhedra.png, accessed in 15/12/2011.